MODELING OF THIN WIRE STRUCTURES FOR THE FDTD METHOD

LI BINGHAO

PhD

The Hong Kong Polytechnic University

2019

The Hong Kong Polytechnic University

Department of Building Services Engineering

MODELING OF THIN WIRE STRUCTURES FOR THE FDTD METHOD

LI BINGHAO

A thesis submitted in partial fulfillment of the requirements for the degree of

Doctor of Philosophy

(Temporary Binding for Examination Purpose)

January 2019

Certificate of Originality

I hereby declare that this thesis is my own work and that, to the best of my knowledge and belief, it reproduces no material previously published or written, no material that has been accepted for the award of any other degree of diploma, except where due acknowledgement has been made in the text.

LI Binghao

Abstract

The finite-difference time-domain (FDTD) method is an intuitive and powerful analysis technique to solve electromagnetic (EM) problems in the time domain. The FDTD method has the advantages of broadband field simulation, less memory space, easy implementation of parallel computing and others. Because of the weakness in simulating a large working volume with elaborate structures, several thin-wire model techniques were developed. However, these techniques cannot model lossy wires with cross sections with circular or non-circular shapes. The inclined thin-wire structures cannot be simulated with acceptable accuracy as well. They have limited values in the application of lightning surge analysis in practical wire structures, such as long power/signal line and cables, structural steel and others in power systems and building structures. In this thesis, three types of extended thin-wire models will be proposed to represent lossy wire structures for lightning surge analysis. These proposed models are then applied to investigate lightning transients in a building, a meteorological tower and a light rail system.

The first extended thin-wire model is used to simulate lightning surge or wave propagation on lossy round wire structures. The wire structures are represented with time-domain cascade circuits and are integrated into a traditional thin-wire model in the FDTD simulation. The wire structures include solid round conductors, cylindrical tubes and coaxial cables, and the skin effect is fully considered. In the coaxial structure, the currents in both inner and outer conductors are not

necessarily balanced. The proposed model has been validated analytically and numerically, and good agreements have been observed. It has been applied to analyze lightning current sharing in a lossy RF coaxial cable. Compared with the traditional FDTD method, this extended thin-wire model requests less memory space and computation time in the simulation.

Lossy thin-wire structures with arbitrary inclination are quite common in the industry, which are difficult to address using traditional FDTD methods. An extended thin-wire model is then proposed. The frequency-dependent losses of the conductors are fully taken into account, and a vector fitting technique is applied to deal with frequency-dependent parameters in the time-domain analysis. The bidirectional coupling within the lossy coaxial conductors is modelled. The currents in inner and outer conductors are not necessarily balanced. Three cases are presented to investigate wave propagation velocity, wave attenuation, and current distribution. They are compared with analytical results and numerical results. It is found that the proposed thin-wire models can depict the transient behaviors in the lossy inclined conductors with the velocity error of less than 1%, and the attenuation error of less than 1.5%

To mimic lossy wire structures with non-circular cross sections for transient analysis, another thin-wire model is developed. Unique correction factors of field quantities and the surface electric field of wire structures are introduced in the model. The stability problem is investigated. A method, called high-frequency

filtering method, is proposed to stabilize the computation stability. These parameters are both frequency-dependent and position-variant. They are evaluated in an initialization process and are applied in the updating process using an iterative convolution technique. The proposed method is validated with the transmission line theory analytically and the traditional FDTD method numerically. Six types of wire structures are tested, including rectangular, H-shape, cross-shaped, T-shape, L-shape and U-shape structures. Good agreements are observed. It is found that the computation time is reduced to 1% of that with the conventional FDTD method, and the computer memory to 30% in the tested case. General guidelines on wire zone meshing are provided as well. Finally, this method is applied to analyze lightning surges in a light rail system under a direct lightning stroke.

Lightning surges induced in buildings are investigated with an FDTD method. When down conductors are used in a building to discharge lightning current, induced surges are observed in adjacent distribution circuits due to electric and magnetic coupling. They are different from those obtained using quasi-static models. The peak value of surge voltage in an open circuit is proportional to a logarithmic function of conductor spacing. The induced current in a short circuit can be directly determined using a closed-form formula. It is found that connected capacitors can reduce the induced surge voltages but may not be effective. SPDs are then recommended installing at two far ends of a distribution circuit. They are

not required to dissipate substantial lightning surge energy observed in the down conductor. It is found that the surge currents in SPDs can be estimated using the closed-form formula as well.

The proposed extended thin-wire models are applied for the simulations of a meteorological tower and a light rail system. For transient analysis, the meteorological tower, lightning current distribution, ground potential rise and step voltage are analyzed. It is found that the majority of the lightning current is discharged via the outermost steel cables and are dissipated to the earth by the horizontal grounding bars. Both the step voltage and ground potential are measured as well in three different grounding configurations. The safety of step voltage in the vicinity of the tower is also addressed. In the DC light rail, the diode boxes provided between rail tracks and fault current return wires are arranged to limit stray current. They are susceptible to damage during lightning strikes. The surge voltages on diode boxes are analyzed and simulated by the FDTD method under different conditions. The frequency dependent loss of wire conductors and lossy rail tracks are considered. It is found that rising front of return strokes, lightning channel locations and soil conductivity nearby affect the surge voltage significantly.

Publications

1. Papers in Journals

- Yaping Du, **Binghao Li**, and Mingli Chen, "Surges induced in building electrical systems during a lightning strike," *Electric Power Systems Research,* vol. 139, pp. 68-74, 2016.

- Yaping Du, **Binghao Li**, and Mingli Chen, "The Extended Thin-Wire Model of Lossy Round Wire Structures for FDTD Simulations," *IEEE Transactions on Power Delivery,* vol. 32, pp. 2472-2480, 2017.

- **Binghao Li**, Yaping Du, and Mingli Chen, "An FDTD thin wire model for lossy wire structures with non-circular cross section," IEEE Transactions on Power Delivery, vol. 33, pp. 3055-3064, 2018.

- **Binghao Li**, Yaping Du, and Mingli Chen, “Thin-wire Models for Inclined Conductors with Frequency-dependent Losses,” IEEE Transactions on Power Delivery, doi: 10.1109/TPWRD.2019.2908012

2. Papers in Conferences

- Yaping Du, **Binghao Li**, and Mingli Chen, "Lightning-induced surges in building electrical systems," *2014 International Conference* in *Lightning Protection (ICLP),* IEEE, 2014, pp. 1217-1222

- Yaping Du, **Binghao Li**, and Mingli Chen, "Ground Potential Rise in Grounding Systems Using the FDTD Method," presented at the Asia-Pacific International Conference on Lightning (APL), Nagoya, Japan, 2015.

- **Binghao Li** and Yaping Du, "A modified FDTD method using a hybrid Cartesian-cylindrical coordinate system," in *2016 Asia-Pacific International Symposium on Electromagnetic Compatibility (APEMC),* IEEE, 2016, pp. 648-651.

- Ruihan Qi, **Binghao Li**, Yaping Du. “Induced surges in railway signaling systems during an indirect lightning strike,” *2016 International Conference* in *Lightning Protection (ICLP),* IEEE, 2016, pp. 1-5.

- Yaping Du, **Binghao Li**, and Mingli Chen. "Hybrid MoM/FDTD method for thin wire structures with rectangular cross section." in *2016 IEEE Conference on Electromagnetic Field Computation (CEFC),* IEEE, 2016.

- Lin Liu, **Binghao Li**, Y. Du and Mingli Chen, " Analysis of Lightning Current, GRP and Step Voltage of a Tall Tower Using the FDTD Method," presented at the Asia-Pacific International Conference on Lightning (APL), Krabi, Thailand, 2017.

- **Binghao Li**, Ruihan Qi, Yaping Du, Mingli Chen. “Lightning surge analysis in light rail transit using the FDTD method,” *2016 International Conference*

in *Lightning Protection (ICLP),* IEEE, 2018, pp. 1-6.

Acknowledgement

I would like to thank my supervisor, Prof. Yaping Du, from Department of Building Services Engineering, the Hong Kong Polytechnic University, for the patient guidance, encouragement and advice he has provided throughout my time as his student. I have been extremely lucky to have a supervisor who cared so much about my work, and who responded to my questions and queries so promptly. Besides my advisor, I would like to thank my colleagues, Mr. Yuxuan Ding and Mr. Yang Zhang, for their unfailing support and assistance.

My sincere thanks go to my wife, for her continued company and encouragement throughout this entire process and has made countless sacrifices to help me get to this point. Finally, my deepest appreciation must be expressed to my parents who provide me unconditional support and love and experienced all the ups and downs of my research with me.

Contents

List of Figures

List of Tables

1 Introduction

1.1 Background

The FDTD method, proposed by Yee [1] in 1966, is an intuitive and powerful analyzing tool to investigate electromagnetic problems. After 1990, with the unpredictable development of computer science technology, the FDTD method has been developed as one of the mainstream simulation techniques for solving theoretical and practical EM problems. This numerical method was first applied in isotropic media with simple geometric structures. Then the applications were extended to electromagnetic wave interactions [2], bio-electromagnetic models [3, 4], electromagnetic pulse problems [5], waveguide models [6-8], the printed circuit board with lumped electric elements [9-12] and the lightning protection analysis [13-17].

Since the FDTD method solves Maxwell's equations in the time domain, wideband problems with non-linear material structures can be calculated naturally. This algorithm meshes the whole problem volume into hexahedral cells with an orthogonal structure. The electric field component, E, and the magnetic component, H, are located at the centers of faces and edges of the hexahedral cells. The time-domain Maxwell's equations in differential form constructed in each cell are solved by centered differential method. During the updating process, E and H field components always have a half time-step discrepancy in the time domain and update in a leapfrog manner. The electric field components, E, update first at a

certain time-step, and the magnetic field components, H, will update at next half time-step. This updating cycle will be repeated until a condition set initially is satisfied. Then, a second-order result can be obtained.

In the FDTD method, the choice of the cell size, Δs, and the time step, Δt, plays an important role in stable simulation [2]. Δs is determined by both the object shapes and the expected wavelength. The maximum time step, Δt, is determined by the cell size of the smallest cells in the working volume. It should satisfy the so-called Courant-Friedrichs-Lewy (CFL) condition [18]. Except for the time step and the cell size, several factors can also affect the simulation stability and accuracy, such as the absorbing boundary condition, sub-cell setting and non-uniform mesh.

The lumped circuit elements frequently used in practical electromagnetic problems are involved in the FDTD computation. Usually, these elements, such as voltage source, current source, resistor, inductance, capacitor, are implemented by incorporating the Ohm's law, circuit element nature and the extended Maxwell equations [19] onto specific E vectors.

In a working volume constructed in a Cartesian coordinate system, six planes of boundaries always need to be defined at the initial state of the simulation process. Except for the perfect electrical conductor (PEC) boundary, the perfect magnetic conductor (PMC) boundary, the absorbing boundary condition (ABC) is always needed to absorb unwanted reflection EM waves, so as to simulate an infinitely

large space. In 1981, Gerrit Mur [20] presented the Mur absorbing boundary, which is quite comprehensible. LIAO absorbing boundary [21] was proposed in 1984 and gained an extensive use for its easy-implement and good absorbing performance. In 1994, Berenger [22] first described the perfectly matched layer (PML) absorbing boundary. Although PML boundary requires comparatively large memory space, it can absorb nearly all the reflected waves and satisfy most of the simulation requirements. A better absorbing layer called the convolutional perfectly matched layer (CPML) [23] was proposed in 2000, which can fully absorb the unwanted waves theoretically to mimic an infinite large conductor and media. In this project, the PML boundary condition is adopted for its suitable features.

Theoretically, the FDTD method can solve any electromagnetic problems and physical phenomena with acceptable accuracy if the mesh is fine enough. However, it will cost a huge memory resource and long calculation time, especially for the models contain tips and gaps. To cope with this, two types of the non-uniform grid were proposed with a 2nd-order accuracy: the universal grading scheme and the sub-gridding scheme, so that the grids can be made denser at key regions, and be sparse at regions where the field changes smoothly. The sub-gridding scheme[24], using the interpolation technique, embeds fine grids into coarse grid region. During each coarse grid updating cycle, the field values in finer grids are updated corresponding times. The universal grading scheme [25-27] sets the changing ratio

of non-uniform cell sizes appropriately, and then revising the field updating equation of the mesh-changing boundary to obtain the 2nd-order accuracy.

1.2 Challenges

One of the biggest challenges of the FDTD application is the simulation of subtle-structured models with reasonable accuracies, such as straight wires with a small radius, thin plates, models with tips and holes. Theoretically, the FDTD method can model any geometric structures only if the mesh is fine enough, while, since the whole working volume is as large as hundreds of meters occasionally, an extra huge computational resource will be required. The non-uniform mesh and the traditional thin-wire model have been proposed to solve this problem, however, there still remain several important issues unsolved, such as skin effect, frequency variant characteristics and ferromagnetic features.

Straight wires with small radius involving EM phenomena and effects are common in the electric power grid, communication systems, railway systems and building structures. The lightning protection systems installed in modern buildings, one of the main applications, are the essential means to prevent facilities and equipment in buildings from getting damage. The transmission procedure of the lightning stroke energy from the top of a building to the grounding electrode is affected by the building structure prominently. The main transformation passage, the down conductor system, consists of several straight wire conductors with ferromagnetic and dispersive features. Extra wire structures, such as

communication coaxial cables, pipelines and reinforcing steel bars in beams columns, will distort the current waveforms and magnitudes by shunting part of lightning current and the electromagnetic coupling effect. In order to supply enough lightning protection, appropriate lightning protection devices need to be selected and installed in appropriate locations based on the current distribution characteristics and grounding electrode performance. As a result, analyzing the current propagation performance in finite conductivity, dispersion, ferromagnetic material conductor and the energy discharge in practical soil conditions are valuable and inevitable.

Although other numerical simulation methods may have advantages over small-sized model, they all exist weaknesses and limitations. The moment of method (MOM) solves linear partial equations in integral form, and it is hard to implement for evaluating Green's functions and the coupling integrals. MOM is suitable in planer or layer stacked up structures. The partial element equivalent circuit (PEEC) is also an integral-form simulation method by combining electromagnetic and circuit theory. Even though the PEEC method can construct the equivalent circuit with the aid of the SPICE technique, the unintentional coupling effect, especially in a complex environment with multi-conductors, is hard to confirm. Besides, the instability problem may occur in the case of involving the time-delay effect. The finite element method (FEM) is another true 3D analytical method, which is unnecessary to consider the coupling effect. It meshes the whole working volume

into small tetrahedral cells, then forms a large matrix consisting of parameters of each cell to get a reasonable result. However, as the size of a simulation target increasing, the requirement of memory space and calculation time will also increase as the existence of the matrix. Furthermore, the FEM is mainly suitable in narrow-band frequency investigation.

Recently thin wire models in the FDTD method have been developed to deal with long wire structures. Such techniques have been successfully applied to analyze electromagnetic transients in electric power systems, building wirings and electrified railway systems, such as grounding systems [28], high voltage substations [29, 30], overhead lines [14, 31-36], transmission towers [37-39], vertical conductors [40-42] , wind turbine generator systems [43] , electrical wirings in buildings [44], electrified railway systems [45] and lines with corona discharge[36].

The thin wire model is the technique which builds specific FDTD updating equations in the local cells of a wire by taking into account EM field distribution. The thin wire model proposed in [46] calculates the current and charge on the wire with the in-cell inductance technique and represents the wire as a series of equivalent current sources in the FDTD region. This model has the advantage in dealing with oblique wires and multi-wire junctions [47]. In [48] special field updating formulas are presented by taking into account the field distribution pattern around the wire in the contour path integration. This is a straightforward

method. However, it may have problems with stability and results may be inaccurate. The thin wire model in [49-51] is established using the intrinsic radius which is obtained with a numerical method. In case that the conductor radius is different from the intrinsic radius, material parameters are adjusted to match the required radius. This method is stable and easy to be implemented. In [52] the concept of line averaged quantities and surface averaged quantities are introduced in deriving the field updating equations. This model possesses the advantages in dealing with thin wires with arbitrary cross-sections.

The traditional thin wire models mainly mimic solid and lossless thin wire structures embedded in air or lossy materials. In case of a lossy wire, it is quite common to insert a lumped DC resistance in the FDTD equations. This certainly incurs calculation errors if the skin effect is significant. Alternatively, the surface impedance boundary condition (SIBC) is proposed to simulate the skin effect loss [53]. An approximate formula is presented for solid round conductors, and a convolution technique is applied to update E/H field components around the wire. However, this approach is difficult to be applied in a coaxial structure. Furthermore, SIBC bears weakness in solving low frequency or broadband EM problems. Several coaxial cable models have been also proposed to improve the calculation efficiency in the FDTD simulation. In [54], a coaxial cable model is proposed by means of the hybrid transmission line theory and the FDTD algorithm. However, the skin effect cannot be considered in the model, and the currents in its inner and

outer conductors have to be balanced. In [55], the transmission line is represented by a two-port circuit in the FDTD region. Though this model can deal with the frequency dependent issue, it is inconvenient to handle field coupling among cables or conductors, which do not run in parallel.

The thin-wire modeling techniques [46] based on the separated mesh method construct the thin-wire model in an additional mesh. This mesh is obtained from the FDTD mesh by the trilinear interpolation and in-cell inductance technique, and it is relatively independent on the FDTD mesh. As a result, this group of thin-wire models has the potential to simulate transients in inclined conductors with desirable performance [47, 56-58]. With these techniques, the insulated wire model [59] and the coaxial conductor model [60] have been proposed recently. However, the frequency-dependent characteristic of the inclined conductors was not taken into account. In addition, the bidirectional coupling between the core and sheath conductors, as well as eddy current in the sheath conductor was not considered in the existing model for the inclined conductors [60].

Originally the thin wire models were developed for circular wires [46, 48, 49]. Later they were invoked to model the wires with rectangular cross sections by modifying either correction factors [52] or E field distribution nearby [61, 62]. Note in these models, the current is uniformly distributed on the wire cross section. Therefore, the EM effects of a physical conductor, such as skin effect, cannot be modeled appropriately. Recently two extended thin wire models [63, 64] have been

introduced to take into account the skin effect in circular conductors including coaxial cables. These models, however, have a limited value in the transient analysis application in which the line structures with non-circular cross sections are involved.

1.3 Objectives of this thesis

This thesis aims at developing a series of extended thin wire models in the FDTD method taking into account frequency dependent loss, arbitrary inclination and non-circular cross section. These extended thin wire models are constructed by embedding other numerical methods and the analytical formulas of non-linear characteristic curves into the classical FDTD mesh. The electromagnetic coupling is considered in the FDTD domain with the FDTD method. The electromagnetic propagation within thin wire structures is evaluated by other methods. With these proposed models, the accuracy of the calculation can be retained. Meanwhile, the advantages of straightforward and less time consumption can be reserved since the model is constructed in a coarse FDTD mesh.

The extended thin wire models are then applied to analyze surge behaviors in 1) a building distribution system; 2) a lightning observation tower and 3) an electrified railway system. Simulations of building distribution systems are performed to study the induced surges in the distribution circuits. Different circuit parameters are considered in the study, and their impact on the induced surges is revealed. The impact of loads connected to the circuits is investigated as well. For

the lightning observation tower, the current distribution within the tower is analyzed first. The ground potential rise of the tower and step voltage in the vicinity of the tower then are calculated under different tower configurations. The FDTD method also analyzes the lightning surges in a light railway system. The surge voltage on the diode boxes between the fault current return wire and the rails is evaluated under both direct lightning and indirect lightning. The impact of various influential factors is discussed, including the lightning striking point, return stroke current waveform, grounding mesh of structures nearby and soil conductivity.

The main contributions of this thesis are listed as follows:

1) An extended thin wire model is proposed to simulate lossy wire structures with considering frequency dependent parameters. Solid wires, hollow tubes and coaxial cables can be simulated with satisfied accuracy. And the computation resource requirement and calculation time are effectively reduced compared with the traditional method.

2) An inclined thin wire model is developed with considering frequency dependent parameters. With this model, the wire structure can be arranged along arbitrary directions. The errors of propagation speed and waveform amplitude are lower than 1% and 3%. Compared with the staircase approximation, this model has a better performance.

3) An extended thin-wire model is proposed to simulate thin wire structures with non-circular cross sections. Frequency dependent parameters are considered with reasonable accuracy. Wire structures which are not designed to carry current in the operation, such as tracks in the railway system and beams in the building structure, can be analyzed under lightning strokes and fault conditions.

4) An advanced sub-cell method is developed to simulate thin wire structures with complexed effects. With this method, the calculation of EM field inside the wire structure is separated from the main FDTD calculation. It is easy to represent the complexed thin wire structures with desired methods without modifying the normal FDTD updating equations.

5) Frequency dependent parameters can be considered in the time domain analysis using the vector fitting technique which can be embedded into the time domain simulation in a convolutional way.

6) Both electric field and magnetic vector potential are employed to evaluate the voltage difference between two points. Without taking into account the magnetic vector potential in the voltage measurement in the FDTD method, a considerable error will be observed in the high frequency range.

7) An FDTD software package is provided on the MATLAB platform. Basic FDTD elements are available in the package. Three proposed thin wire

models are implemented. With the help of this software, lightning transients in practical systems can be simulated and analyzed.

1.4 Brief outlines

Chapter 2 reviews basic FDTD algorithms, including updating equations, stable conditions, lumped elements and three kinds of absorbing boundary conditions. Four conventional thin wire model techniques are reviewed as well.

Chapter 3 proposes an extended thin wire model for simulating wave or surge propagation on a lossy wire structure. A time-domain cascade circuit is developed to represent the wire structure, and the skin effect is fully considered in the circuit modelling. This circuit is integrated into a traditional thin-wire model in the FDTD simulation, and the updating equations are derived for solid round wires, hollow cylindrical tubes, and coaxial cables with and without conductors being bonded.

Chapter 4 presents a series of inclined thin-wire models considering frequency-dependent losses for solid conductors, hollow tubes and coaxial conductors with reasonable accuracy. The Bessel functions and the vector fitting technique are adopted to incorporate the frequency-dependent parameters of the conductors into the time-domain auxiliary equations. Transmission line equations of coaxial conductors are established for wave propagation analysis and linking the wire structure current and conductor currents together. Boundary conditions for the coaxial wire structure are provided as well.

Chapter 5 proposes an FDTD thin wire model with the equivalent circuit and surface charge simulation methods to simulate lossy thin wire conductors with arbitrary cross sections, such as rectangular shape, H-shape, cross shape, L-shape, T-shape, U-shape and others. In this method, frequency-dependent and position-variant field quantities are evaluated with the surface charge simulation method and equivalent circuit method in the initialization process. Time-domain field correction factors are obtained with the vector fitting technique. The frequency-dependent conductor loss is fully considered by four-separated E field components, which are also obtained with the vector fitting technique. All the frequency dependent parameters are embedded in the FDTD calculation in a convolutional approach. General guidelines on wire zone meshing are provided as well.

Chapter 6, 7 and 8 describes three simulation cases with applying proposed thin wire models. In Chapter 6, lightning-induced surges in building distribution circuits were investigated. In chapter 7, a meteorological (lightning) observation tower was analyzed with the FDTD method. In chapter 8, voltage surges between rail tracks and FCRW in a light rail system under lightning strokes are analyzed by the FDTD method.

Finally, chapter 9 concludes the whole thesis and summarizes some meaningful topics which are worthwhile to be discussed in the future works.

2 The method of FDTD

2.1 Updating equations

The FDTD method, proposed by Yee [1] in 1966, solves Maxwell's equations explicitly in the time domain. In this method, the whole volume is meshed into hexahedral cells with an orthogonal structure. Both electric and magnetic field components defined on the hexahedral cells are updated alternately in differential form. This method is matrix-free and uses much less memory space. It has excellent broadband characteristics with a range from near-DC through the microwave to the visible light. Thanks also to its excellent parallelization characteristics, graphics processing units (GPU) can be conveniently applied to improve calculation efficiency.

The traditional FDTD method is based on Maxwell's equations. Within a source free space, Maxwell's equations are shown below

$$-\sigma_m \vec{H} - \mu \cdot \frac{\partial \vec{H}}{\partial t} = \nabla \times \vec{E}, \tag{2.1.1}$$

$$\sigma \cdot \vec{E} + \varepsilon \cdot \frac{\partial \vec{E}}{\partial t} = \nabla \times \vec{H}. \tag{2.1.2}$$

where E is the electric field component, H is the magnetic field component, ε is the electric permittivity, σ is the electric conductivity, μ is the magnetic permeability, σ_m is the equivalent magnetic resistivity. Expanding (2.1.1) and (2.1.2) into differential form in X/Y/Z directions, Maxwell's equations can be rearranged into (2.1.3) and (2.1.4). It is noticed that the differential of H field (E

field) in the time domain is related to the differential of E field (H field) in the space domain.

$$-\sigma_m Hx - \mu\frac{\partial Hx}{\partial t} = \frac{\partial Ez}{\partial y} - \frac{\partial Ey}{\partial z}\bigg|_{x=m\Delta x,\, y=(n+1/2)\Delta y,\, z=(p+1/2)\Delta z,\, t=q\Delta t} \tag{2.1.3a}$$

$$-\sigma_m Hy - \mu\frac{\partial Hy}{\partial t} = \frac{\partial Ex}{\partial z} - \frac{\partial Ez}{\partial x}\bigg|_{x=(m+1/2)\Delta x,\, y=n\Delta y,\, z=(p+1/2)\Delta z,\, t=q\Delta t} \tag{2.1.3b}$$

$$-\sigma_m Hz - \mu\frac{\partial Hz}{\partial t} = \frac{\partial Ey}{\partial x} - \frac{\partial Ex}{\partial y}\bigg|_{x=(m+1/2)\Delta x,\, y=(n+1/2)\Delta y,\, z=p\Delta z,\, t=q\Delta t} \tag{2.1.3c}$$

$$\sigma Ex + \varepsilon\frac{\partial Ex}{\partial t} = \frac{\partial Hz}{\partial y} - \frac{\partial Hy}{\partial z}\bigg|_{x=(m+1/2)\Delta x,\, y=n\Delta y,\, z=p\Delta z,\, t=(q+1/2)\Delta t} \tag{2.1.4a}$$

$$\sigma Ey + \varepsilon\frac{\partial Ey}{\partial t} = \frac{\partial Hx}{\partial z} - \frac{\partial Hz}{\partial x}\bigg|_{x=m\Delta x,\, y=(n+1/2)\Delta y,\, z=p\Delta z,\, t=(q+1/2)\Delta t} \tag{2.1.4b}$$

$$\sigma Ez + \varepsilon\frac{\partial Ez}{\partial t} = \frac{\partial Hy}{\partial x} - \frac{\partial Hx}{\partial y}\bigg|_{x=m\Delta x,\, y=n\Delta y,\, z=(p+1/2)\Delta z,\, t=(q+1/2)\Delta t} \tag{2.1.4c}$$

In order to represent (2.1.3) and (2.1.4) in simulation space, the whole working space is discretized into parallel hexahedron grid, which is called Yee grid, Those six field components, Ex, Ey, Ez, Hx, Hy, Hz are located in each Yee cell. The electric field components are located at edge centers of cubes along the edge direction. The magnetic field components are located at face centers of cubes and perpendicular to the surface. Each E field (H field) components are surrounded by 4 adjacent H field (E field) components, as shown in figure 2.1.

If the electromagnetic field values in every time-step in the time domain and in each cell size in space domain vary linearly, the updating equations of field

components can be obtained conveniently by rearranging (2.1.3) (2.1.4). Note, the central difference method is adopted in time differential items to make sure calculation accuracy.

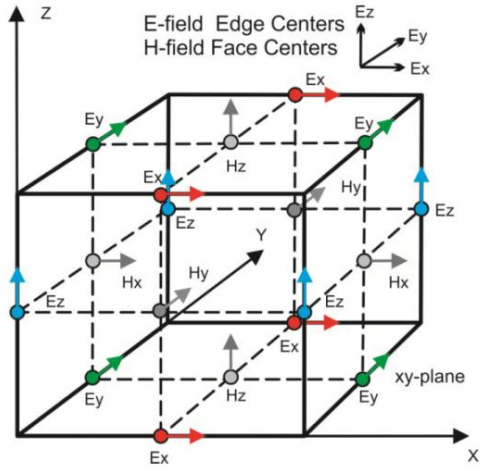

Figure 2.1 The Yee grid configuration

$$Hx^{q+1/2}_{m,n+1/2,p+1/2}=\frac{2\mu-\sigma_m\Delta t}{2\mu+\sigma_m\Delta t}Hx^{q-1/2}_{m,n+1/2,p+1/2}+\frac{2}{2\mu+\sigma_m\Delta t}\left[\begin{array}{l}\frac{\Delta t}{\Delta z}\left(Ey^{q}_{m,n+1/2,p+1}-Ey^{q}_{m,n+1/2,p}\right)\\-\frac{\Delta t}{\Delta y}\left(Ez^{q}_{m,n+1,p+1/2}-Ez^{q}_{m,n,p+1/2}\right)\end{array}\right] \quad (2.1.5a)$$

$$Hy^{q+1/2}_{m+1/2,n,p+1/2}=\frac{2\mu-\sigma_m\Delta t}{2\mu+\sigma_m\Delta t}Hy^{q-1/2}_{m+1/2,n,p+1/2}+\frac{2}{2\mu+\sigma_m\Delta t}\left[\begin{array}{l}\frac{\Delta t}{\mu\Delta x}\left(Ez^{q}_{m+1,n,p+1/2}-Ez^{q}_{m,n,p+1/2}\right)\\-\frac{\Delta t}{\mu\Delta z}\left(Ex^{q}_{m+1/2,n,p+1}-Ex^{q}_{m+1/2,n,p}\right)\end{array}\right] (2.1.5b)$$

$$Hz^{q+1/2}_{m+1/2,n+1/2,p}=\frac{2\mu-\sigma_m\Delta t}{2\mu+\sigma_m\Delta t}Hz^{q-1/2}_{m+1/2,n+1/2,p}+\frac{2}{2\mu+\sigma_m\Delta t}\left[\begin{array}{l}\frac{\Delta t}{\mu\Delta y}\left(Ex^{q}_{m+1/2,n+1,p}-Ex^{q}_{m+1/2,n,p}\right)\\-\frac{\Delta t}{\mu\Delta x}\left(Ey^{q}_{m+1,n+1/2,p}-Ey^{q}_{m,n+1/2,p}\right)\end{array}\right] (2.1.5c)$$

$$Ex^{q+1}_{m+1/2,n,p}=\frac{2\varepsilon-\sigma\Delta t}{2\varepsilon+\sigma\Delta t}Ex^{q}_{m+1/2,n,p}+\frac{2}{2\varepsilon+\sigma\Delta t}\left[\begin{array}{l}\frac{\Delta t}{\Delta y}\left(Hz^{q+1/2}_{m+1/2,n+1/2,p}-Hz^{q+1/2}_{m+1/2,n-1/2,p}\right)\\-\frac{\Delta t}{\Delta z}\left(Hy^{q+1/2}_{m+1/2,n,p+1/2}-Hy^{q+1/2}_{m+1/2,n,p-1/2}\right)\end{array}\right] \quad (2.1.6a)$$

$$Ey^{q+1}_{m,n+1/2,p}=\frac{2\varepsilon-\sigma\Delta t}{2\varepsilon+\sigma\Delta t}Ey^{q}_{m,n+1/2,p}+\frac{2}{2\varepsilon+\sigma\Delta t}\left[\begin{array}{l}\frac{\Delta t}{\varepsilon\Delta z}\left(Hx^{q+1/2}_{m,n+1/2,p+1/2}-Hx^{q+1/2}_{m,n+1/2,p-1/2}\right)\\-\frac{\Delta t}{\varepsilon\Delta x}\left(Hz^{q+1/2}_{m+1/2,n+1/2,p}-Hz^{q+1/2}_{m-1/2,n+1/2,p}\right)\end{array}\right] \quad (2.1.6b)$$

$$Ez_{m,n,p+1/2}^{q+1} = \frac{2\varepsilon - \sigma\Delta t}{2\varepsilon + \sigma\Delta t} Ez_{m,n,p+1/2}^{q} + \frac{2}{2\varepsilon + \sigma\Delta t} \left[\begin{array}{l} \frac{\Delta t}{\varepsilon \Delta x} \left(Hy_{m+1/2,n,p+1/2}^{q+1/2} - Hy_{m-1/2,n,p+1/2}^{q+1/2} \right) \\ -\frac{\Delta t}{\varepsilon \Delta y} \left(Hx_{m,n+1/2,p+1/2}^{q+1/2} - Hx_{m,n-1/2,p+1/2}^{q+1/2} \right) \end{array} \right] \quad (2.1.6c)$$

During the updating process, E and H field components always have a half time-step discrepancy in the time domain. Setting appropriate parameters according to the simulation models, second-order results can be obtained after updating E and H several times.

2.2 Stable conditions

The FDTD method is a numerical computing method in both the time domain and space domain. So that the choice of the cell size, Δs, and the time step, Δt, plays an important role in the calculation. An impropriate setting may affect the accuracy and stability of the calculation results [2].

Δs is determined by both the object shapes and the expected wavelength. Inside and on the surface of the object, especially at corners or tips, enough cells should be separated to make sure a smooth field change. On the other hand, the cell size need also smaller than 1/20 of the expected wavelength at least. In some special cases, such as thin-wire models, the cell size is required to be chosen even smaller compared with the wavelength.

The maximum time step, Δt, is determined by sizes of the smallest cells in the working volume. It should satisfy the following condition, known as the Courant-Friedrichs-Lewy (CFL) condition [18].

$$\Delta t \le \frac{1}{c\sqrt{\frac{1}{(\Delta x)^2}+\frac{1}{(\Delta y)^2}+\frac{1}{(\Delta z)^2}}}. \tag{2.2.1}$$

where Δx, Δy, Δz are the cell sizes in X, Y, Z directions of the smallest cell. In the 2D domain, the cell size in the Z direction is regarded as infinitely large. So, the CFL condition reduced to,

$$\Delta t \le \frac{1}{c\sqrt{\frac{1}{(\Delta x)^2}+\frac{1}{(\Delta y)^2}}}. \tag{2.2.2}$$

Except for the time step and the cell size, other factors can also affect the simulation stability and accuracy issues, such as the absorbing boundary condition, sub-cell setting and non-uniform meshing.

2.3 Lumped elements

The lumped circuit elements are used frequently in practical electromagnetic problems. Usually, these elements are implemented by assigning a particular E vector based on the extended Maxwell equations[19].

The electric current flowing through these circuit elements can be represented by the impressed current density term, $\vec{J}$, in Maxwell's curl equation,

$$\nabla \times \vec{H} = \varepsilon \frac{\partial \vec{E}}{\partial t} + \sigma \vec{E} + \vec{J}. \tag{2.3.1}$$

Impressed current density is used to represent sources or known quantities, which induces the electric and magnetic fields in the computation domain. The passive lumped elements can be also incorporated into (2.3.1) by Ohm's law and

the nature of themselves [10].

2.3.1 Resistive voltage source

Without loss of generality, a voltage source in the Z direction is taken as an example. (2.3.1) can be presented as

$$\frac{\partial E_z}{\partial t} = \frac{1}{\varepsilon_z}\left(\frac{\partial H_y}{\partial x} - \frac{\partial H_x}{\partial y} - \sigma_z E_z - J_z\right). \tag{2.3.2}$$

By differencing (2.3.2), a discrete equation can be derived, similar to the classic FDTD equations

$$\frac{Ez_{i,j,k}^{n+1} - Ez_{i,j,k}^{n}}{\Delta t} = \frac{1}{\varepsilon_z}\frac{Hy_{i,j,k}^{n+\frac{1}{2}} - Hy_{i-1,j,k}^{n+\frac{1}{2}}}{\Delta x} - \frac{1}{\varepsilon_z}\frac{Hx_{i,j,k}^{n+\frac{1}{2}} - Hx_{i,j-1,k}^{n+\frac{1}{2}}}{\Delta y} - \frac{\sigma_z}{2\varepsilon_z}\left(Ez_{i,j,k}^{n+1} + Ez_{i,j,k}^{n}\right) - \frac{1}{\varepsilon_z}J_Z^{n+\frac{1}{2}}. \tag{2.3.3}$$

In the cell which is assigned a source, the electric field vector, Ez, and the impressed potential difference, ΔV, satisfy,

$$\overrightarrow{E_z} = -\nabla V. \tag{2.3.4}$$

The voltage source also meets the Ohm's law,

$$I = \frac{\Delta V + V_S}{R_S}, \tag{2.3.5}$$

where V_S is the impressed voltage source with a predetermined waveform, R_S is the source resistance. In (2.3.3), $\overrightarrow{J_{lz}}$ can be replaced by I in (2.3.5),

$$I^{n+\frac{1}{2}} = \Delta x \Delta y J_{iz}^{n+\frac{1}{2}}. \tag{2.3.6}$$

By inserting (2.3.4) (2.3.5) (2.3.6) into (2.3.3), the voltage source updating equation can be derived

$$Ez_{i,j,k}^{n+1} = \frac{2\varepsilon_z - \Delta t\sigma_z - \dfrac{\Delta t\Delta z}{R_S \Delta x\Delta y}}{2\varepsilon_z + \Delta t\sigma_z + \dfrac{\Delta t\Delta z}{R_S \Delta x\Delta y}} \times Ez_{i,j,k}^{n} + \frac{2\Delta t}{\left(2\varepsilon_z + \Delta t\sigma_z + \dfrac{\Delta t\Delta z}{R_S \Delta x\Delta y}\right)\Delta x} \times \left(Hy_{i,j,k}^{n+\frac{1}{2}} - Hy_{i-1,j,k}^{n+\frac{1}{2}} \right)$$
$$- \frac{2\Delta t}{\left(2\varepsilon_z + \Delta t\sigma_z + \dfrac{\Delta t\Delta z}{R_S \Delta x\Delta y}\right)\Delta y} \times \left(Hx_{i,j,k}^{n+\frac{1}{2}} - Hx_{i,j-1,k}^{n+\frac{1}{2}} \right) - \frac{2\Delta t}{\left(2\varepsilon_z + \Delta t\sigma_z + \dfrac{\Delta t\Delta z}{R_S \Delta x\Delta y}\right)\left(R_S \Delta x\Delta y\right)} \times V_S^{n+\frac{1}{2}}$$

(2.3.7)

2.3.2 Hard voltage source

Even though the voltage sources containing internal resistance is common and have practical meanings, the hard voltage sources do have widespread usage in the model simulation [65].

Implementing a hard voltage source can be achieved by assigning a voltage waveform to the electric field vector directly.

$$\overrightarrow{E_z} = -V_S \tag{2.3.8}$$

2.3.3 Current source

The lumped current source has the relationship as

$$I = I_S + \frac{\Delta V}{R_S} \tag{2.3.9}$$

where I_S is the implied current source, R_S is the source resistance. Incorporating (2.3.1) (2.3.4) (2.3.6) (2.3.9), the current source updating equation can be derived as below

$$Ez_{i,j,k}^{n+1}=\frac{2\varepsilon_z-\Delta t\sigma_z-\dfrac{\Delta t\Delta z}{R_S\Delta x\Delta y}}{2\varepsilon_z+\Delta t\sigma_z+\dfrac{\Delta t\Delta z}{R_S\Delta x\Delta y}}\times Ez_{i,j,k}^{n}+\frac{2\Delta t}{\left(2\varepsilon_z+\Delta t\sigma_z+\dfrac{\Delta t\Delta z}{R_S\Delta x\Delta y}\right)\Delta x}\times\left(Hy_{i,j,k}^{n+\frac{1}{2}}-Hy_{i-1,j,k}^{n+\frac{1}{2}}\right)$$
$$-\frac{2\Delta t}{\left(2\varepsilon_z+\Delta t\sigma_z+\dfrac{\Delta t\Delta z}{R_S\Delta x\Delta y}\right)\Delta y}\times\left(Hx_{i,j,k}^{n+\frac{1}{2}}-Hx_{i,j-1,k}^{n+\frac{1}{2}}\right)-\frac{2\Delta t}{\left(2\varepsilon_z+\Delta t\sigma_z+\dfrac{\Delta t\Delta z}{R_S\Delta x\Delta y}\right)\left(\Delta x\Delta y\right)}\times I_S^{n+\frac{1}{2}} \quad (2.3.10)$$

2.3.4 Hard current source

The inner resistance of an ideal current source is infinitely large in theory. By setting the resistance parameter in (2.3.9) and rearranging (2.3.10), the hard current source updating equation can be deduced as

$$Ez_{i,j,k}^{n+1}=\frac{2\varepsilon_z-\Delta t\sigma_z}{2\varepsilon_z+\Delta t\sigma_z}\times Ez_{i,j,k}^{n}+\frac{2\Delta t}{\left(2\varepsilon_z+\Delta t\sigma_z\right)\Delta x}\times\left(Hy_{i,j,k}^{n+\frac{1}{2}}-Hy_{i-1,j,k}^{n+\frac{1}{2}}\right)$$
$$-\frac{2\Delta t}{\left(2\varepsilon_z+\Delta t\sigma_z\right)\Delta y}\times\left(Hx_{i,j,k}^{n+\frac{1}{2}}-Hx_{i,j-1,k}^{n+\frac{1}{2}}\right)-\frac{2\Delta t}{2\varepsilon_z+\Delta t\sigma_z}\times I_S^{n+\frac{1}{2}}\Big/\Delta x\Delta y \quad (2.3.11)$$

2.3.5 Resistance

By setting the current source, I_S, to zero in (2.3.9) and modifying (2.3.10) correspondingly, the resistance updating equation can be derived as

$$Ez_{i,j,k}^{n+1}=\frac{2\varepsilon_z-\Delta t\sigma_z-\dfrac{\Delta t\Delta z}{R_S\Delta x\Delta y}}{2\varepsilon_z+\Delta t\sigma_z+\dfrac{\Delta t\Delta z}{R_S\Delta x\Delta y}}\times Ez_{i,j,k}^{n}+\frac{2\Delta t}{\left(2\varepsilon_z+\Delta t\sigma_z+\dfrac{\Delta t\Delta z}{R_S\Delta x\Delta y}\right)\Delta x}\times\left(Hy_{i,j,k}^{n+\frac{1}{2}}-Hy_{i-1,j,k}^{n+\frac{1}{2}}\right)$$
$$-\frac{2\Delta t}{\left(2\varepsilon_z+\Delta t\sigma_z+\dfrac{\Delta t\Delta z}{R_S\Delta x\Delta y}\right)\Delta y}\times\left(Hx_{i,j,k}^{n+\frac{1}{2}}-Hx_{i,j-1,k}^{n+\frac{1}{2}}\right) \quad (2.3.12)$$

2.3.6 Capacitor

The current-voltage nature of a capacitor can be described as

$$I = C\frac{d\Delta V}{dt}. \tag{2.3.13}$$

By discretizing the above equation in time, the current-voltage relation can be revised as

$$I^{n+\frac{1}{2}} = C\frac{\Delta V^{n+1} - \Delta V^{n}}{\Delta t}. \tag{2.3.14}$$

By cooperating (2.3.1) (2.3.4) (2.3.6) (2.3.14), the capacitor updating equation can be obtained as

$$\begin{aligned} Ez_{i,j,k}^{n+1} = {} & \frac{2\varepsilon_z - \Delta t\sigma_z - \dfrac{2C\Delta z}{\Delta x\Delta y}}{2\varepsilon_z + \Delta t\sigma_z + \dfrac{2C\Delta z}{\Delta x\Delta y}} \times Ez_{i,j,k}^{n} + \frac{2\Delta t}{\left(2\varepsilon_z + \Delta t\sigma_z + \dfrac{2C\Delta z}{\Delta x\Delta y}\right)\Delta x} \times \left(Hy_{i,j,k}^{n+\frac{1}{2}} - Hy_{i-1,j,k}^{n+\frac{1}{2}} \right) \\ & - \frac{2\Delta t}{\left(2\varepsilon_z + \Delta t\sigma_z + \dfrac{2C\Delta z}{\Delta x\Delta y}\right)\Delta y} \times \left(Hx_{i,j,k}^{n+\frac{1}{2}} - Hx_{i,j-1,k}^{n+\frac{1}{2}} \right) \end{aligned}. \tag{2.3.15}$$

2.3.7 Inductance

The current-voltage characteristic of the inductance is known as

$$V = L\frac{dI}{dt}. \tag{2.3.16}$$

Similarly, the above equation can be discretized in time using the central difference method,

$$\Delta V^{n} = \frac{L}{\Delta t}\left(I^{n+\frac{1}{2}} - I^{n-\frac{1}{2}} \right). \tag{2.3.17}$$

By inserting (2.3.4) and (2.3.6) into (2.3.17), the current density item containing the inductance parameter can be calculated

$$J_{iz}^{n+\frac{1}{2}} = J_{iz}^{n-\frac{1}{2}} + \frac{\Delta t\Delta z}{L\Delta x\Delta y}E_z^{n}. \tag{2.3.18}$$

By replacing (2.3.18) into (2.3.1) and arranging it into the classic FDTD equation form, the inductance updating equation can be derived as

$$Ez_{i,j,k}^{n+1} = \frac{2\varepsilon_z - \Delta t\sigma_z}{2\varepsilon_z + \Delta t\sigma_z} \times Ez_{i,j,k}^{n} + \frac{2\Delta t}{(2\varepsilon_z + \Delta t\sigma_z)\Delta x} \times \left(Hy_{i,j,k}^{n+\frac{1}{2}} - Hy_{i-1,j,k}^{n+\frac{1}{2}} \right) - \frac{2\Delta t}{(2\varepsilon_z + \Delta t\sigma_z)\Delta y} \times \left(Hx_{i,j,k}^{n+\frac{1}{2}} - Hx_{i,j-1,k}^{n+\frac{1}{2}} \right) - \frac{2\Delta t}{2\varepsilon_z + \Delta t\sigma_z} \times J_{iz}^{n+\frac{1}{2}} \quad (2.3.19)$$

2.4 Absorbing boundary conditions

In a working volume constructed in a Cartesian coordinate system, six planes of boundaries always need to be defined at the initial state of the simulation process. The boundary can be basically divided into three types: the perfect electrical conductor (PEC) boundary, the perfect magnetic conductor (PMC) boundary and the absorbing boundary.

The PEC boundary and the PMC boundary have the practical meaning in real-life, which reflect all the electric field components or the magnetic field components respectively. The realization of these two boundaries in the FDTD method is simple and straightforward. For the PEC boundary, one can only define the electric field components tangent to the boundary surface to be zero. Likewise, the PMC boundary can be defined by setting the corresponding magnetic field components to be zero.

In the majority of simulation cases, infinitely large space is required instead of a finite space. It requires the reflected electromagnetic field absorbed perfectly to imitate an open space. So, constructing a desirable absorbing boundary condition (ABC) is necessary and inevitable. In 1981, Gerrit Mur [20] presented the Mur absorbing boundary, which is quite comprehensible. LIAO absorbing boundary

[21] was proposed in 1984 and gained an extensive use for its easy-implement and good absorbing performance. In 1994, Berenger [22] first described the perfectly matched layer (PML) absorbing boundary. Even though the PML boundary requires comparatively large memory, it is adopted in a large number of FDTD models for its perfect features. Except for free space, some conductors or media in simulation models should also be extended to infinity. A better absorbing layer, called the convolutional perfectly matched layer (CPML) [23] was proposed in 2000, which can absorb the total incident wave theoretically.

2.4.1 Mur absorbing boundary conditions

According to Maxwell's equations, the wave equation of the electric field can be derived in a source-free region

$$\nabla^2 E - \frac{1}{c^2} \cdot \frac{\partial^2 E}{\partial t^2} = 0 , \tag{2.4.1}$$

where c is the velocity of light in the media. In 3D-FDTD structure, E field is a function of x, y, z, t, so the wave equation can be rearranged as,

$$\frac{\partial^2 E}{\partial x^2} + \frac{\partial^2 E}{\partial y^2} + \frac{\partial^2 E}{\partial z^2} - \frac{1}{c^2} \cdot \frac{\partial^2 E}{\partial t^2} = 0 \tag{2.4.2}$$

For the sake of convenience, an operator is introduced here, which is defined as

$$L = \frac{\partial^2}{\partial x^2} + \frac{\partial^2}{\partial y^2} + \frac{\partial^2}{\partial z^2} - \frac{1}{c^2} \cdot \frac{\partial^2}{\partial t^2} = D_x^2 + D_y^2 + D_z^2 - \frac{1}{c^2} \cdot D_t^2 \tag{2.4.3}$$

To analyze the propagation of the electric field in the x direction, the wave equation can be written as

$$L \cdot E = L^- \cdot L^+ \cdot E = 0 , \tag{2.4.4}$$

where $L^- = D_x - \frac{D_t}{c^2}\sqrt{1-S^2}$, (2.4.5a)

$$L^+ = D_x + \frac{D_t}{c^2}\sqrt{1-S^2}, \quad (2.4.5b)$$

$$S = \frac{c\sqrt{D_y^2 + D_z^2}}{D_t}. \quad (2.4.5c)$$

L^- is used to descript E field propagation along the negative xxaxis, and L^+ is used to descript E field propagation along the positive xxaxis. Based on the Taylor expansion,

$$\sqrt{1-S^2} = 1 + \frac{1}{2}S^2 + \ldots., \quad (2.4.6)$$

The 1st-order Mur ABC and 2nd-order Mur ABC can be derived. For the 1st-order Mur absorbing boundary condition accuracy, the Taylor expansion only considers the first term of the result.

$$\sqrt{1-S^2} = 1 \quad (2.4.7)$$

Table 2.1 The equation which the 1st-order Mur ABC needs to be satisfied

Boundary	Equations need to satisfy
X=0	$\frac{\partial E}{\partial x} - \frac{1}{c}\cdot\frac{\partial E}{\partial t} = 0$
X=MaxX	$\frac{\partial E}{\partial x} + \frac{1}{c}\cdot\frac{\partial E}{\partial t} = 0$
Y=0	$\frac{\partial E}{\partial y} - \frac{1}{c}\cdot\frac{\partial E}{\partial t} = 0$
Y= MaxY	$\frac{\partial E}{\partial y} + \frac{1}{c}\cdot\frac{\partial E}{\partial t} = 0$
Z=0	$\frac{\partial E}{\partial y} - \frac{1}{c}\cdot\frac{\partial E}{\partial t} = 0$
Z= MaxZ	$\frac{\partial E}{\partial y} + \frac{1}{c}\cdot\frac{\partial E}{\partial t} = 0$

Then the operator, L, is modified from (2.4.5) as

$$L^- = D_x - \frac{D_t}{c^2} \quad (2.4.8a)$$

$$L^{+} = D_x + \frac{D_t}{c^2} \tag{2.4.8b}$$

Each axis in a Cartesian coordinate system has two boundaries perpendicular with it. Using 0 denotes the negative side boundary, and Max denotes the positive side boundary. At the x=0 boundary, in order to make sure the E field propagates along the negative x axis is absorbed, the following equation needs to be satisfied

$$L^{-} \cdot E = \left(D_x - \frac{D_t}{c^2} \right) \cdot E = \frac{\partial E}{\partial x} - \frac{1}{c} \cdot \frac{\partial E}{\partial t} = 0 \tag{2.4.9}$$

Likewise, the other boundaries also need to satisfy corresponding equations.

According to table 2.1, the updating equation in six boundaries can be derived and arranged in the classic FDTD format. In the X=0 boundary,

$$Ey^{q+1}_{1,1:MaxY-1,1:MaxZ} = Ey^{q}_{2,1:MaxY-1,1:MaxZ} + \frac{c_0\Delta t - \Delta x}{c_0\Delta t + \Delta x} \begin{pmatrix} Ey^{q+1}_{2,1:MaxY-1,1:MaxZ} \\ -Ey^{q}_{1,1:MaxY-1,1:MaxZ} \end{pmatrix}, \tag{2.4.10a}$$

$$Ez^{q+1}_{1,1:MaxY,1:MaxZ-1} = Ez^{q}_{2,1:MaxY,1:MaxZ-1} + \frac{c_0\Delta t - \Delta x}{c_0\Delta t + \Delta x} \begin{pmatrix} Ez^{q+1}_{2,1:MaxY,1:MaxZ-1} \\ -Ez^{q}_{1,1:MaxY,1:MaxZ-1} \end{pmatrix}. \tag{2.4.10b}$$

On the X=MaxX boundary,

$$Ey^{q+1}_{MaxX,1:MaxY-1,1:MaxZ} = Ey^{q}_{MaxX-1,1:MaxY-1,1:MaxZ} + \frac{c_0\Delta t - \Delta x}{c_0\Delta t + \Delta x} \begin{pmatrix} Ey^{q+1}_{MaxX-1,1:MaxY-1,1:MaxZ} \\ -Ey^{q}_{MaxX,1:MaxY-1,1:MaxZ} \end{pmatrix}, \tag{2.4.11a}$$

$$Ez^{q+1}_{MaxX,1:MaxY,1:MaxZ-1} = Ez^{q}_{MaxX-1,1:MaxY,1:MaxZ-1} + \frac{c_0\Delta t - \Delta x}{c_0\Delta t + \Delta x} \begin{pmatrix} Ez^{q+1}_{MaxX-1,1:MaxY,1:MaxZ-1} \\ -Ez^{q}_{MaxX,1:MaxY,1:MaxZ-1} \end{pmatrix}. \tag{2.4.11b}$$

On the Y=0 boundary,

$$Ex^{q+1}_{1:MaxX-1,1,1:MaxZ} = Ex^{q}_{1:MaxX-1,2,1:MaxZ} + \frac{c_0\Delta t - \Delta y}{c_0\Delta t + \Delta y} \begin{pmatrix} Ex^{q+1}_{1:MaxX-1,2,1:MaxZ} \\ -Ex^{q}_{1:MaxX-1,1,1:MaxZ} \end{pmatrix}, \tag{2.4.12a}$$

$$Ez^{q+1}_{1:MaxX,1,1:MaxZ-1} = Ez^{q}_{1:MaxX,2,1:MaxZ-1} + \frac{c_0\Delta t - \Delta y}{c_0\Delta t + \Delta y} \begin{pmatrix} Ez^{q+1}_{1:MaxX,2,1:MaxZ-1} \\ -Ez^{q}_{1:MaxX,1,1:MaxZ-1} \end{pmatrix}. \tag{2.4.12b}$$

On the Y=MaxY boundary,

$$Ex^{q+1}_{1:MaxX-1,MaxY,1:MaxZ} = Ex^{q}_{1:MaxX-1,MaxY-1,1:MaxZ} + \frac{c_0\Delta t-\Delta y}{c_0\Delta t+\Delta x}\begin{pmatrix} Ex^{q+1}_{1:MaxX-1,MaxY-1,1:MaxZ} \\ -Ex^{q}_{1:MaxX-1,MaxY,1:MaxZ}\end{pmatrix}, \tag{2.4.13a}$$

$$Ez^{q+1}_{1:MaxX,MaxY,1:MaxZ-1} = Ez^{q}_{1:MaxX,MaxY-1,1:MaxZ-1} + \frac{c_0\Delta t-\Delta y}{c_0\Delta t+\Delta y}\begin{pmatrix} Ez^{q+1}_{1:MaxX,MaxY-1,1:MaxZ-1} \\ -Ez^{q}_{1:MaxX,MaxY,1:MaxZ-1}\end{pmatrix}. \tag{2.4.13b}$$

On the Z=0 boundary,

$$Ex^{q+1}_{1:MaxX-1,1:MaxY,1} = Ex^{q}_{1:MaxX-1,1:MaxY,2} + \frac{c_0\Delta t-\Delta z}{c_0\Delta t+\Delta z}\begin{pmatrix} Ex^{q+1}_{1:MaxX-1,1:MaxY,2} \\ -Ex^{q}_{1:MaxX-1,1:MaxY,1}\end{pmatrix}, \tag{2.4.14a}$$

$$Ey^{q+1}_{1:MaxX,1:MaxY-1,1} = Ey^{q}_{1:MaxX,1:MaxY-1,2} + \frac{c_0\Delta t-\Delta z}{c_0\Delta t+\Delta z}\begin{pmatrix} Ey^{q+1}_{1:MaxX,1:MaxY-1,2} \\ -Ey^{q}_{1:MaxX,1:MaxY-1,1}\end{pmatrix}. \tag{2.4.14b}$$

On the Z=MaxZ boundary,

$$Ex^{q+1}_{1:MaxX-1,1:MaxY,MaxZ} = Ex^{q}_{1:MaxX-1,1:MaxY,MaxZ-1} + \frac{c_0\Delta t-\Delta z}{c_0\Delta t+\Delta z}\begin{pmatrix} Ex^{q+1}_{1:MaxX-1,1:MaxY,MaxZ-1} \\ -Ex^{q}_{1:MaxX-1,1:MaxY,MaxZ}\end{pmatrix}, \tag{2.4.15a}$$

$$Ey^{q+1}_{1:MaxX,1:MaxY-1,MaxZ} = Ey^{q}_{1:MaxX,1:MaxY-1,MaxZ-1} + \frac{c_0\Delta t-\Delta z}{c_0\Delta t+\Delta z}\begin{pmatrix} Ey^{q+1}_{1:MaxX,1:MaxY-1,MaxZ-1} \\ -Ey^{q}_{1:MaxX,1:MaxY-1,MaxZ}\end{pmatrix}. \tag{2.4.15b}$$

Normally, the 1st-order Mur ABC cannot meet the absorbing requirement. The 2nd-order Mur ABC with better absorbing performance may be required, though it is more complex.

For the 2nd-order Mur ABC, two terms of the result of the Taylor expansion are considered

$$\sqrt{1-S^2} = 1+\frac{1}{2}S^2. \tag{2.4.16}$$

Then (2.4.5a) and (2.4.5b) can be modified as

$$L^- = D_x - \frac{D_t}{c^2}\cdot\left(1-\frac{1}{2}S^2\right), \tag{2.4.17a}$$

$$L^+ = D_x + \frac{D_t}{c^2}\cdot\left(1-\frac{1}{2}S^2\right). \tag{2.4.17b}$$

Similarly, the equations that the electric field components in the six boundaries

need to be satisfied can also be derived according to (2.4.17a) and (2.4.17b).

Table 2.2 The equations which the 2nd-order Mur ABC needs to be satisfied

Boundary	Equations need to satisfy
X=0	$\frac{\partial^2 E}{\partial t \partial x} - \frac{1}{c}\frac{\partial^2 E}{\partial t^2} + \frac{c}{2}\left(\frac{\partial^2 E}{\partial y^2} + \frac{\partial^2 E}{\partial z^2}\right) = 0$
X=MaxX	$\frac{\partial^2 E}{\partial t \partial x} + \frac{1}{c}\frac{\partial^2 E}{\partial t^2} - \frac{c}{2}\left(\frac{\partial^2 E}{\partial y^2} + \frac{\partial^2 E}{\partial z^2}\right) = 0$
Y=0	$\frac{\partial^2 E}{\partial t \partial y} - \frac{1}{c}\frac{\partial^2 E}{\partial t^2} + \frac{c}{2}\left(\frac{\partial^2 E}{\partial x^2} + \frac{\partial^2 E}{\partial z^2}\right) = 0$
Y= MaxY	$\frac{\partial^2 E}{\partial t \partial y} + \frac{1}{c}\frac{\partial^2 E}{\partial t^2} - \frac{c}{2}\left(\frac{\partial^2 E}{\partial x^2} + \frac{\partial^2 E}{\partial z^2}\right) = 0$
Z=0	$\frac{\partial^2 E}{\partial t \partial z} - \frac{1}{c}\frac{\partial^2 E}{\partial t^2} + \frac{c}{2}\left(\frac{\partial^2 E}{\partial x^2} + \frac{\partial^2 E}{\partial y^2}\right) = 0$
Z= MaxZ	$\frac{\partial^2 E}{\partial t \partial z} + \frac{1}{c}\frac{\partial^2 E}{\partial t^2} - \frac{c}{2}\left(\frac{\partial^2 E}{\partial x^2} + \frac{\partial^2 E}{\partial y^2}\right) = 0$

2.4.2 LIAO absorbing boundary conditions

The LIAO absorbing boundary condition gained widespread use since it was proposed. This absorbing technic is easy to be implemented and requires less memory space. For the waves propagate from any angle, the LIAO ABC shows a remarkable performance. Unlike the Mur ABC which realizes the wave absorption by modifying electric field components tangential to the boundary surface, the LIAO ABC calculates the E vector vertical to the boundary.

In the FDTD calculation space, each field component is a two-argument function, location in axis and time. Taking E_x as an example, the M_{th}-order error at

location x and time t can be represented using the backward difference,

$$\Delta^M E_X(t,x) = \Delta^{M-1} E_X(t, x-\alpha c\Delta t) - \Delta^{M-1} E_X(t-\Delta t, x-2\alpha c\Delta t), \quad (2.4.18)$$

where c is the velocity of light, Δt is the time step chosen in FDTD setting, α is the artificial transmitting coefficient within a range of (0, 2). The 0_{th}-order error is defined as

$$\Delta^0 E_X(t,x) = E_X(t, x-\alpha c\Delta t). \quad (2.4.19)$$

The Mth-order error of E_x can be expressed by recurring (2.4.18) from the 0th-order to Mth-order as

$$\Delta^M E_x(t, x-\alpha c\Delta t) = \sum_{i=1}^{M+1} (-1)^{i+1} C_{i-1}^M E_x\left[t-(i-1)\Delta t, x-i\alpha c\Delta t\right]. \quad (2.4.20)$$

where C_i^M is a binomial coefficient. Neglecting the higher order error waves, the E_x at the next time step can be expressed as

$$E_x(t+\Delta t, x) \approx \sum_{i=1}^{N} \Delta^{i-1} E_x(t, x-\alpha c\Delta t) = \sum_{i=1}^{N} (-1)^{i+1} C_i^N E_x\left[t-(i-1)\Delta t, x-i\alpha c\Delta t\right]. \quad (2.4.21)$$

According to (2.4.21), the LIAO ABC with the 2_{nd}-order accuracy can be obtained

$$E_x(x, t+\Delta t) = 2E_x(x-\Delta x, t) - E_x(x-2\Delta x, t-\Delta t). \quad (2.4.22)$$

Similarly, the 4_{th}-order LIAO ABC is presented as

$$\begin{aligned} E_x(x,t+\Delta t) &= 4E_x(x-\Delta x,t) - 6E_x(x-2\Delta x,t-\Delta t) \\ &+4E_x(x-3\Delta x,t-2\Delta t) - 4E_x(x-4\Delta x,t-3\Delta t) \end{aligned}. \quad (2.4.23)$$

Though the LIAO ABC has a good absorbing performance with less memory requirement and easy implementation features, an instability exists in the LIAO boundary calculation after certain time steps. Wagner and Chew [66] declaimed in

1995 that the instability problem of the LIAO ABC may be caused by the theoretical value of the pole of reflection coefficient cannot be located in the unit circle of the complex plane.

Lei Zhang [67] proposed an easy method for improving LIAO ABC stability performance. Two different orders of the LIAO boundary are incorporated by a weighting factor, a, and the expression is shown as

$$\begin{aligned} E_x(t+\Delta t,x) \approx (1-a)\sum_{i=1}^{N}(-1)^{i+1} C_i^N E_x\left[t-(i-1)\Delta t, x-i\alpha c\Delta t\right] \\ +a\sum_{i=1}^{M}(-1)^{i+1} C_i^M E_x\left[t-(i-1)\Delta t, x-i\alpha c\Delta t\right] \end{aligned}, \tag{2.4.24}$$

where M and N are two different orders of the boundary. The weighting factor, a, varies between 0 and 1. Taking the 2nd-order and the 4th-order LIAO ABC as an example, with a=0.8, the boundary updating equation is represented as

$$\begin{aligned} E_x(x,t+\Delta t) = (4\times 0.8+2\times 0.2)E_x(x-\Delta x,t)-(6\times 0.8+1\times 0.2)E_x(x-2\Delta x,t-\Delta t) \\ +(4\times 0.8)E_x(x-3\Delta x,t-2\Delta t)-(4\times 0.8)E_x(x-4\Delta x,t-3\Delta t) \end{aligned}. \tag{2.4.25}$$

2.4.3 Perfectly matched layer absorbing boundary conditions

The perfectly matched layer (PML) ABC is a big improvement in the FDTD absorbing boundary evolution. The outstanding absorbing performance fits in nearly all occasions, such as non-uniform mesh, dispersive media. The PML ABC is realized by implementing a special media beside PEC boundaries, which can let the incident waves penetrate in perfectly without any reflection for all frequency and attenuate the waves inside the media exponentially.

As for the theory of PML at the vacuum-PML interface, consider the TEz

polarized plane wave propagating in an arbitrary direction, as shown in figure 2.2, field components can be expressed in the time-harmonic domain as

$$E_x = -E_0 \sin\phi_0 e^{j\omega(t-\alpha x-\beta y)}, \tag{2.4.26a}$$

$$E_y = E_0 \cos\phi_0 e^{j\omega(t-\alpha x-\beta y)}, \tag{2.4.26b}$$

$$H_z = H_0 e^{j\omega(t-\alpha x-\beta y)}. \tag{2.4.26c}$$

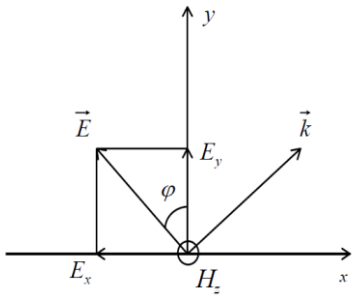

Figure 2.2 the TEz polarized plane wave propagating in an arbitrary direction

The Maxwell's equations for a TEz polarized wave are

$$\varepsilon_0 \frac{\partial E_x}{\partial t} + \sigma E_x = \frac{\partial H_z}{\partial y}, \tag{2.4.27a}$$

$$\varepsilon_0 \frac{\partial E_y}{\partial t} + \sigma E_y = -\frac{\partial H_z}{\partial x}, \tag{2.4.27b}$$

$$\mu_0 \frac{\partial H_z}{\partial t} + \sigma_m H_z = \frac{\partial E_x}{\partial y} - \frac{\partial E_y}{\partial x}. \tag{2.4.27c}$$

In a TEz PML medium, Hz can be broken into two artificial components associated with the x and y directions as

$$H_{zx} = H_{zx0} e^{j\omega(t-\alpha x-\beta y)} = H_{zx0} e^{j\omega\beta y} e^{j\omega(t-\alpha x)}, \tag{2.4.28a}$$

$$H_{zy} = H_{zy0} e^{j\omega(t-\alpha x-\beta y)} = H_{zx0} e^{j\omega\alpha x} e^{j\omega(t-\beta y)}, \tag{2.4.28b}$$

where $H_z = H_{zx} + H_{zy}$. Therefore, a modified set of Maxwell's equations (2.4.27) for a TEz polarized PML medium can be expressed as

$$\varepsilon_0 \frac{\partial E_x}{\partial t} + \sigma_{pey} E_x = \frac{\partial (H_{zx} + H_{zy})}{\partial y}, \tag{2.4.29a}$$

$$\varepsilon_0 \frac{\partial E_y}{\partial t} + \sigma_{pex} E_y = -\frac{\partial (H_{zx} + H_{zy})}{\partial x}, \tag{2.4.29b}$$

$$\mu_0 \frac{\partial H_{zx}}{\partial t} + \sigma_{pmx} H_{zx} = -\frac{\partial E_y}{\partial x}, \tag{2.4.29c}$$

$$\mu_0 \frac{\partial H_{zy}}{\partial t} + \sigma_{pmy} H_{zy} = \frac{\partial E_x}{\partial y}, \tag{2.4.29d}$$

where σ_{pex}, σ_{pey}, σ_{pmx}, and σ_{pmy} are the introduced fictitious conductivities. When $\sigma_{pmx}=\sigma_{pmy}=\sigma_m$, equations (2.4.29) can be merged and yields (2.4.27). When the electric and magnetic losses are assigned to be zero, the field updating equations for the PML region become that of a vacuum region. Field components E_y and H_{zx} together can represent a wave propagating in the x direction, and field components of E_x and H_{zy} represent a wave propagating in the y direction. Substituting the field equations for the x and y propagating waves in (2.4.26) (2.4.28) into the modified Maxwell's equations (2.4.29), one can obtain

$$\varepsilon_0 E_0 \sin\phi_0 - j\frac{\sigma_{pey}}{\omega} E_0 \sin\phi_0 = \beta (H_{zx0} + H_{zy0}), \tag{2.4.30a}$$

$$\varepsilon_0 E_0 \cos\phi_0 - j\frac{\sigma_{pex}}{\omega} E_0 \cos\phi_0 = \alpha (H_{zx0} + H_{zy0}), \tag{2.4.30b}$$

$$\mu_0 H_{zx0} - j\frac{\sigma_{pmx}}{\omega} H_{zx0} = \alpha E_0 \cos\phi_0, \tag{2.4.30c}$$

$$\mu_0 H_{zy0} - j\frac{\sigma_{pmy}}{\omega} H_{zy0} = \beta E_0 \sin\phi_0. \tag{2.4.30d}$$

Using (2.4.30c) (2.4.30d) to eliminate magnetic field terms in equations (2.4.30a) and (2.4.30b) yields

$$\varepsilon_0 \mu_0 \left(1 - j\frac{\sigma_{pey}}{\varepsilon_0 \omega}\right) \sin\phi_0 = \beta \left[\frac{\alpha \cos\phi_0}{\left(1 - j\frac{\sigma_{pmx}}{\mu_0 \omega}\right)} + \frac{\beta \sin\phi_0}{\left(1 - j\frac{\sigma_{pmy}}{\mu_0 \omega}\right)}\right], \tag{2.4.31a}$$

$$\varepsilon_0\mu_0\left(1-j\frac{\sigma_{pex}}{\varepsilon_0\omega}\right)\sin\phi_0=\alpha\left[\frac{\alpha\cos\phi_0}{\left(1-j\frac{\sigma_{pmx}}{\mu_0\omega}\right)}+\frac{\beta\sin\phi_0}{\left(1-j\frac{\sigma_{pmy}}{\mu_0\omega}\right)}\right]. \tag{2.4.31b}$$

The unknown constants α, β can be obtained from (2.4.31) as

$$\alpha=\frac{\sqrt{\mu_0\varepsilon_0}}{G}\left(1-j\frac{\sigma_{pex}}{\omega\varepsilon_0}\right)\cos\phi_0, \tag{2.4.32a}$$

$$\beta=\frac{\sqrt{\mu_0\varepsilon_0}}{G}\left(1-j\frac{\sigma_{pey}}{\omega\varepsilon_0}\right)\sin\phi_0, \tag{2.4.32b}$$

where $G=\sqrt{w_x\cos^2\phi_0+w_y\sin^2\phi_0}$,

$$w_x=\left(1-j\frac{\sigma_{pex}}{\omega\varepsilon_0}\right)\Big/\left(1-j\frac{\sigma_{pmx}}{\omega\mu_0}\right),$$

$$w_y=\left(1-j\frac{\sigma_{pey}}{\omega\varepsilon_0}\right)\Big/\left(1-j\frac{\sigma_{pmy}}{\omega\mu_0}\right).$$

Therefore, the generalized field component can be expressed as

$$\psi=\psi_0 e^{j\omega\left(t-\frac{x\cos\phi_0+y\sin\phi_0}{cG}\right)}e^{-\frac{\sigma_{pex}\cos\phi_0}{\varepsilon_0 cG}x}e^{-\frac{\sigma_{pey}\sin\phi_0}{\varepsilon_0 cG}y}, \tag{2.4.33}$$

where the first exponential represents the phase of a plane wave and the second and third exponentials govern the decrease in the magnitude of the wave along the x axis and y axis, respectively.

Once α and β are determined by (2.4.32), the split magnetic field can be determined from (2.4.30c) (2.4.30d) as

$$H_{zx0}=E_0\sqrt{\frac{\varepsilon_0}{\mu_0}}\frac{w_x\cos^2\phi_0}{G}, \tag{2.4.34a}$$

$$H_{zy0}=E_0\sqrt{\frac{\varepsilon_0}{\mu_0}}\frac{w_y\sin^2\phi_0}{G}. \tag{2.4.34b}$$

The magnitude of the total magnetic field Hz is then given as

$$H_0 = H_{zx0} + H_{zy0} = E_0\sqrt{\frac{\varepsilon_0}{\mu_0}}G\,. \tag{2.4.35}$$

The wave impedance in a TEz PML medium can be expressed as

$$Z = \frac{E_0}{H_0} = \sqrt{\frac{\mu_0}{\varepsilon_0}}\frac{1}{G} \tag{2.4.36}$$

If the conductivity parameters are chosen such that

$$\frac{\sigma_{pex}}{\varepsilon_0} = \frac{\sigma_{pmx}}{\mu_0}\,, \tag{2.4.37a}$$

$$\frac{\sigma_{pey}}{\varepsilon_0} = \frac{\sigma_{pmy}}{\mu_0}\,, \tag{2.4.37b}$$

Then the term G becomes equal to unity as w_x and w_y becomes equal to unity. Therefore, the wave impedance of this PML medium becomes the same as that of the interior free space. In other words, when the constitutive conditions of (2.4.37) are satisfied, a TEz polarized wave can propagate from free space into the PML medium without reflection for all frequencies.

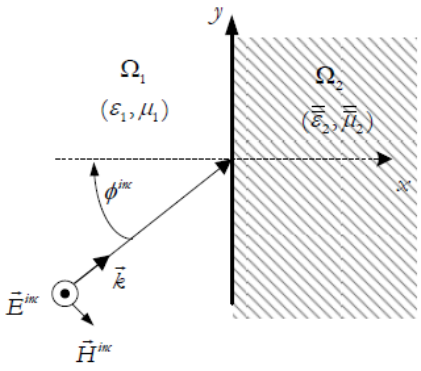

Figure 2.3 An arbitrary incident wave between two lossy media

The theory of PML at the PML-PML interface is different from the theory of

PML at the vacuum-PML interface. The reflection coefficient for an arbitrary incident wave between two lossy media, as shown in figure 2.3, can be expressed as

$$r_p = \frac{Z_2 \cos\phi_2 - Z_1 \cos\phi_1}{Z_2 \cos\phi_2 + Z_1 \cos\phi_1}, \tag{2.4.38}$$

where Z1 and Z2 are the intrinsic impedances of respective mediums. Applying (2.4.36), the reflection coefficient r_p becomes

$$r_p = \frac{G_1 \cos\phi_2 - G_2 \cos\phi_1}{G_1 \cos\phi_2 + G_2 \cos\phi_1}. \tag{2.4.39}$$

The Snell-Descartes law at the interface normal to x of two lossy media can be described as

$$\left(1 - i\frac{\sigma_{y1}}{\varepsilon_0 \omega}\right)\frac{\sin\phi_1}{G_1} = \left(1 - i\frac{\sigma_{y2}}{\varepsilon_0 \omega}\right)\frac{\sin\phi_2}{G_2}. \tag{2.4.40}$$

When the two media have the same conductivities, i.e. $\sigma_{pey1}=\sigma_{pey2}=\sigma_{pey}$, $\sigma_{pmy1}=\sigma_{pmy2}=\sigma_{pmy}$, (2.4.40) becomes

$$\frac{\sin\phi_1}{G_1} = \frac{\sin\phi_2}{G_2}. \tag{2.4.41}$$

Moreover, when (σ_{pex1}, σ_{pmx1}), (σ_{pex2}, σ_{pmx2}), and (σ_{pex}, σ_{pmx}) satisfy the matching condition in equation (2.4.37), G1=G2=1. Then (2.4.41) reduces to

$$\phi_1 = \phi_2. \tag{2.4.42}$$

And equation (2.4.39) reduces to

$$r_p = 0. \tag{2.4.43}$$

Therefore, when two PML media satisfy (2.4.37) and lie at an interface normal to the x axis with the same (σ_{pex}, σ_{pmx}), a wave can transmit through this interface

with no reflections theoretically, at any angle of incidence and any frequency.

However, if the two media have the same (σ_{pex}, σ_{pmx}) but do not satisfy (2.4.37), then the reflection coefficient becomes

$$r_p = \frac{\sin\phi_1 \cos\phi_2 - \sin\phi_2 \cos\phi_1}{\sin\phi_1 \cos\phi_2 + \sin\phi_2 \cos\phi_1}. \tag{2.4.44}$$

Substituting (2.4.41) into above equation, the reflection coefficient of two unmatched PML media becomes

$$r_p = \frac{\sqrt{w_{x1}} - \sqrt{w_{x2}}}{\sqrt{w_{x1}} + \sqrt{w_{x2}}}. \tag{2.4.45}$$

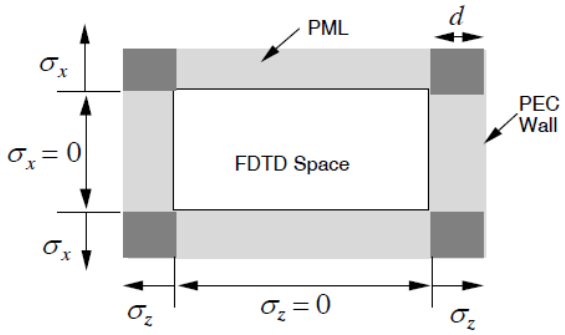

Figure 2.4 The PML implementation strategy in 2D space

Equation (2.4.45) shows that the reflection coefficient for two unmatched PML media is highly dependent on frequency, regardless of the incident angle. The analysis can be applied to two PML media lying at the interface normal to the y axis as well.

Based on the previous discussion, if a two-dimensional FDTD problem space is attached with an adequate thickness of PML media, the outgoing waves will be absorbed without any undesired numerical reflections. The PML regions must be

assigned appropriate conductivity values satisfying the matching condition (2.4.37); the positive and negative x boundaries of the PML regions have nonzero σ_{pex} and σ_{pmx}, whereas the positive and negative y boundaries of the PML regions have nonzero σ_{pey} and σ_{pmy} values. The coexistence of nonzero values of σ_{pex}, σ_{pmx}, σ_{pey} and σ_{pmy} is required at the four corner PML overlapping regions.

For a three-dimensional problem space, each field component of the electric and magnetic fields is broken into two field components similar to the two-dimensional case. These modified split electric field equations presented as below

$$\varepsilon_0 \frac{\partial E_{xy}}{\partial t} + \sigma_{pey} E_{xy} = \frac{\partial \left(H_{zx} + H_{zy} \right)}{\partial y}, \tag{2.4.46a}$$

$$\varepsilon_0 \frac{\partial E_{xz}}{\partial t} + \sigma_{pez} E_{xy} = -\frac{\partial \left(H_{yx} + H_{yz} \right)}{\partial z}, \tag{2.4.46b}$$

$$\varepsilon_0 \frac{\partial E_{yx}}{\partial t} + \sigma_{pex} E_{yx} = -\frac{\partial \left(H_{zx} + H_{zy} \right)}{\partial x}, \tag{2.4.46c}$$

$$\varepsilon_0 \frac{\partial E_{yz}}{\partial t} + \sigma_{pez} E_{yz} = \frac{\partial \left(H_{xy} + H_{xz} \right)}{\partial z}, \tag{2.4.46d}$$

$$\varepsilon_0 \frac{\partial E_{zx}}{\partial t} + \sigma_{pex} E_{zx} = \frac{\partial \left(H_{yx} + H_{yz} \right)}{\partial x}, \tag{2.4.46e}$$

$$\varepsilon_0 \frac{\partial E_{zy}}{\partial t} + \sigma_{pey} E_{zy} = -\frac{\partial \left(H_{xy} + H_{xz} \right)}{\partial y}. \tag{2.4.46f}$$

Likewise, the modified Maxwell's split magnetic field equations are

$$\mu_0 \frac{\partial H_{xy}}{\partial t} + \sigma_{pmy} H_{xy} = -\frac{\partial \left(E_{zx} + E_{zy} \right)}{\partial y}, \tag{2.4.47a}$$

$$\mu_0 \frac{\partial H_{xz}}{\partial t} + \sigma_{pmz} H_{xy} = \frac{\partial \left(E_{yx} + E_{yz} \right)}{\partial z}, \tag{2.4.47b}$$

$$\mu_0 \frac{\partial H_{yx}}{\partial t} + \sigma_{pmx} H_{yx} = \frac{\partial \left(E_{zx} + E_{zy} \right)}{\partial x}, \tag{2.4.47c}$$

$$\mu_0 \frac{\partial H_{yz}}{\partial t} + \sigma_{pmz} H_{yz} = -\frac{\partial \left(E_{xy} + E_{xz} \right)}{\partial z}, \tag{2.4.47d}$$

$$\mu_0 \frac{\partial H_{zx}}{\partial t} + \sigma_{pmx} H_{zx} = -\frac{\partial \left(E_{yx} + E_{yz} \right)}{\partial x}, \tag{2.4.47e}$$

$$\mu_0 \frac{\partial H_{zy}}{\partial t} + \sigma_{pmy} H_{zy} = \frac{\partial \left(E_{xy} + E_{xz} \right)}{\partial y}. \tag{2.4.47f}$$

Then the matching condition for a three-dimensional PML is given by

$$\frac{\sigma_{pex}}{\varepsilon_0} = \frac{\sigma_{pmx}}{\mu_0}, \tag{2.4.48a}$$

$$\frac{\sigma_{pey}}{\varepsilon_0} = \frac{\sigma_{pmy}}{\mu_0}, \tag{2.4.48a}$$

$$\frac{\sigma_{pez}}{\varepsilon_0} = \frac{\sigma_{pmz}}{\mu_0}. \tag{2.4.48a}$$

The PML regions must be assigned appropriate conductivity values satisfying the matching condition (2.4.48); the positive and negative x boundaries of PML regions have nonzero σ_{pex} and σ_{pmx}, the positive and negative y boundaries of PML regions have nonzero σ_{pey} and σ_{pmy}, the positive and negative z boundaries of PML regions have nonzero σ_{pez} and σ_{pmz}. The coexistence of nonzero values of σ_{pex}, σ_{pmx}, σ_{pey}, σ_{pmy}, σ_{pez} and σ_{pmz} is required at the PML overlapping regions.

The outer boundaries of the PML regions are terminated by PEC walls. When a finite-thickness PML medium backed by a PEC wall is adopted, an incident plane wave may not be totally attenuated within the PML region, and small reflections

to the interior domain from the PEC back wall may occur. For a finite-width PML medium where the conductivity distribution is uniform, there is an apparent reflection coefficient, which is expressed as

$$R(\phi_0) = e^{-2\frac{\sigma \cos\phi_0}{\varepsilon_0 c}\delta}, \tag{2.4.49}$$

where σ is the conductivity of the medium, δ is the thickness of the PML medium. The factor 2 in the exponent is due to the travel distance, which is twice the distance between the vacuum-PML interface and the PEC backing. Here the exponential term is the attenuation factor of the field magnitude of the plane wave as shown in equation (2.4.33). Form (2.4.49), the effectiveness of a finite-width PML is dependent on the losses within the PML medium.

Significant reflections were observed when constant uniform losses are assigned throughout the PML media, which is a result of the discrete approximation of fields and material parameters at the domain-PML interfaces and sharp variation of conductivity profiles. This mismatch problem can be tempered using a spatially gradually increasing conductivity distribution, which is zero at the domain-PML interface and tends to be a maximum conductivity σ_{max} at the end of the PML region. There are two major types of mathematical functions are proposed as the conductivity distributions or loss profiles: power and geometrically increasing functions.

1) The power increasing function

$$\sigma(\rho) = \sigma_{\max}\left(\frac{\rho}{\delta}\right)^{n_{pml}}, \tag{2.4.50}$$

$$\sigma_{\max} = -\frac{\left(n_{pml}+1\right)\varepsilon_0 c \ln\left(R(0)\right)}{2\Delta s N}. \tag{2.4.51}$$

where ρ is the distance from the computational domain-PML interface to the position of the field component, and δ is the thickness of the PML cell, and R(0) is the reflection coefficient of the finite-width PML medium at normal incidence. The distribution function is linear for n_{pml}=1 and parabolic for n_{pml}=2. To determine the conductivity profile using (2.4.50) the parameters R(0) and n_{pml} must be predefined. Usually n_{pml} takes a value such as 2, 3, or 4 and R(0) takes a very small value such as 10^{-8} for a satisfactory PML performance.

2) The geometrically increasing function

$$\sigma(\rho) = \sigma_0 g^{\frac{\rho}{\Delta s}}, \tag{2.4.52}$$

$$\sigma_0 = -\frac{\varepsilon_0 c \ln(g)}{2\Delta s g^N - 1} \ln\left(R(0)\right), \tag{2.4.53}$$

where the parameter g is a real number used for a geometrically increasing function.

2.5 Thin wire model review

FDTD method [1] is a powerful, straightforward and easy-implemented method for analyzing electromagnetic fields in the time domain. However, a trade-off exists between the accuracy and calculation burden especially for the simulation model containing small-sized structures. If a highly accurate result is required, large memory space and a long calculation time is inevitable. Likewise, a coarse Yee cell structure and a large time step may lead to an unacceptable accuracy. The thin wire model is one of the methods to alleviate this contradiction for the case of

modeling long wires with a small radius.

Four types of thin wire models will be reviewed here. The thin wire model proposed in [46] calculates the current and charge on the wire separately by the in-cell inductance technique and represents the wire as a series of equivalent current sources in the FDTD region. This model owns the advantages of dealing with oblique wires and multi-wire junctions [47]. In [48] special field updating formulas are presented by taking into account the field distribution pattern around the wire in the contour path integration. It is straightforward, however, the instability issues and inaccurate results may occur. The thin wire model in [49] is established using the intrinsic radius which is obtained with a numerical method. In case that the conductor radius is different from the intrinsic radius, material parameters are adjusted to match the required radius. This method is stable and easy implemented. In [52] the concept of line averaged quantities and surface averaged quantities are introduced in deriving the field updating equations. This model possesses advantages in dealing with thin wires with arbitrarily shaped cross sections

2.5.1 The Holland thin wire model

The Maxwell's equations in a source free space in differential form are represented as,

$$\nabla \times H = \varepsilon \frac{\partial E}{\partial t}, \tag{2.5.1}$$

$$\nabla \times E = -\mu \frac{\partial H}{\partial t}. \tag{2.5.2}$$

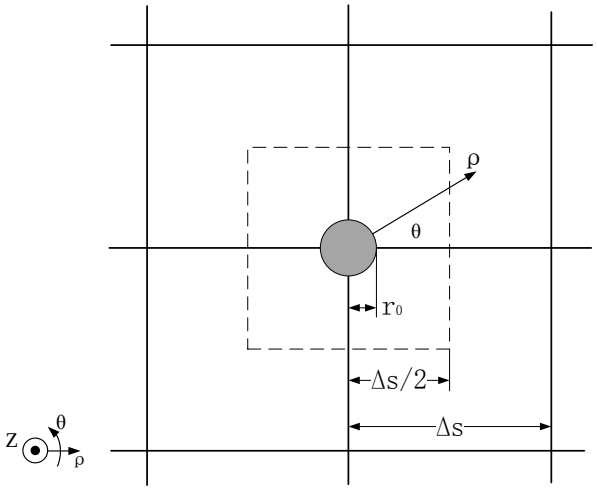

Figure 2.5 The configuration of the Holland thin wire model align with Z axis

Taking a simple geometry structure to illustrate the thin wire method. A thin wire is located aligned with the Z axis, and contains Ez field inside. A uniform mesh technique is adopted. The arrangement is shown in figure 2.5.

In a cylindrical coordinate system, radial electric field Eρ can be represented from (2.5.1) as,

$$\frac{1}{\rho}\frac{\partial Hz}{\partial \theta}-\frac{\partial H\theta}{\partial z}=\varepsilon\frac{\partial E\rho}{\partial t}. \tag{2.5.3}$$

Integrate (2.5.3) from 0 to 2π, the Hz term will be eliminated, and we can obtain

$$-\frac{\partial}{\partial z}\int_0^{2\pi} H\theta d\theta=\varepsilon\frac{\partial}{\partial t}\int_0^{2\pi} E\rho d\theta. \tag{2.5.4}$$

The circumferential magnetic field, Hθ, can be derived from (2.5.2) as

$$\frac{\partial E\rho}{\partial z}-\frac{\partial Ez}{\partial \rho}=-\mu\frac{\partial H\theta}{\partial t}. \tag{2.5.5}$$

By taking the integration of ρ from r0 to R, the electric field in a longitudinal direction can be expressed as

$$Ez(R) = \mu \frac{\partial}{\partial t} \int_{r0}^{R} H\theta d\rho + \frac{\partial}{\partial z} \int_{r0}^{R} E\rho d\rho \,. \tag{2.5.6}$$

Assuming the electromagnetic field nearby the conductor is quasi-static, and the thin wire is infinite long, the distribution of Hθ and Eρ can be assumed as,

$$\begin{aligned} H\theta(\rho) &= \frac{I}{2\pi\rho} \\ E\rho(\rho) &= \frac{Q}{2\pi\rho\varepsilon} \end{aligned}, \tag{2.5.7}$$

where I is the current flow through the conductor, Q is the charge within a unit length of the thin wire structure. Substitutes (2.5.7) into (2.5.4), we can obtain

$$\frac{\partial Q}{\partial t} + \frac{\partial I}{\partial z} = 0 \,. \tag{2.5.8}$$

Substitutes (2.5.7) into (2.5.6) yields,

$$Ez(R) = \begin{cases} L(R)\left(\dfrac{\partial I}{\partial t} + \dfrac{1}{\mu\varepsilon}\dfrac{\partial Q}{\partial z}\right), & R > r0 \\ 0, & R \le r0 \end{cases} \tag{2.5.9}$$

where $L(R) = \dfrac{\mu}{2\pi} \ln \dfrac{R}{r0}$. In FDTD domain, Ez component is an averaged quantity within its sub-cell area which has been indicated in figure 2.5 by the dotted line. While, Ez(R) component in (2.5.9) is a location dependent quantity, and it needs to be converted to an averaged value, $\langle Ez \rangle$, to satisfy the FDTD format. This is so called the in-cell inductance technique.

$$\langle Ez \rangle = \frac{\iint_S Ez(R) ds}{S} = L\left(\frac{\partial I}{\partial t} + \frac{1}{\varepsilon\mu}\frac{\partial Q}{\partial z}\right) \tag{2.5.10}$$

where $L = \dfrac{\mu}{2\pi} \dfrac{\int_{r0}^{R} \ln\left(\dfrac{\rho}{r0}\right) \rho d\rho}{\int_{0}^{R} \rho d\rho} = \dfrac{\mu}{2\pi}\left[\ln\left(\dfrac{R}{r0}\right) - \dfrac{1}{2} + \dfrac{r0^2}{2R^2}\right]$

$R = \Delta s / \sqrt{\pi}$

Note $S = \pi R^2 = \Delta s^2$ is a cell surface area. As a result, the electromagnetic field distribution outside the thin wire conductor satisfies the following equations,

$$C\frac{\partial V}{\partial t} + \frac{\partial I}{\partial z} = 0, \tag{2.5.11a}$$

$$L\frac{\partial I}{\partial t} + \frac{\partial V}{\partial z} = \langle Ez \rangle. \tag{2.5.11b}$$

where $\begin{matrix} C = \varepsilon\mu / L \\ V = Q / C \end{matrix}$.

I component in (2.5.11) is equivalent to a current source in the FDTD domain, and $\langle Ez \rangle$ is equivalent to the collocated Ez component in FDTD. The Holland thin wire model embeds thin wire structures into the FDTD domain by means of the in-cell inductance technique. The calculation procedure is illustrated in figure 2.6.

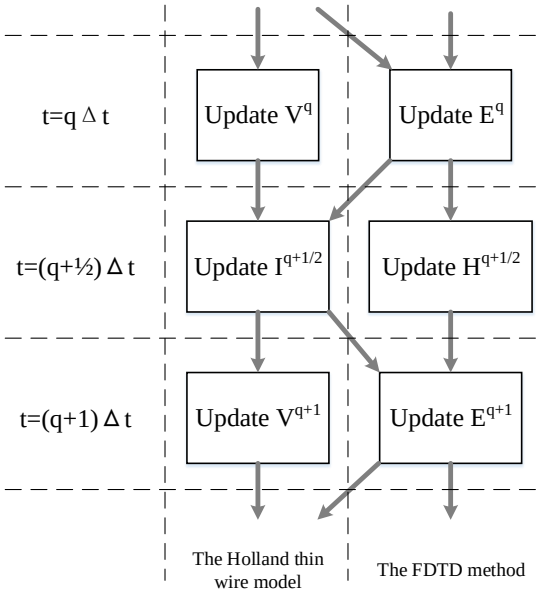

Figure 2.6 The calculation procedure for the Holland thin wire model

2.5.2 The Umashankar thin wire model

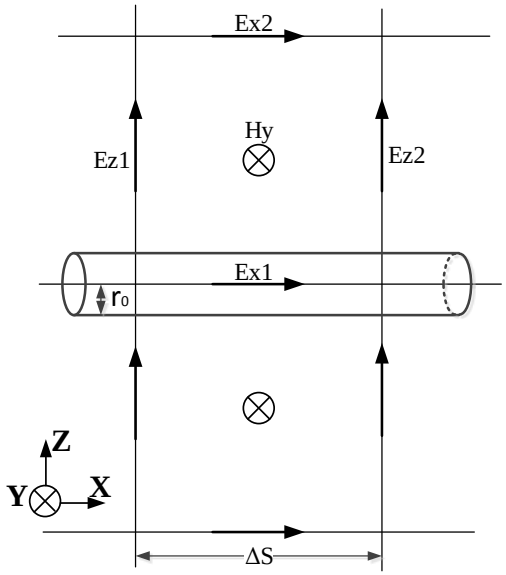

Figure 2.7 The configuration of the Umashankar thin wire model align with X axis

To derive the Umashankar thin wire model, several hypotheses are proposed first. The magnetic field nearby the thin wire is magnetostatics. The circumferential magnetic field and radial electric field around the thin wire are distributed as a function of 1/r. Finally, The thin wire is infinitely long in the longitudinal direction. The configuration of the thin wire model is shown in figure 2.7 in the Cartesian coordinate system.

The thin wire structure is located aligned with the x axis. Based on the hypotheses, the radial electric field can be expressed as

$$Ez(Z) = Ez\left(\frac{\Delta s}{2}\right)\frac{\Delta s/2}{Z}. \tag{2.5.12}$$

Similarly,

$$Hy(Z) = Hy\left(\frac{\Delta s}{2}\right)\frac{\Delta s/2}{Z}. \tag{2.5.13}$$

Taking contour integration for (2.1.2) over a Yee cell surface, we obtain

$$-\mu\iint_S \frac{\partial Hy}{\partial t}dxdz = \int_{r0}^{\Delta s} Ez1dz + \int_0^{\Delta s} Ex2dx + \int_{\Delta s}^{r0} Ez2dz + \int_{\Delta s}^{0} Ex1dx \,. \tag{2.5.14}$$

Since Ex1 is located within the thin wire structure, it can be regarded as zero if the thin wire material is a perfect electric conductor. Then, (2.5.14) can be rearranged as

$$Hy^{q+1/2} = Hy^{q-1/2} + \frac{\Delta t}{\mu}\left(Ez1^q - Ez2^q\right) + \frac{2\Delta t}{\mu \ln\left(\Delta s / r0\right)} Ex2 \,. \tag{2.5.15}$$

Other circumferential magnetic field components can be updated in the same way. According to the contour integration, the thin wire model in FDTD, which is realized by only enforcing E fields to align with the wire conductor, has an intrinsic radius. The radius is calculated as below.

$$Ez1 \cdot \frac{\Delta s}{2} \cdot \ln\frac{\Delta s}{r_{in}} = Ez1 \cdot \Delta s \quad \Rightarrow \quad r_{in} \approx 0.135\Delta s \tag{2.5.16}$$

2.5.3 The Taku Noda thin wire model

In the FDTD method, a thin wire model can be obtained directly by enforcing the E components along with the wire to zero. In this situation, the thin wire model does not modify any values of ε and μ. The corresponding radius is a natural radius, so-called intrinsic radius, r_{in}. The electric field distribution around the thin wire is assumed as proportional to be 1/r. The configuration of the Taku Noda thin wire model is shown in figure 2.8.

The intrinsic radius can be calculated as,

$$\int_{r_{in}}^{\Delta s} Ex(x)ds = A\ln\frac{\Delta s}{r_{in}} = \Delta s Ex(0.5\Delta s)$$
$$\frac{A}{1.5\Delta s} = Ex(1.5\Delta s) \qquad (2.5.17)$$

where constant A is a coefficient for describing the electric field distribution. Electric field $Ex(0.5\Delta s)$ and $Ex(1.5\Delta s)$ can be obtained from a specially designed FDTD iteration. A thin wire model is located in a volume covered by the PML absorbing boundaries. Both sides of the thin wire are truncated by absorbing boundaries to avoid unwanted reflections as shown in figure 2.9. A current source is inserted in the thin wire with enough distance from the measurement point. The source waveform is a DC wave with a smooth rise head.

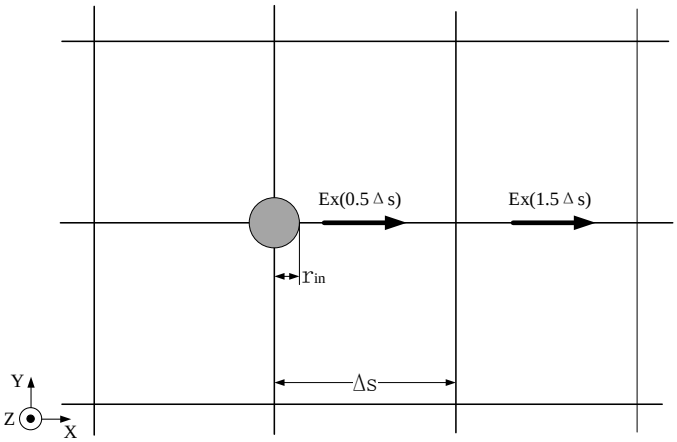

Figure 2.8 The configuration of the Taku Noda thin wire model align with z axis

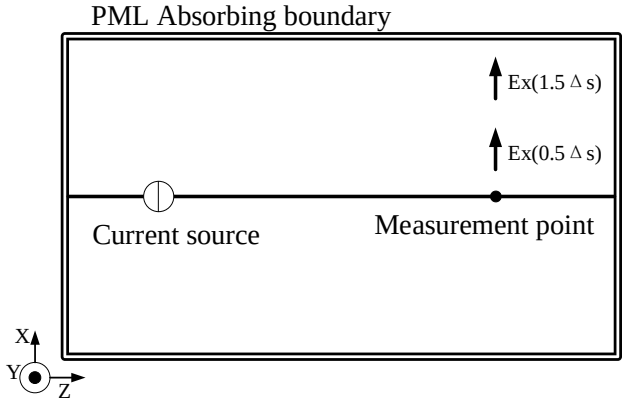

Figure 2.9 The measurement arrangement of the intrinsic radius

After the electric field at the measurement point is stable enough, the electric field $Ex(0.5\Delta s)$ and $Ex(1.5\Delta s)$ can be obtained. The relationship between r_{in} and Δs can be derived from (2.5.17) as

$$r_{in} \approx 0.2298\Delta s \,. \tag{2.5.18}$$

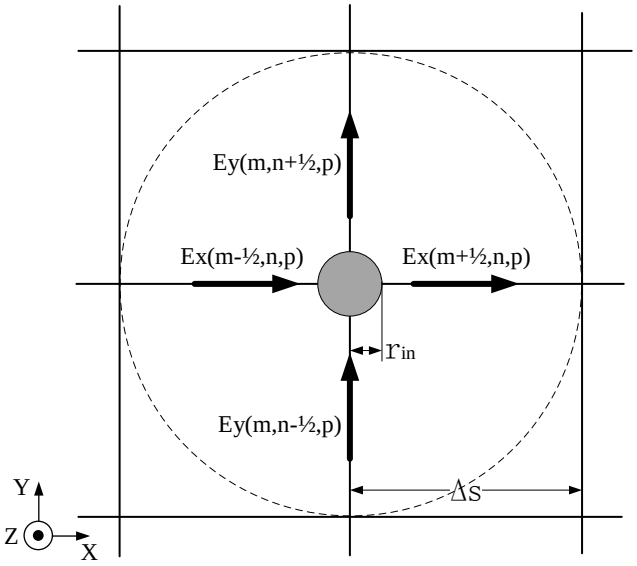

(a) 4 electric field components distribution

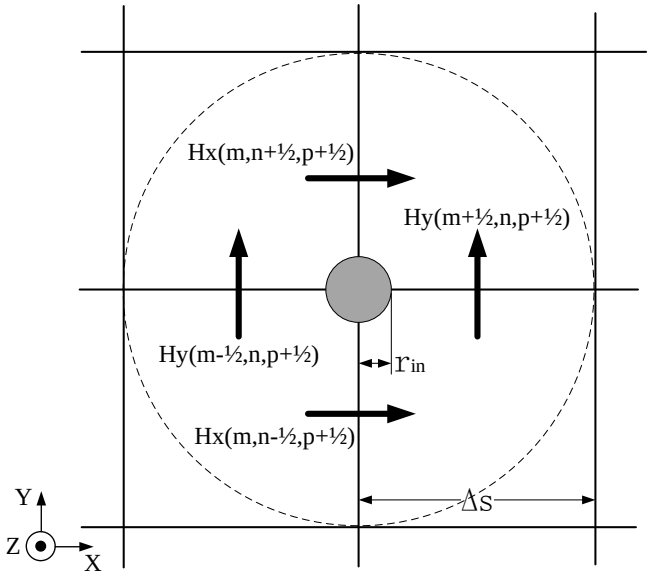

(b) 4 magnetic field components distribution

Figure 2.10 The electromagnetic field components distribution nearby the thin wire model which need to be modified

In real simulation cases, the radius will not be always equal to the intrinsic radius. A thin wire model with a desired radius can be established by modifying parameters of ε and μ which are attached to the 4 electric field components and 4 magnetic field components nearby the thin wire structure. Taking a thin wire model aligned with the Z axis as an example, the arrangement for the electromagnetic field components which needs to be modified is shown in figure 2.10. The modification is realized by

$$\begin{aligned} \varepsilon m &\Rightarrow \varepsilon^* \\ \mu / m &\Rightarrow \mu^* \end{aligned}, \tag{2.5.19}$$

where m is the correction factor.

Assuming an equipotential plane exists around the thin wire with a radius of Δ s, marked in figure 2.10 by dashed lines, the capacitance between the conductor and the equipotential plane is calculated as

$$C = \frac{2\pi\varepsilon}{\ln \Delta s / R} \tag{2.5.20}$$

where R is the desired radius of thin wire model. The capacitance should be identical for both situations: modified permittivity with intrinsic radius, unmodified permittivity with the desired radius. This equivalent equation can be represented in (2.5.21).

$$\frac{2\pi m\varepsilon}{\ln \Delta s / r_{in}} = \frac{2\pi\varepsilon}{\ln \Delta s / R} \tag{2.5.21}$$

Therefore, the correction factor can be derived from (2.5.21) as

$$m = \frac{\ln \Delta s / r_{in}}{\ln \Delta s / R} \approx \frac{1.471}{\ln \Delta s / R}. \tag{2.5.22}$$

Then the parameters nearby the thin wire model can be modified as (2.5.19) to obtain the desired radius.

The implementation of the Taku Noda thin wire model is concluded as below:

1) Confirm the radius of the thin wire model.
2) Estimate the correction factor, seeing (2.5.22).
3) Modify corresponding parameters, seeing (2.5.19).
4) Proceed FDTD iteration.

2.5.4 The Railton thin wire model

A Maxwell's equation can be regarded as containing two types of quantities: the line averaged quantity, $\langle a \rangle_x$, and the surface averaged quantity, $\langle\langle a \rangle\rangle_{xy}$. Taking Faraday's equation as an example.

$$-\mu \iint_S \frac{\partial H}{\partial t} ds = \oint_C E dl \tag{2.5.23}$$

In the X-Z plane, as shown in figure 2.11, (2.5.23) can be discretized in the vicinity of a Z-oriented thin wire model as

$$-\mu \Delta x \Delta z \frac{\partial}{\partial t} \langle\langle Hy \rangle\rangle_{xz} = \left(\langle Ez1 \rangle_z - \langle Ez2 \rangle_z \right) \Delta z + \left(\langle Ex1 \rangle_x - \langle Ex2 \rangle_x \right) \Delta x \tag{2.5.24}$$

where $\langle Exi \rangle_x$, $\langle Ezi \rangle_z$ are the averaged values along with the attached cell edges, and $\langle\langle Hy \rangle\rangle_{xz}$ is the averaged value over the corresponding cell surface. As a result, during each FDTD calculation time step, 4 line averaged quantities produce one surface averaged quantity. If the field is uniform, the derived surface quantity is

equal to the corresponding line averaged quantity. It can be then used to update another surface quantity at the next time step without any modification. For instance, in a uniform field, the line and surface quantities of Hy satisfy

$$\langle\langle Hy\rangle\rangle_{xz} = \langle Hy\rangle_{y} . \tag{2.5.25}$$

$\langle Hy\rangle_{y}$ can be used to calculate the surface averaged quantity of $\langle\langle Ex\rangle\rangle_{yz}$ and $\langle\langle Ez\rangle\rangle_{xy}$ at next time step.

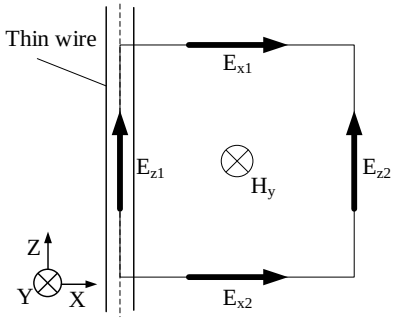

Figure 2.11 The schematic diagram for the line and surface quantities in X-Z plane

For the electromagnetic field in the vicinity of some objects, such as a thin wire structure, the line averaged quantity is not equal to the surface averaged quantity. Correction factors are needed to convert the quantities between line averaged and surface averaged. Taking Hy as an example as well,

$$\langle\langle Hy\rangle\rangle_{xz} = \mu_{y} \langle Hy\rangle_{y} . \tag{2.5.26}$$

In the static or quasi-static field, since different objects generate different field distribution, the correction factors are variant and depend on the object geometry.

For an infinite long thin wire structure, as shown in figure 2.12 which is located aligned with Z axis, the field distribution in the X and Y directions is proportional

to

$$Ex(x,y)\infty Hy(x,y)\infty \frac{x}{x^2+y^2}$$
$$Ey(x,y)\infty Hx(x,y)\infty \frac{y}{x^2+y^2} \tag{2.5.27}$$

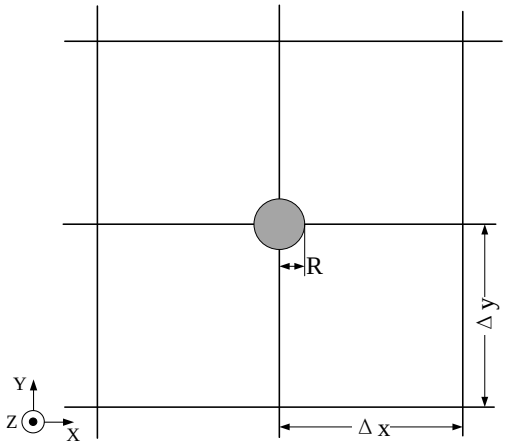

Figure 2.12 The configuration of the Railton thin wire model align with Z axis

Substituting (2.5.27) into (2.5.26), the correction factor can be derived.

$$\mu_y = \frac{\langle\langle Hy\rangle\rangle_{xz}}{\langle Hy\rangle_y} = \frac{\left(\int_R^{\Delta x} \frac{x}{x^2+y^2}dx\right)\Big/\Delta x}{\left(\int_{-\Delta y/2}^{\Delta y/2} \frac{x}{x^2+y^2}dy\right)\Big/\Delta y} = \frac{\ln\frac{\Delta x}{R}}{2\tan^{-1}\left(\Delta y/\Delta x\right)}\frac{\Delta y}{\Delta x} \tag{2.5.28}$$

The calculation of the other correction factors is similar. Then (2.5.24) can be modified as,

$$-\mu\mu_y\Delta x\Delta z\frac{\partial}{\partial t}\langle\langle Hy\rangle\rangle_{xz} = \left(\langle Ez1\rangle_z - \langle Ez2\rangle_z\right)\Delta z + \left(\langle Ex1\rangle_x - \langle Ex2\rangle_x\right)\Delta x \tag{2.5.29}$$

The Railton's method can also derive the intrinsic radius of the thin wire model which only enforces the electric field components along with the thin wire structure to zero. In this case, the line averaged quantities are equal to the surface averaged quantities around the thin wire, i.e.

$$\mu_y = \frac{\ln \frac{\Delta x}{R}}{2\tan^{-1}\left(\Delta y \big/ \Delta x\right)} \frac{\Delta y}{\Delta x} = 1 . \tag{2.5.30}$$

In a Yee structure with uniform mesh technique, the intrinsic radius can be obtained as,

$$r_{in} = 0.208\Delta x . \tag{2.5.31}$$

2.5.5 Thin wire model applications

Since the thin wire model can be constructed in a coarse FDTD mesh, the dense FDTD cell size is avoided. The computation time and memory space requirement are dramatically reduced compared with the classical FDTD discretization. Lightning surge analysis is one of the suitable application areas whose model scale is usually as large as kilometers and the radius of wire conductors is as small as centimeters, or even millimeters. Up to now, the thin wire technique has been applied successfully in the simulations of overhead line systems, tower structures, wind turbine generators, building structures, high-voltage substations, corona discharge phenomenon, buried cables and ground electrodes.

It is quite common that overhead lines, including distribution lines and shielding wires, are represented by thin wire models in the simulation. In [14], the voltage difference between the middle point of a horizontal wire and ground was investigated under indirect lightning strokes with the presence of a tall building. Different lightning parameters and configurations were discussed. To reduce the memory space requirement and simulation time in the case containing a lightning

channel, [68] proposed a two-step FDTD method. The electric field near the lightning channel is first evaluated in a 2D FDTD volume. Then the surge behaviors on transmission lines can be calculated in a 3D FDTD volume with a desirable model scale by adding a portion of EM field obtained in step one. With this proposed method, the induced current in a buried cable under a lightning stroke was evaluated [69]. The influence factors, such as lightning strike points, cable length and ground conductivity, were discussed. To restrain the induced current, a shielded cable is adopted. Its performance is evaluated. In [33], a transmission line model was established in the FDTD domain. The simulation results obtained from this model were compared with measured data under different conditions, such as lightning propagation speed, ground conductivity and length of a vertical ground rod. Reasonable accuracy was observed. [34] proposed a lightning arrester model with a nonlinear resistor element. The nonlinear V-I relation was represented by a piecewise linear curve. With the proposed model and thin wire model, a complete model of a multiphase distribution line system was established, and the simulation results match well with those obtained from the traditional method. The influences of shield wires and grounding method were discussed. In [70], the relation between the induced voltage in an overhead line system and the soil conductivity was discussed. Based on the simulation results, the construction of the vertically stratified ground does affect the induced voltage. As the depth of the top layer of the stratified ground is larger than 30m, the stratified soil can be regarded as a homogeneous soil.

The thin wire model is also adopted in the simulations of tower structures, such as grounding mesh, tower main body, current injection wires, voltage reference wires and reinforced bars. A simple vertical conductor was analyzed and discussed in [40]. Surge behaviors on the vertical conductor were simulated in case of a horizontal wave incident and a vertical wave incident. In [37, 39], a 500 kV transmission tower was modeled with the FDTD method. Ground wires were considered by the thin wire model. With this tower model, the insulator-string voltages of the tower under a lightning stroke were estimated. The effect of return stroke angles for a transmission tower was assessed in [71]. It was found the angle of current injection wire affects surge behaviors in the tower. Particularly, the surge response in case of vertical current injection wire is 30% larger than the horizontal case. Current distribution and surge behaviors within a microwave relay station tower were analyzed in an FDTD model in [72]. Reinforced bars were included in this model. Based on the simulation results, a few suggestions to design a suitable lightning protection system were proposed.

For the reasons of height and location, lightning surge analysis of wind turbine generators are necessary and important. The thin wire model is used to mimic lightning conductors in blades, grounding mesh and underground cables. Overvoltage on a reduced-size wind turbine generator under a lightning stroke was discussed in [43]. Different lighting strike points, i.e. the rear portion of nacelle and blade tip, and effect of seasons were considered. The potential rise of an

incomplete wind turbine generator and its closed area was investigated in [73]. Low grounding resistance with stratiform characteristic is considered. With the help of the FDTD method, the potential rise of a complete wind turbine under all kinds of lightning surge waveforms can be estimated. [74] discussed how the soil conductivity, relative permittivity, lightning strike position on a wind turbine and the rising head of a lightning waveform to affect the impinged surge waveforms in a buried cable.

The building structure is another application area of the thin wire model, which is used to represent reinforced bars, electrical wirings and metallic pipelines. In [75], current distribution and oscillation phenomenon within reinforced concrete structures were estimated and discussed. The contribution of a closed ring conductor to restrain oscillation was investigated. [44] investigated induced voltage and invaded current within a building structure under a direct lightning stroke. The influence factors, such as building height, wiring method and lightning waveforms were analyzed separately. Based on the simulation results, the location of the SPD installation and its rating selection were suggested. A model of a full-scale building including reinforced concrete and reinforced bars were established with the FDTD method in [76]. A lightning protection system, grounding mesh and nonlinear lumped components were also included. The EM environment inside the building structure was evaluated under direct and indirect lightning strokes. A transmission line system with lightning arresters and pole transformers, as well as

buildings, were modeled with the FDTD method in [77, 78]. The induced voltage surges in the transmission line system under lightning strokes were analyzed. It was observed that with the presence of buildings, the induced voltage surges are reduced.

The thin wire model can be used in simulations of high-voltage substations. [29] evaluated EM transients in a high-voltage substation when a circuit breaker was switched. A few factors which may influence the EM environment were analyzed, such as relative position, signal spectrum and ground condition. An air-insulated high-voltage substation was modeled with the FDTD method with considering nonlinear circuit breakers, lightning arresters and back-flashover phenomena in [79]. The current invaded in the substation under lightning strokes were analyzed. Some protection suggestions and techniques to protect the low-voltage control circuit in the substation were proposed.

Corona phenomenon in power systems and grounding electrodes can also be simulated with the thin wire model. [35, 80, 81] proposed an advanced thin wire model which can consider the corona discharge. The equivalent radius and conductivity of the area is controlled and adjusted by the instantaneous electric field near the wire. The calculated results match well with the measured waveforms. With the help of the proposed corona model, the transient voltages on an insulator were estimated in a transmission line system in [36]. The corona discharge on the ground wire will reduce the voltage amplitude. The behaviors of

soil ionization close to earth electrodes (represented by the thin wire model) were investigated with the FDTD method in [82]. The value of soil resistivity is variant, and it depends on the local electric field strength.

3 Thin wire model of lossy round wire structures

In this chapter, an extended thin wire model is presented to model lossy round wire structures, and to solve transient problems even if the skin effect is significant. This model is an extension of the traditional model proposed by Railton [52]. First differential equations [83, 84] are established in the conductor zone. An equivalent circuit is then built to determine current density in the conductor, subsequently electric field on the conductor surface. The results are finally integrated into the FDTD equations [52] to update E/H field components around the wire structure. In this chapter, the thin wire model for solid lossy wires is presented first, followed by hollow cylindrical tubes and coaxial conductors. In a coaxial cable, the surge propagation over a lossy transmission line is taken into account. Finally analytical and numerical validation of the extended thin-wire model is presented.

3.1 Extended model for a solid wire/hollow tube

Consider a case in which a long lossy conductor is immersed in the medium with permittivity ε and permeability μ_0. The conductor is a cylinder with radius r_a or a cylindrical tube with outer and inner radii of r_a and r_b. It is characterized with conductivity σ and permeability μ. Fig. 3.1 shows the configuration of a single conductor placed in the FDTD grid. Without loss of generality, this conductor is orientated along the x axis.

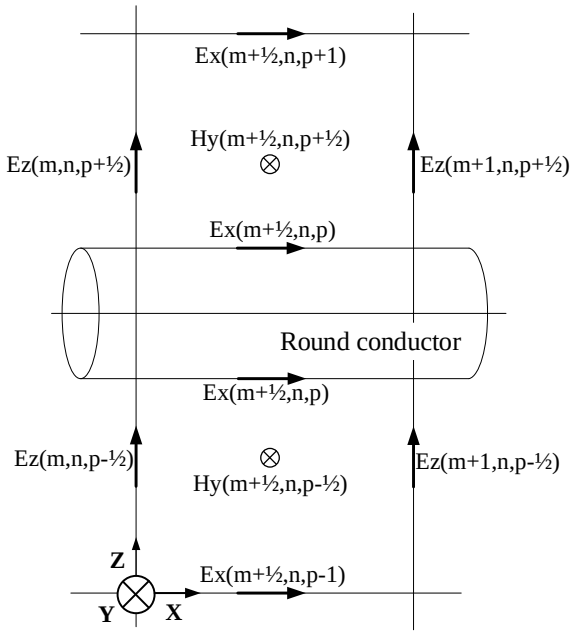

(a) x-z plan view

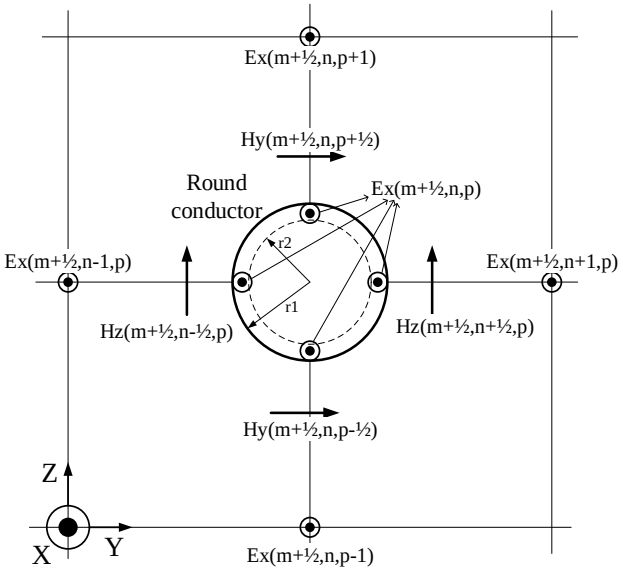

(b) y-z plan view

Figure 3.1 Configuration of a single round conductor in the working domain (m, n and p denote cell indices in x, y, and z directions, and q time step index)

The whole working volume is divided into two regions: conductor region and non-conductor region (or FDTD region). In the FDTD region, electric (E) /

magnetic (H) field components adjacent to the conductor are updated with "corrected" FDTD equations given in [52]. In these equations, the permittivity and permeability of the medium are corrected by multiplying correction coefficient m. In a uniform meshing system, this coefficient is given by

$$m = \pi / \left[2\ln\left(r_a / s \right) \right] \tag{3.1}$$

where s is the width of cells in the FDTD region.

Note that the electric field on the surface of a lossy conductor is not equal to zero. A separate set of equations need to be established in order to determine electric field component E_x in the axial direction. Assume conductor current is constant along its axis in a cell. A 2D differential equation for current density $J(r,t)$ inside the conductor is then obtained [83], as follows:

$$\frac{\partial J(t)}{\partial r} = \frac{\mu\sigma}{2\pi r}\frac{\partial I(t)}{\partial t}, \tag{3.2}$$

where $I(r,t)$ is the total current within the cylindrical zone of radius r.

Divide the round conductor into a set of thin cylindrical shells ($i = 1,2 \ldots M$) over its cross section from its outer surface to the center, as seen in Fig. 3. 2. Shell i has outer radius r_i and inner radius r_{i+1}, and cross sectional area A_i. Discretize (3.2) in both time and space. Assume that I_i^q is the total current in a cylindrical zone containing all inner shells (shell $i, i+1 \ldots M$) at time step q. A discrete form of (3.2) is then obtained, as follows:

$$R_{i-1}[I_{i-1}^q - I_i^q] - R_i[I_i^q - I_{i+1}^q] = L_i \frac{I_i^q - I_i^{q-1}}{\Delta t} \tag{3.3}$$

where equivalent resistance $R_i = 1/A_i\sigma$ and inductance $L_i = \mu(r_{i-1} - r_i)/2\pi r_i$

for cylindrical shell i $(i = 1 \cdots M)$. Δt is the size of the time step.

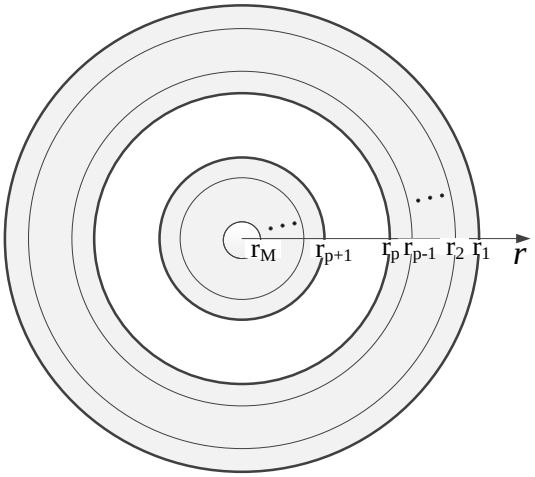

(a) Meshing of a cylindrical conductor

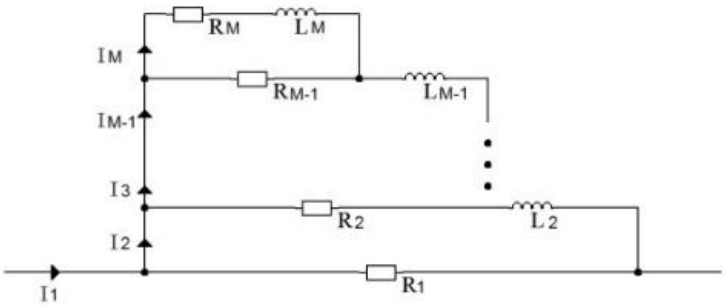

(b) Equivalent circuit for cylindrical zone currents

Figure 3.2 Model of a cylindrical conductor

Applying the implicit backward Euler's integration method (3.3) yields an updating equation of zone currents, as follows:

$$I_i^q = a_{i,i-1} \cdot I_{i-1}^q + \sum_{j=i}^{M} a_{i,j} I_j^{q-1} , \tag{3.4}$$

where

$$a_{i,i} = 1/[1 + [R_{i-1} + (1 - a_{i+1,i}) R_i] \Delta t / L_i] ,$$

$$a_{i,i-1} = a_{i,i} \cdot R_{i-1} \cdot \Delta t / L_i ,$$

$a_{i,j} = a_{i,i} \cdot a_{i+1,j} \cdot R_i \cdot \Delta t / L_i$.

and $a_{M+1,M}$ is equal to zero. Fig. 3.2 (b) presents an equivalent circuit for cylindrical zone currents using equivalent resistance and inductance. The shell number in a conductor zone is determined by its skin depth at the primary frequency so that the current density does not vary significantly in each shell. For example, the thickness of the outermost shell is smaller than 1/10 of the skin depth.

Note that total conductor current $I_1^q(m+1/2)$ in segment $m+1/2$ and time step q is derived by integrating H vectors in a contour path enclosing the conductor, as follows:

$$I_1^q(m+1/2) = \Delta z \cdot \begin{bmatrix} H_z^q(m+1/2, n+1/2, p) \\ -H_z^q(m+1/2, n-1/2, p) \end{bmatrix} + \Delta y \cdot \begin{bmatrix} H_y^q(m+1/2, n, p-1/2) \\ -H_y^q(m+1/2, n, p+1/2) \end{bmatrix}. \tag{3.5}$$

where Δy and Δz are the cell dimensions in the y and z directions. With (3.4) cylindrical zone current $I_i^q \quad (i = 2 \ldots M)$ in the interior zones can be determined by total conductor current I_1^q at the present time step, and cylindrical zone currents $I_{i-1}^{q-1} \quad (i = 2 \ldots M)$ at the previous time step. The axial field component E_x on the conductor surface is then obtained by using the surface current, as follows:

$$Ex_{m+1/2,n,p}^{q+1/2} \approx \frac{I_1^q(m+1/2) - I_2^q(m+1/2)}{A_1 \cdot \sigma} \tag{3.6}$$

This field component is used in the "corrected" FDTD equations for updating H field components adjacent to the conductor. The FDTD updating cycle is then

completed.

The hollow cylindrical tube actually is a special case of the solid conductor. Consider that a conductor is divided into M shells. The last shell has zero inner radius if it is a solid conductor, and has a non-zero inner radius if it is a hollow tube. The FDTD updating equations for the field components adjacent to the conductor remain unchanged.

3.2 Extended model for a coaxial structure

3.2.1 Coaxial conductors with a non-zero transverse voltage

Shown in Fig. 3.3 is a configuration of two coaxial conductors. There are three sub-regions in this case; (a) outer conductor, (b) inner conductor, and (c) air gap or insulation layer between two conductors. As the exterior of the outer conductor remains unchanged, the FDTD updating equations in local cells and E_x calculation given in Section 2 are still valid.

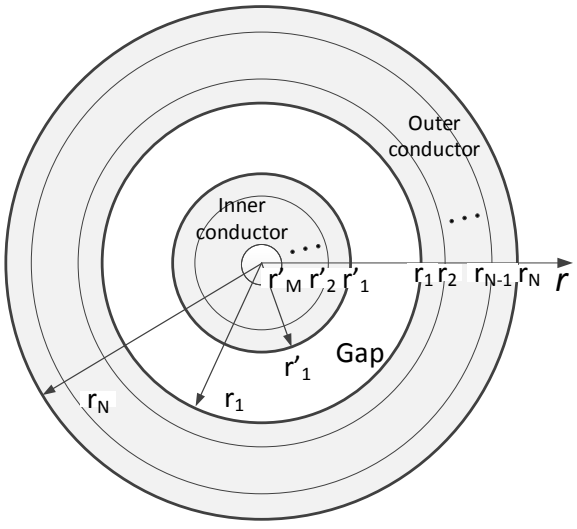

Figure 3.3 Configuration of coaxial conductors

To determine the current density on the conductors, cross section discretization is made for both outer and inner conductors. In this case a special shell ordering strategy is adopted to simplify the system equations. On the inner conductor the outermost shell is the first one, while the innermost shell is the first one on the outer conductor, as shown in Fig. 3.3. Discretizing (3.2) in both conductors and applying the backward Euler's integration method yield a set of discrete equations for updating cylindrical zone currents, as follows:

$$\begin{aligned} I_{in,i}^{q} &= a_{i,i-1}^{in} \cdot I_{in,i-1}^{q} + \sum_{j=i}^{M} a_{i,j}^{in} I_{in,j}^{q-1} \\ I_{ou,i}^{q} &= a_{i,i-1}^{ou} \cdot I_{ou \cdot i-1}^{q} + a_{i,N}^{ou} \cdot I_{ou,N}^{q} + \sum_{j=i}^{N-1} a_{i,j}^{ou} I_{ou,j}^{q-1} \end{aligned}, \tag{3.7}$$

where $I_{in,i}^{q}$ and $I_{ou,i}^{q}$ are respectively the currents in the cylindrical zones with radius r_i' (inner conductor) and radius r_i (outer conductor). Both $a_{i,j}^{in}$ and $a_{i,j}^{ou}$ in (3.8) are respectively the coefficients for inner shells and outer shells, and are given in (3.4). Especially, $a_{N,N}^{ou}$ is identical to 1 and inductance $L_i = \mu(r_i - r_{i-1})/2\pi r_i$ for shells in the outer conductor. Let I_{in}^{q} and I_{ou}^{q} be the total conductor currents in inner and outer conductors, respectively. With the definition of cylindrical zone current, the following equations hold

$$\begin{aligned} I_{in,1}^{q} &= I_{ou,1}^{q} = I_{in}^{q} \\ I_{in}^{q} + I_{ou}^{q} &= I_{ou,N}^{q} \end{aligned}, \tag{3.8}$$

where $I_{ou,N}^{q}$ is considered to be the total wire-structure current, which is not necessarily equal to zero.

Transmission line equations in the gap have to be established to link currents in

both inner and outer conductors. Let L and C be the per-unit length inductance and capacitance of a lossless coaxial cable, which are given by

$$\begin{aligned} L &= \frac{\mu}{2\pi}\ln\frac{r_1}{r_1'} \\ C &= \frac{2\pi\varepsilon}{\ln r_1/r_1'} \end{aligned}. \tag{3.9}$$

The lossy transmission line equations are now expressed by

$$\begin{aligned} \frac{\partial V^{q-1/2}(m+1/2)}{\partial x} &= -L\frac{\partial I_{in}^{q-1/2}(m+1/2)}{\partial t} - V_{R.in}^{q-1/2} + V_{R.ou}^{q-1/2} \\ \frac{\partial I_{in}^{q}(m)}{\partial x} &= -C\frac{\partial V^{q}(m)}{\partial t} \end{aligned}, \tag{3.10}$$

where $V^{q-1/2}$ is the transverse voltage between inner and outer conductors. Both $V_{R.in}^{q-1/2}$ and $V_{R.ou}^{q-1/2}$ are determined by axial electric field components on the conductor surfaces in the gap. They are expressed by

$$V_{R.in}^{q-1/2} = R_{in.1}\left(I_{in.1}^{q-1/2}(m+1/2) - I_{in.2}^{q-1/2}(m+1/2)\right)$$

$$V_{R.ou}^{q-1/2} = R_{ou.1}\left(I_{ou.2}^{q-1/2}(m+1/2) - I_{ou.1}^{q-1/2}(m+1/2)\right)$$

Note that $I^{q-1/2} \approx 0.5(I^{q-1} + I^{q})$. Both $I_{in,2}^{q}$ and $I_{ou,2}^{q}$ in (10) can be expressed by $I_{in,1}^{q}$ and $I_{ou,1}^{q}$ and $I_{ou,N}^{q}$ with (3.7). Note that the outer conductor current does not contribute any inductive voltage drop in evaluating transverse voltage on the coaxial structure.

Fig. 3.4 shows the circuit model of the lossy transmission line of a lossy coaxial structure. Both inner and outer conductors are represented by equivalent cascade circuits developed from (3.7), which are similar to that shown in Fig. 3.2(b). Both $R_{j,i}$ and $L_{j,i}$ $(j = in, ou)$ are the equivalent resistance and inductance of shell i

in the inner or outer conductor, and are determined by (3.3).

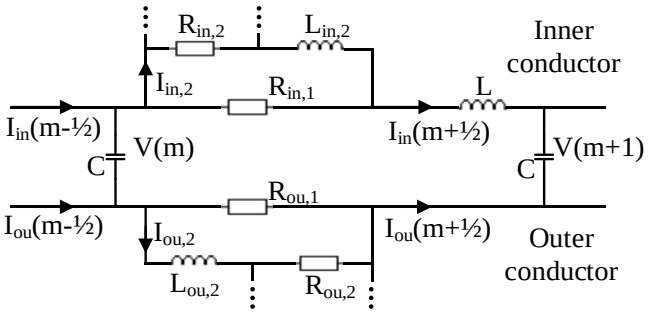

Figure 3.4 Transmission line configuration of a coaxial wire structure

Total wire-structure current $I_{ou,N}^{q}$ is determined from an integral of magnetic field along a contour path enclosing the coaxial structure. Note from (3.8) that $I_{in,1}^{q} = I_{ou,1}^{q} = I_{in}^{q}$. Three unknowns I_{in}^{q}, I_{ou}^{q} and $V^{q+1/2}$ can be completely determined with (3.10), and are expressed explicitly by

$$\begin{aligned} I_{in}^{q}(m+1/2) &= \left[P^{q} - T \cdot I_{ou,N}^{q}(m+1/2)\right] \Big/ S \\ I_{ou}^{q}(m+1/2) &= I_{ou,N}^{q}(m+1/2) - I_{in}^{q}\left(m+1/2\right) \\ V^{q+1/2}(m) &= V^{q-1/2}(m) + F\left[I_{in}^{q}(m+1/2) - I_{in}^{q}(m-1/2)\right] \end{aligned} \quad , \tag{3.11}$$

where

$$F = -\frac{\Delta t}{C \cdot \Delta x}$$

$$S = \frac{L}{\Delta t} + \frac{R_{in.1}}{2}(1 - a_{2,1}^{in}) - \frac{R_{ou.1}}{2}(a_{2,1}^{ou} - 1)$$

$$T = \frac{R_{ou.1}}{2} a_{2,N}^{ou}$$

$$\begin{aligned} P^{q} = &-\frac{V^{q-1/2}(m+1) - V^{q-1/2}(m)}{\Delta x} + \frac{L}{\Delta t} I_{in}^{q-1}(m+\frac{1}{2}) \\ &-\frac{R_{in,1}}{2}\begin{bmatrix} I_{in,1}^{q-1}(m+1/2) \\ -I_{in,2}^{q-1}(m+1/2) \end{bmatrix} + \frac{R_{ou,1}}{2}\begin{bmatrix} I_{ou,2}^{q-1}(m+1/2) \\ -I_{ou,1}^{q-1}(m+1/2) \end{bmatrix} \\ &+\frac{R_{in,1}}{2}\sum_{j=2}^{M} a_{2,j}^{in} I_{in,j}^{q-1}(m+1/2) + \frac{R_{ou,1}}{2}\sum_{j=2}^{N-1} a_{2,j}^{ou} I_{ou,j}^{q-1}(m+1/2) \end{aligned} \quad .$$

Subsequently, $I_{ou,2}^{q}$ is determined with (3.7) using $I_{ou,1}^{q}$ and $I_{ou,N}^{q}$. The axial

field component E_x on the surface of the outer conductor can be then calculated with the equation similar to (3.6).

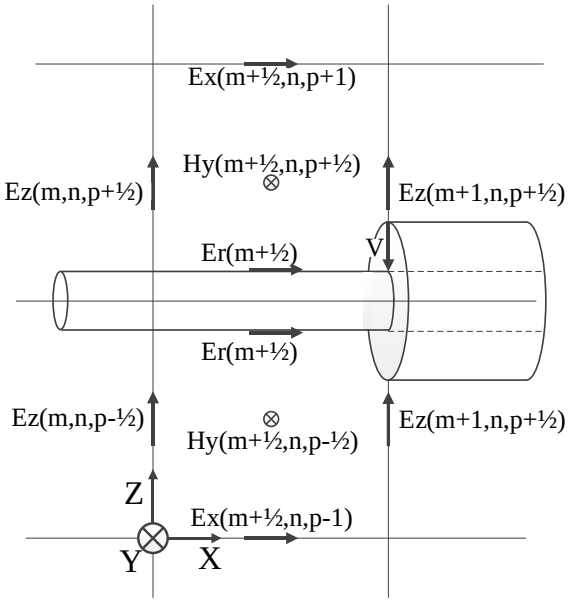

Figure 3.5 Configuration of the end of a coaxial wire structure

3.2.2 End of the coaxial structure

Without loss of generality, the inner conductor is connected to a feeding line. Non-zero transverse voltage V may be observed at the end of the wire structure, as shown in Fig. 3.5. The extended model presented in Section 2 is applicable to the conductor at its end. However, transverse voltage V needs to be inserted in the FDTD equations for updating transverse H field components. Magnetic field component H_y, for example, is calculated with both electric field components and transverse voltage, as follows:

$$H_y^{q+1}(m+1/2,n,p+1/2) = H_y^{q}(m+1/2,n,p+1/2) - \frac{\Delta t}{\mu \Delta z} \cdot \begin{bmatrix} E_x^{q+1/2}(m+1/2,n,p+1) \\ -E_x^{q+1/2}(m+1/2,n,p) \end{bmatrix} + \frac{\Delta t}{\mu \Delta x} \begin{bmatrix} E_z^{q+1/2}(m,n,p+1/2) - \\ E_z^{q+1/2}(m+1,n,p+1/2) \end{bmatrix} - \frac{\Delta t}{\mu \Delta x \Delta z} V^{q+1/2} \tag{3.12}$$

Eq. (3.12) is also applicable to the case in which the coaxial structure is open at its end. When both inner and outer conductors are bonded together at the structure end, transverse voltage V is simply set to zero.

The complete computation procedure for the coaxial structure is summarized in Fig. 3.6.

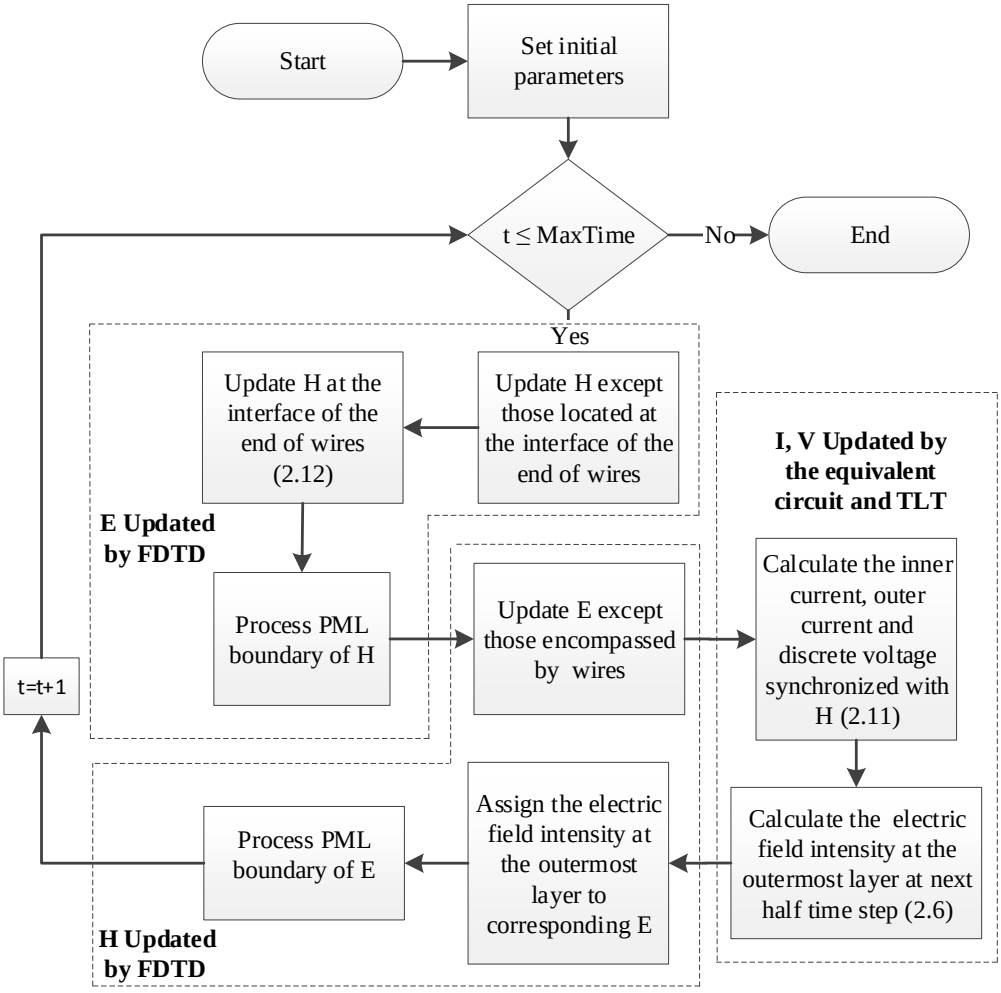

Figure 3.6 Flow chart of the FDTD procedure for coaxial wire structures

3.2.3 Coaxial structure with zero transverse voltage

If both inner and outer conductors of a coaxial structure are electrically

connected at two ends, the potential difference between them or transverse voltage is zero everywhere along the coaxial structure. There is no radial displacement current in the air gap or insulation layer. This can be considered as a special case of the solid conductor, in which one of shells has zero conductivity. Without loss of generality, let cylindrical shell *p* be the gap, as shown in Fig. 3.2(a).

By using the same procedure presented in the previous section, discrete equations for cylindrical zone currents in inner and outer conductors are obtained, as follows:

$$I_i^q = a_{i,i-1} \cdot I_{i-1}^q + \sum_{j=i}^{p} a_{i,j} I_j^{q-1} + \sum_{k=p+2}^{M} a_{i,k} I_k^{q-1} \tag{3.13a}$$

for $p \le i \le M$, where coefficient $a_{i,j}$ is determined by with (3.2), and

$$I_p^q = a_{p,p-1} \cdot I_{p-1}^q + a_{p,p} \cdot I_p^{q-1} + \sum_{j=p+2}^{M} a_{i,j} I_j^{q-1} \tag{3.13b}$$

for $i < p$, where

$$a_{p,p} = \frac{1}{1+[R_{p-1} + (1-a_{p+2,p+1})R_{p+1}]\Delta t/(L_p + L_{p+1})},$$

$$a_{p,p-1} = a_{p,p} R_{p-1} \cdot \Delta t/(L_p + L_{p+1}),$$

$$a_{p,j} = a_{p,p} \cdot a_{p+2,j} \cdot R_{p+1} \cdot \Delta t/(L_p + L_{p+1}).$$

The inductance in the gap is modified to be

$$L_p = \frac{\mu}{2\pi} \ln \frac{r_p}{r_{p+1}}. \tag{3.14}$$

Note that both cylindrical zone currents I_p^q and I_{p+1}^q adjacent to the gap are the same.

Similar to the solid wire, the total current is obtained by integrating magnetic field components in the FDTD domain at each time step. Current distribution in

the conductors is updated with (3.13), subsequently the electric field component on the conductor surface. The FDTD updating cycle is then completed.

3.3 Numerical evaluation and validation

The extended thin-wire model has been applied to study wave or surge propagation on lossy wire structures. For validation, the results were compared with an analytical formula for simple wire structures, and numerically with the commercial FDTD software for a coaxial structure.

3.3.1 Analytical validation

A lossy wire structure running in parallel with the perfect ground is selected for validating the proposed thin-wire model analytically. Fig. 3.7(a) shows the configuration of Testing System A. In this system, the line is assumed to be infinitely long without any reflection, and is situated at the height of $0.19\,\mathrm{m}$ above the perfect ground. The line is connected to a voltage source at one end via a lossless wire. The voltage source generates a sinusoidal waveform of $100\,\mathrm{MHz}$. Several wire structures are tested, including a solid round conductor, a hollow cylindrical tube, and a coaxial cable with zero transverse voltage. Table 3.1 shows the geometric dimensions of these wire structures. The conductivity of all wires is set to $1 \times 10^6\,\mathrm{S/m}$, and the skin depth of the wires is equal to $0.05\,\mathrm{mm}$. Attenuation of the sinusoidal wave propagating along this lossy transmission line is investigated.

On a lossy round wire, no matter whether it is a solid wire, a hollow wire or a shorted coaxial cable, propagation of a sinusoidal wave with frequency ω can be analyzed using the transmission line theory [85]. By assuming no reflected wave and lossless dielectric material, voltage $V(x,t)$ on the line is described by

$$V(x,t) = V_0 e^{-bx} \sin(\omega t - \gamma x). \tag{3.15}$$

where V_0 is the voltage amplitude at the origin. At high frequency, i.e. $\omega L \gg R$, attenuation constant b and the wave propagation constant γ in (3.15) is determined by

$$\begin{aligned} b &= \frac{R}{2} \cdot \sqrt{\frac{C}{L}}, \\ \gamma &= \omega\sqrt{LC} \end{aligned} \tag{3.16}$$

where C and L are the capacitance and inductance of a traditional transmission line. Resistance R is frequency-dependent, and can be determined using the formulas for the internal impedance of round wires [86].

Table 3.1 Geometric dimensions of wire structures

Wire structures	Inner radius (mm)	Outer radius (mm)	Thickness (mm)
Solid conductor	0	3	3
Cylindrical tube	0	3	0.02
Coaxial cable*	1	3	0.02

Note: * both inner and outer conductors are connected electrically at two ends

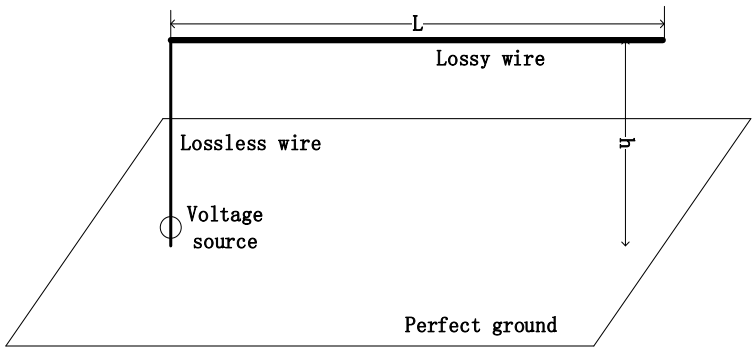

(a) Testing System A

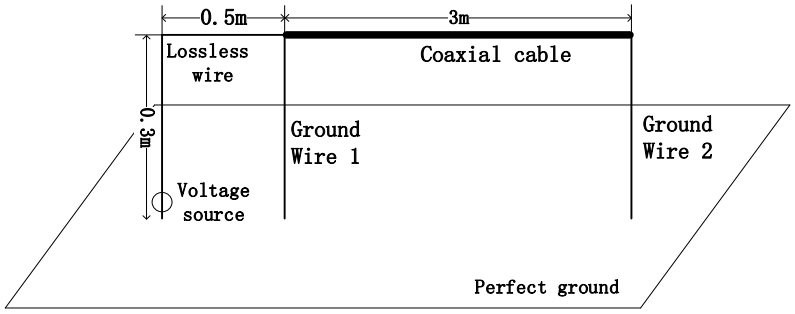

(b) Testing System B

Figure 3.7 Configuration of two testing systems

In the FDTD simulation with the proposed model, the whole working volume of the simulation model is $0.5\ \text{m} \times 0.5\ \text{m} \times 40.5\ \text{m}$. It is surrounded by perfectly matched layers to absorb unwanted reflection. The free space buffers between the conductor and absorbing boundaries have at least 25 cells. A uniform meshing scheme is adopted, and the cell size is set to $10\ \text{mm}$. In the conductor region, a non-uniform discretizing scheme [83] is adopted in the solid wire and inner conductor of the coaxial cables with 40 shells; a uniform discretizing scheme is adopted in the hollow tube and outer conductor of the cable with 20 shells.

The amplitude of the sinusoidal voltage at $x = 5\ \text{m}$ was set to $1\ \text{kV}$. Voltages on

the line at several locations ($x = 15$ m, 25 m and 35 m) are calculated. The results obtained with both the proposed FDTD model and analytical formula (3.15) are given in Table 3.2. In the table, V_{SE} denotes the voltage calculated by the extended thin wire model, and V_{TL} by the transmission line formulas. It is noted that the results obtained with the proposed FDTD model match theoretical values very well with a maximum relative error of 0.29% and an average relative error of 0.11%. This indicates that the extended thin wire model is applicable to lossy solid wires, hollow tubes and coaxial cables with core and sheath being connected.

Table 3.2 Wave attenuation taking into account the skin effect over a solid round wire, a hollow tube and a shorted coaxial cable

Locations/m		5	15	25	35
Solid conductor	V_{SE}/V	1000	983.3	966.9	949.8
	V_{TL} /V	1000	982.0	964.3	947.0
Hollow tube	V_{SE}/V	1000	956.2	914.4	873.4
	V_{TL} /V	1000	955.3	912.6	871.8
Paralleled coaxial cable	V_{SE}/V	1000	956.4	914.6	873.9
	V_{TL} /V	1000	955.5	913.0	872.4

3.3.2 Numerical validation

There is no analytical formula available for a coaxial wire structure if it carries an unbalanced current. The traditional FDTD method is then selected for the comparison with the proposed thin-wire model. The mesh size of the coaxial cable

must be less than its skin effect depth if the traditional FDTD method is used. Extremely large memory space and extremely long calculation time would be required. To make the comparison feasible, a 3 m-long coaxial cable is selected for testing.

Fig. 3.7(b) shows the configuration of a testing system for the coaxial cable. The lossy coaxial cable runs in parallel with the perfect ground. The cable has the same dimensions as those given in Table 3.1, except for sheath thickness. The sheath thickness is now increased to $1\ \text{mm}$ in order to avoid unacceptable memory allocation in the simulation by the traditional FDTD method. The inner conductor is connected to a voltage source via a lossless wire. While the outer conductor is grounded at its two ends with two lossless wires. The voltage source is grounded at the other end, and generates a voltage with the Gaussian impulse waveform of $5\ \text{ns}$ pulse width. The currents of both inner and outer conductors at $x = 0.5\ \text{m}$ are recorded for comparison.

The working volume of the proposed model is $0.5\ \text{m} \times 0.5\ \text{m} \times 4\ \text{m}$. In the simulation using the extended thin-wire model, the cell size in the non-conductor (FDTD) region is set to 10 mm uniformly. In the conductor region, the inner conductor is divided into 40 shells with the non-uniform discretizing scheme, and the outer conductor is divided equally into 50 shells. In the traditional FDTD simulation, a non-uniform meshing technique is adopted. The cell size in the *y* and *z* directions is $0.03\ \text{mm}$ on the conductors, and is increased gradually to $0.5\ \text{m}$.

The meshing scheme for the coaxial cable in the *y*-*z* plane is illustrated in Fig. 3.8. In both cases, perfectly matched layers are adopted on the boundary of the working volume to absorb unwanted reflection.

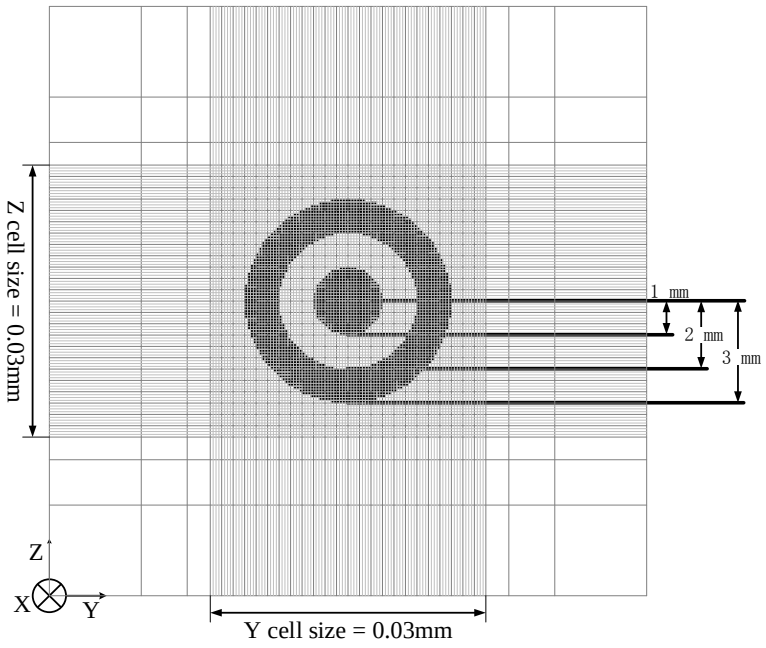

Figure 3.8 The meshing scheme for the coaxial cable in the traditional FDTD simulation

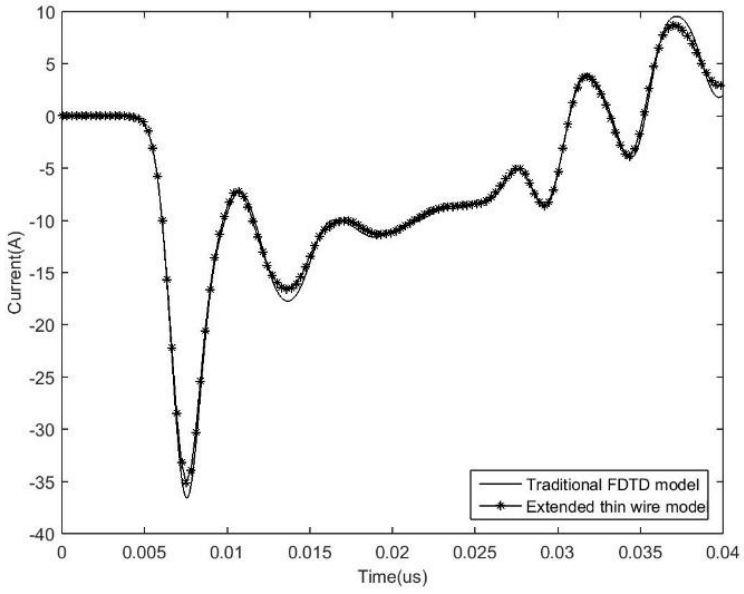

Figure 3.9 Current waveforms in the inner conductor

Fig. 3.9 and Fig. 3.10 show the simulated current waveforms obtained with these two methods. It is found that these results match well in general. A small difference of the currents is observed around their peaks. The maximum relative difference of current is around 4% to 5% in both inner and outer conductors. Note that in this case the currents of both inner and outer conductors are not the same. Compared with the traditional FDTD method, the extended thin wire model takes much less computational resources. In this case, the simulation with the traditional method consumed 4 GB memory space and ran 655 hours in a single core CPU (Inter® Core™ i7-4790 CPU @ 3.60 GHz). While the simulation with the proposed model consumed less than 0.5 GB memory space and ran 5 hours only.

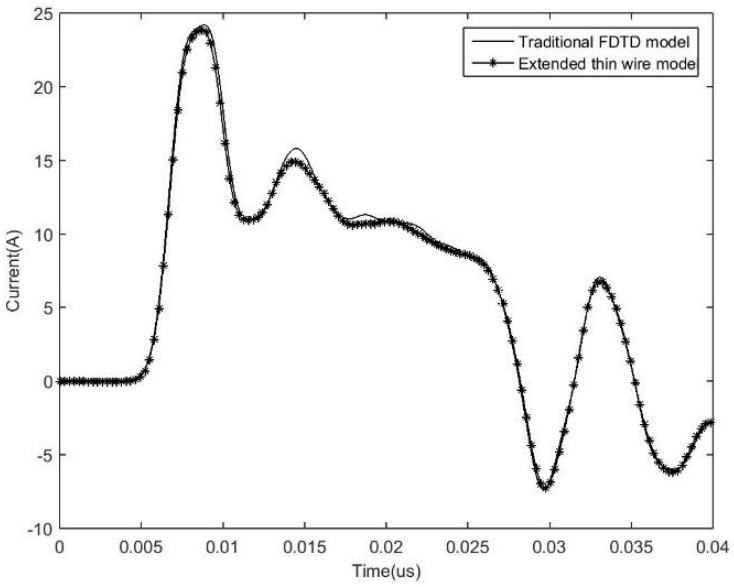

Figure 3.10 Current waveforms in the outer conductor

A further investigation is performed to find out the reason for the 4%-5% difference. In this case, surge propagation on a lossless coaxial cable with the same

geometry is simulated with these two methods. The surge impedance is then determined by using the measured voltage and current at $x = 0.5$ m. The results are compared with the theoretical formula $z = \sqrt{L/C}$. Table 3.3 shows these calculated values of surge impedance of the lossless line. It is found that the value with the proposed model is almost the same as the theoretical value, with the difference of less than 1%. While the difference with the traditional method reaches 5% approximately. Therefore, it is reasonable to conclude that the difference of currents in Fig. 3.9 and Fig. 3.10 is primarily due to the meshing scheme adopted in the transitional FDTD method. In order to obtain more accurate results, much finer meshing is required in the traditional method. This will, however, lead to unacceptable computation resources required.

Table 3.3 Comparison of lossless-line surge impedance

Method	Traditional FDTD method	Proposed thin-wire model	Transmission line theory
Impedance (Ω)	364.03	380.23	383.82

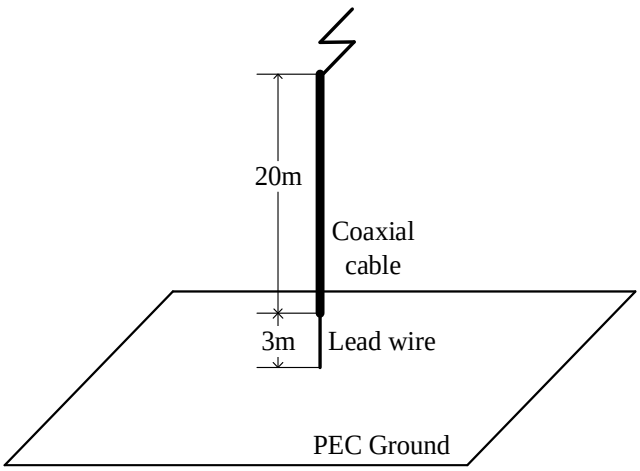

Figure 3.11 Configuration of a coaxial cable subject to a lightning stroke

3.3.3 Surge current sharing in a coaxial cable

This proposed thin-wire model is now applied to analyze current sharing in a lossy RF coaxial cable. Fig. 3.11 shows the configuration of a coaxial cable subject to a lightning stroke. As shown in Fig. 3.11, this 20 m-long outdoor cable runs vertically, and the outer conductor at the bottom end is connected to the perfect ground via a $3\,\mathrm{m}$ lossless lead wire. Both inner and outer conductors are connected together directly at the top end, and via a MOV device at the bottom end. The RF cable has the radii of $12.65\,\mathrm{mm}$ and $4.5\,\mathrm{mm}$ for outer and inner conductors, respectively, and the conductor thickness of $0.2\,\mathrm{mm}$. The conductivity of the lossy cable is $5.96 \times 10^7\ \mathrm{S/m}$.

In the simulation the lightning return stroke is represented by a current source connected at the top with an upward lead wire. It generates an impulse current of $0.25/100\ \mu\mathrm{s}$ with $10\,\mathrm{kA}$ amplitude. The working volume of the simulation model is $6\ \mathrm{m} \times 6\ \mathrm{m} \times 29\ \mathrm{m}$. The upward lead wire reaches the PML boundary on the upper end. The uniform meshing scheme is adopted in the non-conductor (FDTD) region, and the cell size is set to $0.1\ \mathrm{m}$. The technique proposed in [51] is applied to enhance numerical stability. The coaxial cable is represented with the extended thin-wire model proposed in this chapter. In the conductor region, the shell numbers of both inner and outer conductors are 40 and 20 respectively. The nonlinear MOV device is modelled with a piece-wise linear resistance [34].

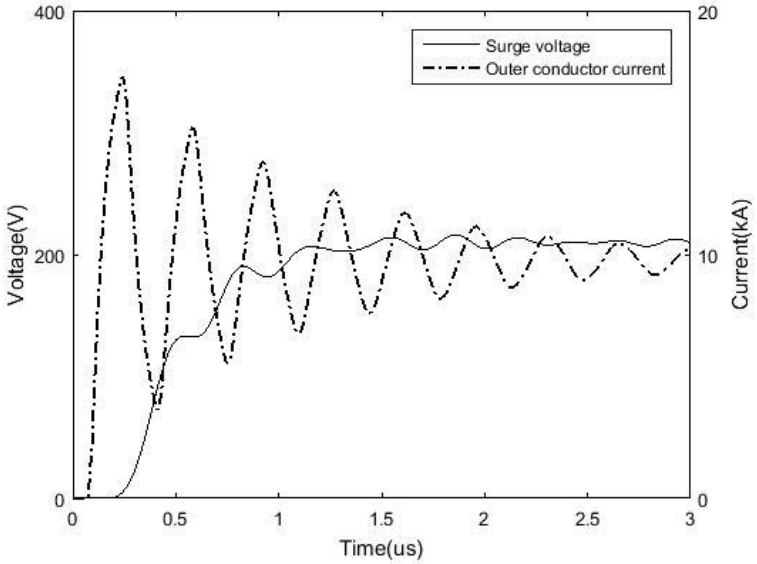

(a) Without a MOV device at the bottom end

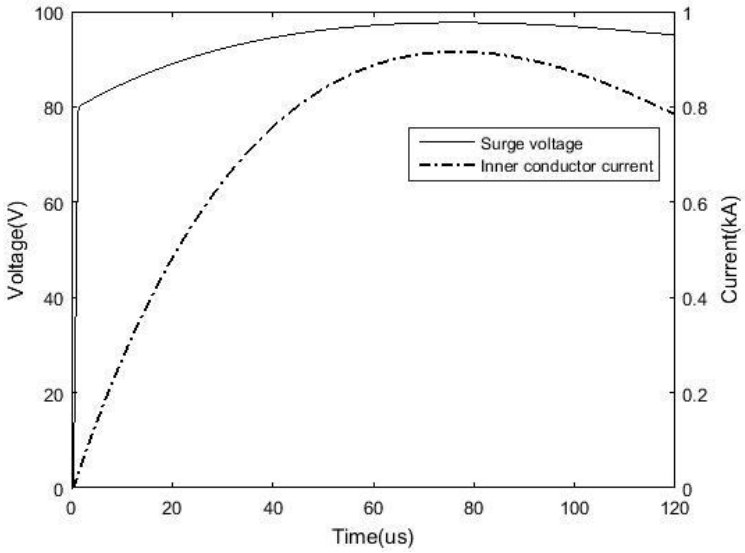

(b) With a MOV device at the bottom end

Figure 3.12 Waveforms of transverse voltage and conductor current at the bottom end of a lossy RF coaxial cable with considering the skin effect

Fig. 3.12 shows the waveforms of the current and voltage at the bottom end in two different cases; (a) with the MOV device absent and (b) with the MOV device

present. Without the MOV device, the surge current is carried by the outer conductor. The transverse voltage is basically affected by frequency-variant transfer impedance of the cable. Note that its rising time is longer than that of the source current due to the skin effect. As time goes on, the current waveform becomes much smoother. The transverse voltage tends to be determined by its DC resistance when the current changes slowly. With the MOV device, a portion of surge current will flow through the inner conductor. The voltage is clamped to a lower level. The inner conductor current has a much longer rising time, and becomes significant in the tail part of the current.

For comparison, simulation is made for the cable without considering the skin effect. In this case, the current density is uniformly distributed within the cable. The shell number in the inner and outer conductor is now reduced to 1. Fig. 3.13 shows the waveforms of the current and voltage in both case (a) and case (b). In the absence of a MOV device, it is found that the transverse voltage does not attenuate as significantly in the wave front as that shown in Fig. 3.12. This is due to small resistance of the outer conductor as the skin effect is not considered at high frequency. In the presence of the MOV device, the inner conductor current is greater than that shown in Fig. 3.12. Again, small resistance of the inner conductor at high frequency leads to an increase of inner conductor current. All these indicate that the skin effect could affect significantly the waveforms of the current and voltage in the cable. No instable behavior is encountered even if the calculation is

continued for 1.25 million time steps.

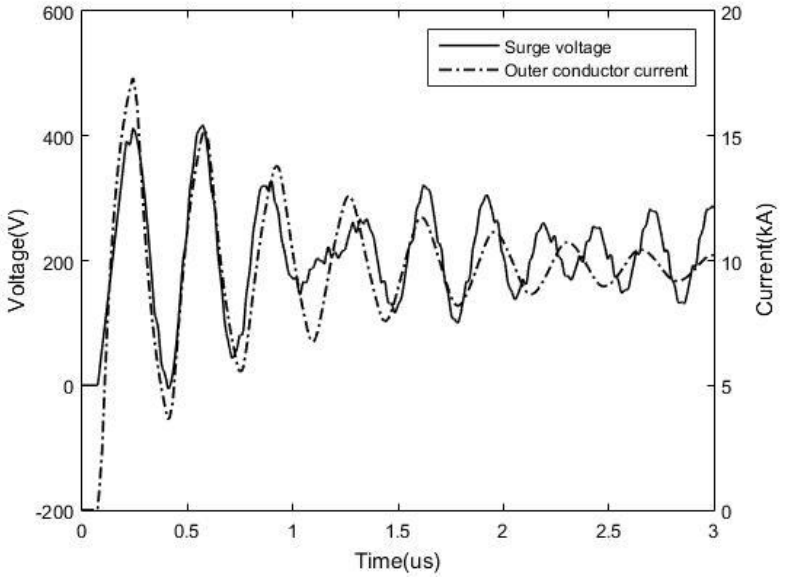

(a) Without a MOV device at the bottom end

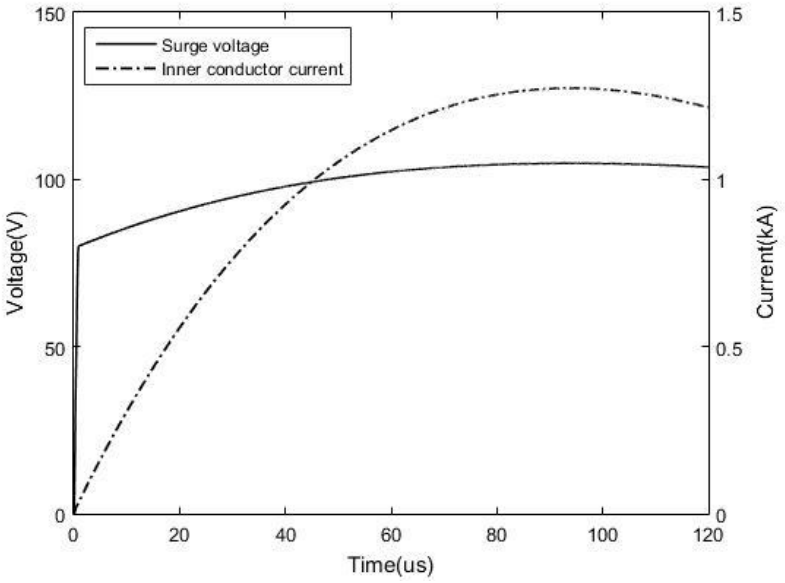

(b) With a MOV device at the bottom end

Figure 3.13 Waveforms of transverse voltage and conductor current at the bottom end of a lossy RF coaxial cable without considering the skin effect

3.4 Summary

This chapter presented an extended thin wire model for simulating wave or surge propagation on a lossy wire structure. A time-domain cascade circuit was developed to represent the wire structure, and the skin effect was fully considered in the circuit modelling. This circuit was integrated into a traditional thin-wire model in the FDTD simulation, and the updating equations were derived for solid round wires, hollow cylindrical tubes, and coaxial cables with and without conductors being bonded. In the coaxial structure, a lossy transmission line equivalent circuit, which incorporated cascade circuits for both inner and outer conductors, was established. The currents in both inner and outer conductors were not necessarily balanced.

The extended thin-wire model has been validated analytically and numerically. This model has been applied to analyze lightning current sharing in a lossy RF coaxial cable. Compared with the traditional FDTD method, this extended thin-wire model requires less memory space and less computation time in the simulation. The extended thin-wire model is shown to be stable for 1.25 million time steps.

4 Inclined thin-wire models with frequency-dependent Losses

This chapter presents a series of FDTD thin-wire models for inclined conductors considering frequency-dependent losses, including solid conductors, hollow tubes and coaxial conductors. In the model for coaxial conductors, a bidirectional coupling between the core and sheath conductors, and the eddy current in the sheath conductor are modeled. The currents in both core and sheath conductors are not necessarily balanced. Frequency-dependent parameters of the conductors are expressed first with the Bessel functions, and they are approximated by a vector fitting technique for time domain analysis. Section 4.1 reviews the fundamentals of the traditional inclined thin-wire model. The thin-wire models considering frequency-dependent losses are presented in Section 4.2 and 4.3. In Section 4.4, three case studies are performed to investigate and validate the proposed thin-wire models.

4.1 Traditional inclined thin-wire model

In the thin-wire model [46] proposed by Holland and Simpson, a conductor is posited along the center of the thin-wire mesh, as shown in Fig. 4.1. This conductor is divided into a series of line segments. As this mesh is separated from the FDTD mesh orientated in x, y and z directions, it is possible to simulate an inclined configuration with this model. The mesh is composed of a column of cubic cells.

The cell size of the thin-wire mesh in the longitudinal direction (l) is identical to the length of the line segment. The cell size in other directions is determined by the adjacent FDTD cell size as well as the angle of inclination [47].

In the thin-wire model domain, the wave propagation along a conductor is described with auxiliary equations. Both current I and charge Q on the conductor are used as updating variables, and they are located at line segment centers and edges respectively. The normal FDTD updating equations are used to compute the EM field outside the conductor.

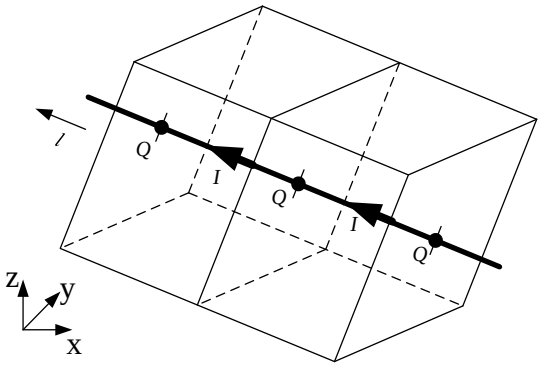

Figure 4.1 Configuration of the thin-wire mesh in the xyz coordinate system

Assuming the length of a conductor is much longer than its radius, and the EM field near the conductor is quasi-static, the auxiliary updating equations of the thin-wire model in the thin-wire mesh can be represented as,

$$\begin{aligned} &\langle L\rangle\cdot\left(\frac{\partial I}{\partial t}+\frac{1}{\varepsilon\mu}\frac{\partial Q}{\partial l}\right)=\langle E_l\rangle-E_s \\ &\frac{\partial Q}{\partial t}+\frac{\sigma}{\varepsilon}Q+\frac{\partial I}{\partial l}=0 \end{aligned} \quad . \tag{4.1}$$

where E_s denotes the surface electric field of the conductor. $\langle E_l\rangle$ is the averaged electric field within a thin-wire cubic cell. $\langle x\rangle$ means the parameter obtained by

an interpolated procedure. For an inclined thin-wire model, $\langle E_l \rangle$ is obtained by interpolation and synthesization with 12 electric field components in the FDTD cells (4 components per direction) using a trilinear interpolation method, which is fully described in [47].

These two meshes are coupled via an in-cell inductance $\langle L \rangle$. It is defined as,

$$\langle L \rangle = \frac{\mu \iiint_V \ln\left(D(x,y,z)/r_0\right) dxdydz}{2\pi \Delta x \Delta y \Delta z}. \tag{4.2}$$

where r_0 is the thin-wire radius, Δx, Δy and Δz are the cell sizes of the FDTD mesh. D is the radial length between a point in volume V and the inclined conductor. Volume V is the collocated region of the thin-wire cells and FDTD cells. Since the asymmetry and irregularity of the collocated region, the in-cell inductances are usually estimated separately with a numerical method.

The updating variable Q is normally substituted with virtual voltage V, i.e. $V = Q/C$ for handling multi-wire junctions. The auxiliary updating equations are then expressed as [58]

$$\langle L \rangle \cdot \frac{\partial I}{\partial t} + \frac{\partial V}{\partial l} = \langle E_l \rangle - E_s, \tag{4.3a}$$

$$\langle C \rangle \cdot \left(\frac{\partial \mathrm{V}}{\partial t} + \frac{\sigma}{\varepsilon} V \right) + \frac{\partial I}{\partial l} = 0. \tag{4.3b}$$

Note that the capacitance $\langle C \rangle$ is determined by two neighboring in-cell inductances as,

$$\langle C \rangle = \left(\frac{1}{\langle L_+ \rangle} + \frac{1}{\langle L_- \rangle} \right) \cdot \frac{\varepsilon \mu \Delta l}{2}, \tag{4.4}$$

where Δl is the length of line segments for the conductor.

During an updating cycle, the conductor current obtained in the thin-wire domain is interpolated and projected to the corresponding electric field components in the FDTD domain. Actually, the conductor carrying the current is represented as a series of equivalent current sources in the FDTD domain. The EM field outside the conductor is then updated in the FDTD cells, and the virtual voltage is updated with (4.3b). After that, E_l obtained in the FDTD domain is sent to the thin-wire domain for updating the conductor current together with E_s. The updating procedure of the traditional inclined thin-wire model is shown in Fig. 4.2.

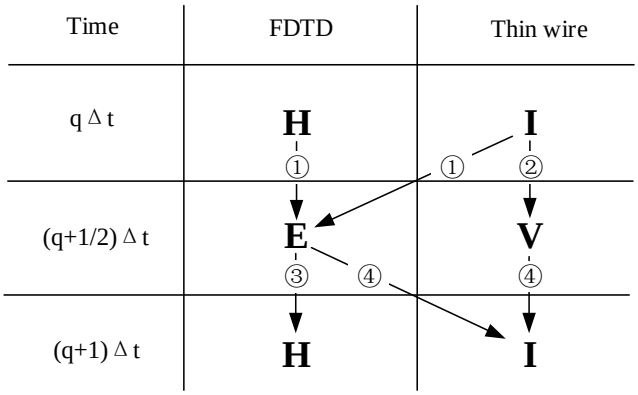

Figure 4.2 Calculation procedure of the traditional inclined thin-wire model with auxiliary updating equations

In this procedure, only lossless or conductors with DC loss are considered. The surface electric field E_s is simply equivalent to either zero or the constant voltage drop of IR_{Dc}, where R_{DC} is the DC resistance. Both bidirectional coupling between the core and sheath conductors, and the eddy current in the sheath

conductor were not considered.

4.2 Solid wires or hollow tubes with frequency-dependent losses

In a cylindrical conductor with finite conductivity, the surface electric field E_s is non-trivial. It is determined by the product of surface impedance Z and conductor current I. Note, the surface impedance is frequency-dependent, but can be expressed using Bessel functions [87], as shown in the Appendix. To incorporate the frequency-dependent parameters into the time-domain computation of current I with (4.3), the surface impedance is approximated with a vector fitting technique [88, 89] as a rational function. The surface electric field E_s in s domain is then expressed as

$$\begin{aligned} E_s(s) &= Z(s)\cdot I(s) \\ &= dI(s) + shI(s) + \sum_{m=1}^{N} \frac{r_m}{s-a_m} I(s) \end{aligned}, \tag{4.5}$$

where d and h represent the constant and differential components, and a_m and r_m are the poles and residues of rational functions.

By applying an inverse Laplace transform, the surface electric field, discretized in both time and space, is expressed as

$$E_s^{q-\frac{1}{2}}(k) = \left(\frac{d}{2} + \frac{h}{\Delta t} + \frac{1}{2}\sum_{m=1}^{N} B_m\right) I^q(k) + \left(\frac{d}{2} - \frac{h}{\Delta t}\right) I^{q-1}(k) + \frac{1}{2}\sum_{m=1}^{N}\left[\left(e^{a_m \Delta t}+1\right)\varphi_m^{q-1}(k)\right], \tag{4.6}$$

where

$$\begin{aligned} B_m &= r_m / a_m \cdot \left(e^{a_m \Delta t} - 1\right) \\ \varphi_m^q(k) &= B_m I^q(k) + e^{a_m \Delta t}\varphi_m^{q-1}(k) \end{aligned}.$$

In (4.6), q denotes the time step, and k denotes the index of a line segment. The

last term in the right hand side of (4.6) is a convolutional term.

Substituting (4.6) in (4.3a), the conductor current I considering the frequency-dependent loss in the conductor is obtained as

$$\begin{aligned} I^{q}(k) = {} & C_{Is,Is} \cdot I^{q-1}(k) + C_{Is,Vs} \cdot \begin{bmatrix} V^{q-1/2}(k+1/2) \\ -V^{q-1/2}(k-1/2) \end{bmatrix} \\ & + C_{Is,Es} \cdot \left\{ \left\langle E_{l}^{q-1/2}(k) \right\rangle - \frac{1}{2} \sum_{m=1}^{N} \left[\left(e^{A_m} + 1 \right) \cdot \varphi_{m}^{q-1}(k) \right] \right\} \end{aligned} \tag{4.7}$$

where

$$C_{Is,Is} = \frac{2L - d\Delta t + 2h}{DENO}$$

$$C_{Is,Vs} = -\frac{2\Delta t}{\Delta l \cdot DENO}$$

$$C_{Is,Es} = \frac{2\Delta t}{DENO}$$

$$DENO = 2L + d\Delta t + 2h + \Delta t \sum_{m=1}^{N} B_m$$

The updating equation of the conductor voltage V remains the same as (4.3b).

4.3 Coaxial conductors with frequency-dependent losses

4.3.1 Surface electric field of the sheath conductor

The coaxial conductors consist of a core conductor, an insulation gap and a sheath conductor, as shown in Fig. 4.3. This structure carries both currents I_{co} in the core and I_{sh} in the sheath. These currents may not be necessarily balanced in the simulation. Note that the structure length is much longer than its cross sectional dimensions. Divide the structure into a number of short segments. The electric field on the outer surface of the sheath conductor in segment k can be then expressed with core and sheath currents in the frequency domain, as follows:

$$E_s(k) = Z_{c,co} \cdot I_{co}(k) + Z_{c,sh} \cdot I_{sh}(k). \tag{4.8}$$

where $Z_{c,co}$ and $Z_{c,sh}$ are the surface impedances on the outer sheath surface caused by the core and sheath currents I_{co} and I_{sh}. The detailed expressions of surface impedances are given in the Appendix.

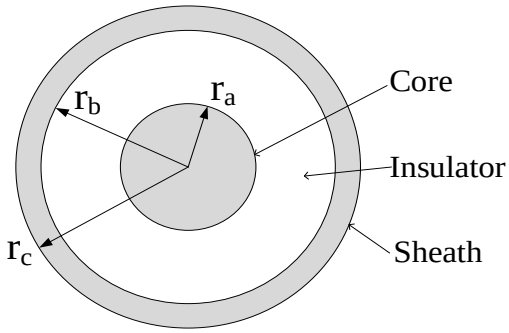

Figure 4.3 Cross section of the coaxial conductors

Note that total current I_t of a wire structure is used in the auxiliary equation (4.3), instead of I_{co} and I_{sh}. It is necessary to build additional equations in the coaxial wire structures, apart from the auxiliary equations. For a long coaxial wire structure, frequency-domain transmission line equations in discrete form can be established, as follows:

$$\frac{V_T(k+1/2) - V_T(k-1/2)}{\Delta l} = -sL_T I_{co}(k) + Z_{a,sh} I_{sh}(k) - (Z_{c,co} - Z_{a,co}) I_{co}(k), \tag{4.9a}$$

$$\frac{I_{co}(k) - I_{co}(k-1)}{\Delta l} = -sC_T V_T(k-1/2), \tag{4.9b}$$

$$I_t(k) = I_{co}(k) + I_{sh}(k), \tag{4.9c}$$

where V_T is the transverse voltage on the gap of the coaxial wire structure, $Z_{a,x}$ and $Z_{b,x}$ (x=*co* or *sh*) are the surface impedances on the core surface and inner sheath surface contributed by the current in conductor x. Both circuit parameters L_T and C_T are given by

$$L_T = \frac{\mu}{2\pi}\ln\left(r_a / r_c\right)$$
$$C_T = 2\pi\varepsilon \ln^{-1}\left(r_a / r_c\right)$$

Surface impedances in the lossy conductors are frequency-dependent. Similar to the solid conductors, the vector fitting technique is applied to express surface impedances with rational functions for time-domain simulation, as follows:

$$\begin{aligned}
Z_{a.co}(s) &= d_c + sh_c + \sum_{m=1}^{N}\frac{r_{cm}}{s-a_{cm}},\\
Z_{b,co}(s) &= d_{s1} + sh_{s1} + \sum_{m=1}^{N}\frac{r_{s1m}}{s-a_{s1m}},\\
Z_{b,sh}(s) &= d_{s2} + sh_{s2} + \sum_{m=1}^{N}\frac{r_{s2m}}{s-a_{s2m}},\\
Z_{c,co}(s) &= d_{o1} + sh_{o1} + \sum_{m=1}^{N}\frac{r_{o1m}}{s-a_{o1m}},\\
Z_{c,sh}(s) &= d_{o2} + sh_{o2} + \sum_{m=1}^{N}\frac{r_{o2m}}{s-a_{o2m}}.
\end{aligned} \tag{4.10}$$

By substituting (4.9c) in (4.9a) and (4.9b), and taking an inverse Laplace transform, both discrete core current and gap voltage in the time domain can be expressed with the total current I_t, as follows:

$$\begin{aligned}
I_{co}^{q}(k) = {} & C_{Ic,Ic}I_{co}^{q-1}(k) + C_{Ic,Itp}I_{t}^{q}(k) + C_{Ic,Itn}I_{t}^{q-1}(k) + \\
& C_{Ic,\varphi}\psi_{co}^{q-1}(k) + C_{Ic,V_T}\left[V_T^{q-1/2}(k+1/2) - V_T^{q-1/2}(k-1/2)\right],
\end{aligned} \tag{4.11a}$$

$$V_T^{q+1/2}(k-1/2) = V_T^{q-1/2}(k-1/2) + C_{V_T,Ic}\left[I_{co}^{q}(k) - I_{co}^{q}(k-1)\right], \tag{4.11b}$$

where

$$C_{Ic,Ic} = -\left(\frac{d_c - d_{s1} + d_{s2}}{2} + \frac{L_T + h_c - h_{s1} + h_{s2}}{\Delta t}\right)\Big/ DENO_{co}$$
$$C_{Ic,Itp} = \left(\frac{d_{s2}}{2} + \frac{h_{s2}}{\Delta t} + \frac{1}{2}\sum_{m=1}^{N}B_{s2m}\right)\Big/ DENO_{co}$$
$$C_{Ic,Itn} = \left(\frac{d_{s2}}{2} - \frac{h_{s2}}{\Delta t}\right)\Big/ DENO_{co}$$
$$C_{Ic,V_T} = -1\Big/\left(\Delta l \cdot DENO_{co}\right)$$
$$C_{Ic,\varphi} = -1\Big/\left(2 \cdot DENO_{co}\right)$$

$$DENO_{co} = \frac{d_c - d_{s1} + d_{s2}}{2} + \frac{L_T + h_c - h_{s1} + h_{s2}}{\Delta t} + \frac{1}{2}\sum_{m=1}^{N}\left(B_{cm} - B_{s1m} + B_{s2m}\right)$$

$$C_{V_T,Ic} = -\Delta t / \Delta l / C_T$$

$$\psi_{co}^{q-1}(k) = \sum_{m=1}^{N}\left[\left(e^{a_{cm}\cdot\Delta t}+1\right)\varphi_{co.cm}^{q-1} - \left(e^{a_{s1m}\cdot\Delta t}+1\right)\varphi_{co.s1m}^{q-1} + \left(e^{a_{s2m}\cdot\Delta t}+1\right)\varphi_{co.s2m}^{q-1} - \left(e^{a_{s2m}\cdot\Delta t}+1\right)\varphi_{t.s2m}^{q-1}\right]$$

$$\varphi_{co.xm}^{q}(k) = B_{xm}\cdot I_{co}^{q}(k) + e^{a_{xm}\cdot\Delta t}\cdot\varphi_{co.xm}^{q-1}(k)$$

$$\varphi_{t.xm}^{q}(k) = B_{xm}\cdot I_{t}^{q}(k) + e^{a_{xm}\cdot\Delta t}\cdot\varphi_{t.xm}^{q-1}(k)$$

$$B_{xm} = \frac{r_{xm}}{a_{xm}}\left(e^{a_{xm}\cdot\Delta t}-1\right)$$

With (9c) and (11a), the electric field on the outer surface of the sheath E_s in (8) can be estimated as

$$E_s^{q-1/2}(k) = C_{It,Itn}I_t^{q}(k) + C_{It,Itp}I_t^{q-1}(k) + C_{It,Icp}I_{co}^{q-1}(k) + C_{Es,Icp}C_{Ic,V_T}\left[V_T^{q-1/2}(k+1/2) - V_T^{q-1/2}(k-1/2)\right] + C_{Ic,\varphi}\psi_{co}^{q-1}/2 + C_{Es,\varphi}\psi_{Es}^{q-1} \tag{4.12}$$

where

$$I_t(k) = I_{co}(k) + I_{sh}(k)$$

$$C_{It,Itn} = C_{Es,Icp}C_{Ic,Itp} + C_{Es,Itp}$$

$$C_{It,Itp} = C_{Es,Icp}C_{Ic,Itn} + C_{Es,Itn}$$

$$C_{It,Icp} = C_{Es,Icp}C_{Ic,Ic} + C_{Es,Icn}$$

$$C_{Es,Icp} = \frac{d_{o1} - d_{o2}}{2} + \frac{h_{o1} - h_{o2}}{\Delta t} + \frac{1}{2}\sum_{m=1}^{N}\left(B_{o1m} - B_{o2m}\right)$$

$$C_{Es,Icn} = \frac{d_{o1} - d_{o2}}{2} + \frac{h_{o1} - h_{o2}}{\Delta t}$$

$$C_{Es,Itp} = \frac{d_{o2}}{2} + \frac{h_{o2}}{\Delta t} + \frac{1}{2}\sum_{m=1}^{N}B_{o2m}$$

$$C_{Es,Itn} = \frac{d_{o2}}{2} + \frac{h_{o2}}{\Delta t}$$

$$\psi_{Es}^{q-1}=\sum_{m=1}^{N}\left[\left(e^{a_{o1m}\cdot\Delta t}+1\right)\varphi_{co.o1m}^{q-1}-\left(e^{a_{o2m}\cdot\Delta t}+1\right)\varphi_{co.o2m}^{q-1}+\left(e^{a_{o2m}\cdot\Delta t}+1\right)\varphi_{t.o2m}^{q-1}\right]$$

4.3.2 Current distribution in the coaxial conductors

To update the field components in the FDTD domain as shown in Fig. 4.2, the total wire structure current I_t needs to be determined. Substituting the surface electric field given in (4.12) into the discrete version of auxiliary equations in (3a) yields I_t in the time domain as

$$\begin{aligned}I_t^q(k)=&C_{It,It}\cdot I_t^{q-1}(k)+C_{It,Ic}\cdot I_{co}^{q-1}(k)+C_{It,V_T}\cdot\left[V_T^{q-1/2}(k+1/2)-V_T^{q-1/2}(k-1/2)\right]\\&+C_{It,Vs}\cdot\left[V^{q-1/2}(k+1/2)-V^{q-1/2}(k-1/2)\right]+\psi_t^{q-1}+C_{It,E_l}\cdot\left\langle E_l^{q-1/2}(k)\right\rangle\end{aligned},\qquad(4.13)$$

where

$$C_{It,It}=\left(\langle L\rangle/\Delta t-C_{Es,Icp}\cdot C_{Ic,Itn}-C_{Es,Itn}\right)\Big/DENO_t$$

$$C_{It,Ic}=-\left(C_{Es,Icp}\cdot C_{Ic,Ic}+C_{Es,Icn}\right)\Big/DENO_t$$

$$C_{It,V_T}=-C_{Es,Icp}\cdot C_{Ic,V_T}/DENO_t$$

$$C_{It,Vs}=-1/(\Delta d\cdot DENO_t)$$

$$C_{It,E_l}=1/DENO_t$$

$$\psi_t^{q-1}(k)=-\left(C_{Es,Icp}\cdot C_{Ic,\varphi}\cdot\psi_{co}^{q-1}(k)+C_{Es,\varphi}\cdot\psi_{Es}^{q-1}(k)\right)\Big/DENO_t$$

$$DENO_t=\langle L\rangle/\Delta t+C_{Es,Icp}\cdot C_{Ic,Itp}+C_{Es,Itp}$$

Both core and sheath currents I_{co} and I_{sh} are then calculated with (4.11a) and (4.9c) after the total structure current I_t is obtained.

4.3.3 Boundary conditions for the coaxial conductors

At each end of a wire structure, the current continuity is enforced by a multi-junction equation in [47] no matter whether there is any external wire connected

or not. Additional equations must be established to include gap voltage at the end of the coaxial wire structure for updating FDTD field components.

Fig. 4.4 illustrates the arrangement of M external wires connected to the core of the coaxial wire structure. A virtual wire segment of length Δl is added to the end of the core conductor as the representation of the external wires, as shown in Fig. 4(b). This wire segment carries the total current of all external wires, as follows:

$$I_{co,A}^{q} = \sum_{m=1}^{M} I_{tm}^{q} \tag{4.14}$$

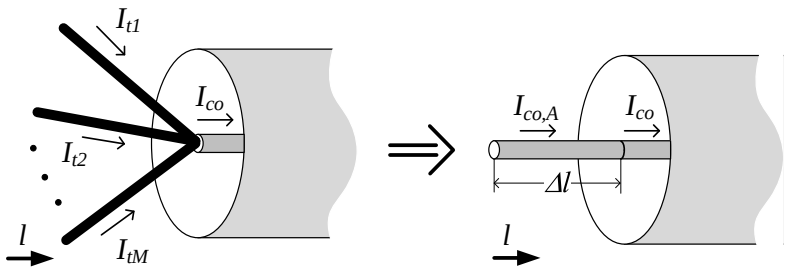

(a) Multi-wire connection (b) Virtual wire connection

Figure 4.4 The structure of multi-junctions at coaxial conductor terminal

With (4.9b), the gap voltage at the end of the coaxial conductors can be obtained with the currents in the virtual core segment and its adjacent segment. The updating equation for the gap voltage V_{A} at the end shown in Fig. 4.4 is derived as

$$V_{T,A}^{q+1/2} = V_{T}^{q-1/2} + C_{V_T,Ic} \cdot \left[I_{co}^{q}(1) - I_{co,A} \right] \tag{4.15}$$

The updating equation at other ends of the wire structure can be derived in a similar manner. In case the core is open at the end of the wire structure, I_{co} is simply set to be zero.

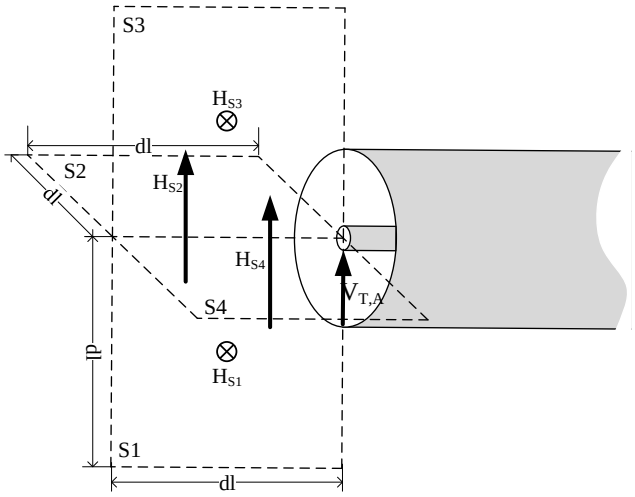

Figure 4.5 Configuration for evaluating magnetic fields at the structure end

The gap voltage, existing at the end of the coaxial wire structure, will alter EM field in its vicinity in the FDTD cells. To establish a link between the voltage at the end and its surrounding EM field, two orthogonal sets of double square surfaces are constructed at the structure end along the wire axis, as shown in Fig. 4.5. The size of these surfaces is equal to the segment length of the conductors. The Faraday's law is then applied in each surface for evaluating H field components in these areas, as follows:

$$H_{s1} = H_{s2} = \frac{dt}{\mu \cdot \Delta l^2} \cdot V_{T,A} \tag{4.16}$$

$$H_{s3} = H_{s4} = -\frac{dt}{\mu \cdot \Delta l^2} \cdot V_{T,A}$$

where H_{si} is the averaged magnetic field on the corresponding surface S_i. In the normal FDTD updating cycle of magnetic fields, H field components calculated with (4.16) are interpolated and superposed to the FDTD magnetic field components in the corresponding FDTD cells.

4.3.4 Flow chart

The calculation flow chart of the proposed thin-wire model is illustrated in Fig. 4.6. The detailed procedure is summarized, as follows:

1) Update electric field component *E* in the FDTD domain using I_t and *H*;
2) Update virtual voltage *V* in the thin-wire domain with (4.3b) using I_t;
3) Update gap voltage V_T at the end of the coaxial conductors with (4.11b) using I_{co};
4) Update total current I_t with (4.13) using I_{co}, *E*, *V* and V_T;
5) Update core conductor current I_{co} inside the coaxial wire structure with (4.13a) using V_T and I_t. If necessary, update sheath conductor current I_{sh} with (4.9c) using I_t and I_{co};
6) Update magnetic field component *H* in the FDTD domain with (4.15) using V_T and *E*.

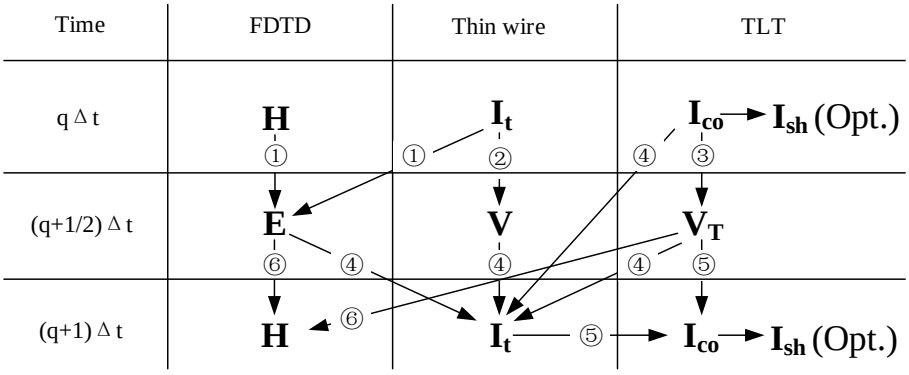

Figure 4.6 Calculation procedure of the proposed thin-wire model for coaxial conductors

4.4 Case studies

The proposed thin-wire models for inclined lossy conductors are tested under transient or wave propagating conditions in this section. The issues of propagation velocity and frequency-dependent losses on the conductors are investigated. The simulation results are compared with those obtained by analytical and numerical methods for validation.

4.4.1 Propagation velocity

The wave propagation velocity of the proposed thin-wire model is tested first. Fig. 4.7 shows the configuration of a dipole structure with the voltage source located between two conductive arms [90]. The length and radius of each conductive arm are 1 m and 0.1 mm, respectively. The conductivity of the arms is 1e7 S/m. The voltage source at the feeding point generates a Gaussian impulse expressed by

$$V(t) = A_0 \exp\left[-\frac{1}{2}\left(\frac{t-\mu}{\sigma}\right)^2\right], \tag{4.17}$$

where $A_0 = 1\text{V},\ \sigma = 1 \times 10^{-9}s,\ \mu = 2.5 \times 10^{-9}s$. The current waveform at the voltage source is measured to determine the time when the impulse travels back to the feeding point.

The conductive arms have two degrees of freedom: θ and φ, as shown in Fig. 4.7. Both θ and φ are defined respectively as an angle between the conductor and the z axis, and an angle between the conductor projection on the xy plane and the

x axis. θ varies from 0° to 90° with an interval of 10°. φ varies from 0° to 45° with an interval of 15° for the symmetrical geometry.

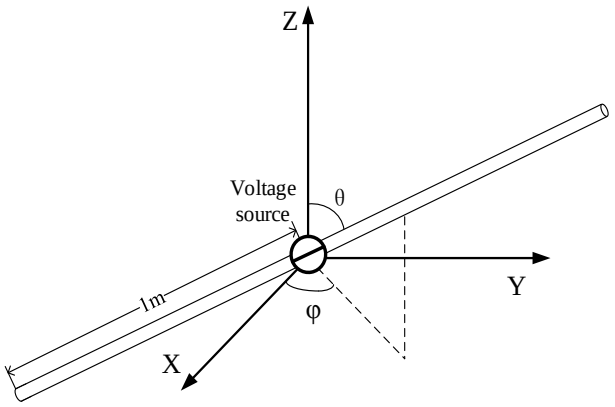

Figure 4.7 A dipole structure with an impulse voltage at its feeding point

In the FDTD domain, the cell size is set to be 1 cm, and the time step is 19.2 ps. The perfectly matched layer (PML) absorbing boundary conditions are applied to absorb unwanted wave reflections in six boundaries. In the thin-wire domain, the solid conductor is divided into 201 line segments. The voltage source and current sensor are located in segment 101. The propagation velocity of the proposed thin-wire model with different inclinations is shown in Fig. 4.8. Note, the velocity value is normalized by the result for $\theta = \varphi = 0^\circ$. According to the simulation results, the relative errors of the propagation velocity are less than 1%. Compared with the error of the staircase approximation method [90], which is as large as 14%, the proposed thin-wire model performs well. It is concluded that the proposed model can depict the wave propagation along an inclined direction with a correct velocity.

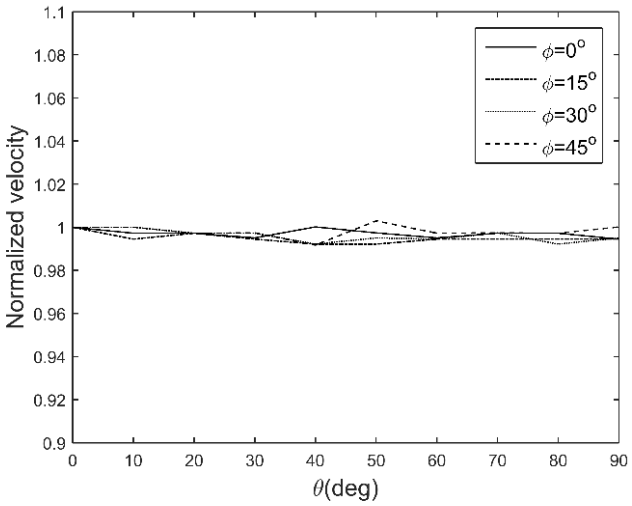

Figure 4.8 Normalized propagation velocity of the proposed thin-wire model with different inclinations

4.4.2 Frequency-dependent loss of solid wire and hollow tube

A lossy conductor is arranged to be in parallel with a perfect ground, as shown in Fig. 4.9. The conductor is assumed to be infinitely long. One end of this conductor is connected to the ground via a lossless wire and an ideal current source. The current source generates a 100 MHz sinusoidal wave. Two types of wire structures are tested, including a solid conductor and a hollow tube. The geometric dimensions of these two conductors are shown in Table 4.1. The conductivity of these conductors is set to be 1e5 S/m for signifying the conductive loss effect. Five current sensors are placed along each of two lossy wire structures at the distance of 10 m, 20 m, 30 m, 40 m and 50 m away from Point P. To test the accuracy of the proposed model under different positions, two configurations of the wire structures are investigated, as shown in Fig.4.10. In Config. A, Point P is

positioned at the corner of the FDTD cell. The lossy wire is located at a height of 0.3 m above the ground. In Config. B, Point P is positioned at the cell center. The lossy wire is then at the height of 0.35 m above the ground. In these two configurations, φ is equal to either 0° or 45°.

Table 4.1 Geometric dimensions of wire structures

Wire structures	Core radius (mm)	Sheath radius (mm)	Thickness (mm)
Solid conductor	1	\	\
Hollow tube	\	2	0.1
Coaxial conductor	1	2	0.1

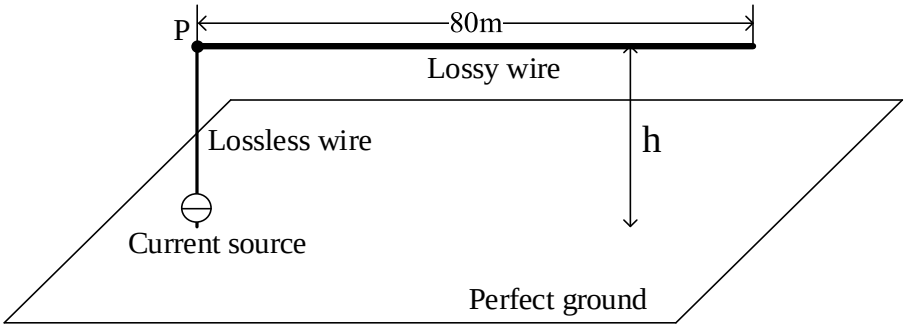

Figure 4.9 Configuration of frequency-dependent loss validation with a solid conductor or a hollow tube

Wave propagation over the tested conductor can be analyzed analytically with the transmission line theory (TLT) [85] as the conductor runs in parallel with the ground plane. The peak current along a wire with no reflected wave at angular frequency ω is given by,

$$I(x,t) = I_0 e^{-\alpha x} \sin(\omega t - \beta x), \tag{4.18}$$

where

$$\alpha = \sqrt{[(\omega^2 LC)^2 + (\omega^2 RC)^2]^{1/2} - \omega^2 LC}\,/\sqrt{2}$$
$$\beta = \sqrt{[(\omega^2 LC)^2 + (\omega^2 RC)^2]^{1/2} + \omega^2 LC}\,/\sqrt{2}$$

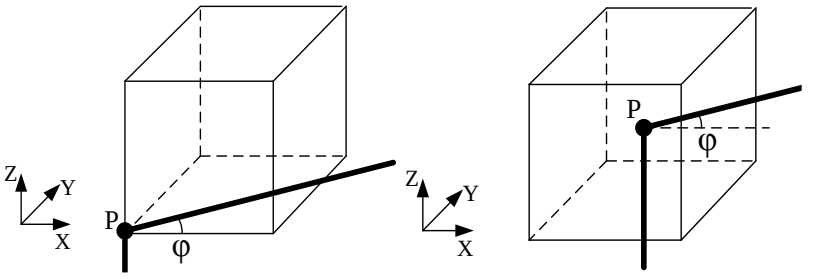

(a) Config. A: cell corner (b) Config. B: cell center

Figure 4.10 Location of Point P on the infinitely-long conductor

Table 4.2 Simulation results of a lossy solid wire

φ	Method	Current/A				Relative Error
		l=20m	l=30m	l=40m	l=50m	
Config. A: Point P located at the cell corner, h=0.3m						
0^o	Prop.	0.9319	0.8686	0.8096	0.7547	1.51%
	TLT	0.9264	0.8584	0.7952	0.7367	
45^o	Prop.	0.9290	0.8599	0.7965	0.7397	0.26%
	TLT	0.9265	0.8583	0.7952	0.7367	
Config. B: Point P located at the cell center, h=0.35m						
0^o	Prop.	0.9266	0.8588	0.7959	0.7376	0.43%
	TLT	0.9283	0.8619	0.8000	0.7426	
45^o	Prop.	0.9256	0.8591	0.7961	0.7380	0.43%
	TLT	0.9283	0.8617	0.8000	0.7427	

Both C and L are the capacitance and inductance of a traditional transmission line respectively. Resistance R is frequency-dependent, and can be determined using the formulas for the internal impedance of round conductors [86].

Table 4.3 Simulation results of a lossy hollow tube

φ	Method	Current/A				Relative Error
		l=20m	l=30m	l=40m	l=50m	
Config. A: Point P located at the cell corner, h=0.3m						
0^o	Prop.	0.8951	0.8014	0.7175	0.6425	2.60%
	TLT	0.8862	0.7852	0.6958	0.6165	
45^o	Prop.	0.8880	0.7904	0.7016	0.6248	0.77%
	TLT	0.8861	0.7852	0.6957	0.6165	
Config. B: Point P located at the cell center, h=0.35m						
0^o	Prop.	0.8870	0.7873	0.6986	0.6201	0.45%
	TLT	0.8889	0.7902	0.7024	0.6244	
45^o	Prop.	0.9330	0.8817	0.8474	0.8101	1.01%
	TLT	0.9462	0.8952	0.8470	0.8014	

In the FDTD domain, the cell size and time step are defined as 0.1 m and 9.6225 ps. Five planes of the PML boundary conditions and one plane of the perfect electrical conductor (PEC) boundary condition are applied on the domain boundaries. In the proposed thin-wire model, the lossy wire is divided into 800 line segments, and the lossless wire is divided into 3 segments in Config. A or 4

segments in Config. B line segments.

The simulation results of the solid wire and hollow tube obtained with the proposed thin-wire model and TLT are shown in Table 4.2 and Table 4.3. The magnitude of the current wave measured at each location is normalized by the current magnitude at l=10 m. It is noticed that the results obtained from the two methods match very well. The averaged relative errors for the solid wire and hollow tube in all configurations are 0.62% and 1.21%, respectively. This indicates that the proposed thin-wire model is applicable to lossy solid wires and hollow tubes.

4.4.3 Coaxial conductors

A lossy coaxial wire structure is tested, as shown in Fig. 4.11. It runs at a height of 0.3 m above a perfect ground. The length of the wire structure is 20 m. The geometric dimensions are given in Table 4.1. The conductivity of both core and sheath conductors are 1e6 S/m. At one end of the coaxial wire structure, the core is extended further for a distance of 0.5 m horizontally, and then is connected to ground via a lossless wire and an ideal current source. The current source generates a Gaussian impulse, with parameters of $A_0 = 1$ A, $\sigma = 9 \times 10^{-10}\, s$ and $\mu = 5 \times 10^{-9} s$. The other end of the coaxial wire structure, the core remains open. The sheath is grounded via lossless wires at two ends of the structure. There is no electrical connection between the core and sheath. The radius of the lossless wires is 1 mm. Similar to the arrangement in Section V (B), two configurations for

the position of P are considered with $\varphi = 0^{\circ}$ or $\varphi = 45^{\circ}$. The current waveforms at the middle point of the core conductor are measured. The results obtained with the proposed model is compared with those from the extended thin-wire model in [42] for validation. In the extended thin-wire model the lossy coaxial conductors are arranged to be in parallel with the FDTD cell edges.

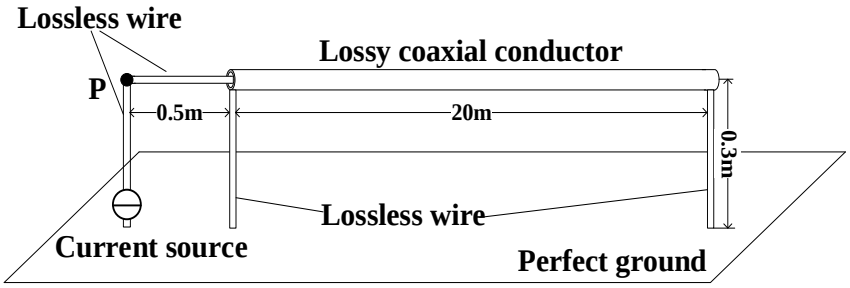

Figure 4.11 Configuration of the lossy coaxial conductors

In the FDTD domain, the cell size and time step are set to be 0.1 m and 9.6225 ps. The PEC boundary condition is applied at the bottom side of the problem domain. The PML absorbing boundary conditions are applied on the other sides of the domain. In the thin-wire model, the coaxial wire structure is divided into 200 line segments. The horizontal lossless wire is divided into 5 segments, and the vertical lossless wires are divided into 3 segments in Config. A or 4 segments in Config. B.

The current waveforms measured at the middle point of the core conductor under two configurations are shown in Fig. 4.12. In all these cases, current waveforms obtained with two methods match well. The proposed thin-wire model can simulate the inclined coaxial conductors considering frequency-dependent loss

with reasonable accuracy.

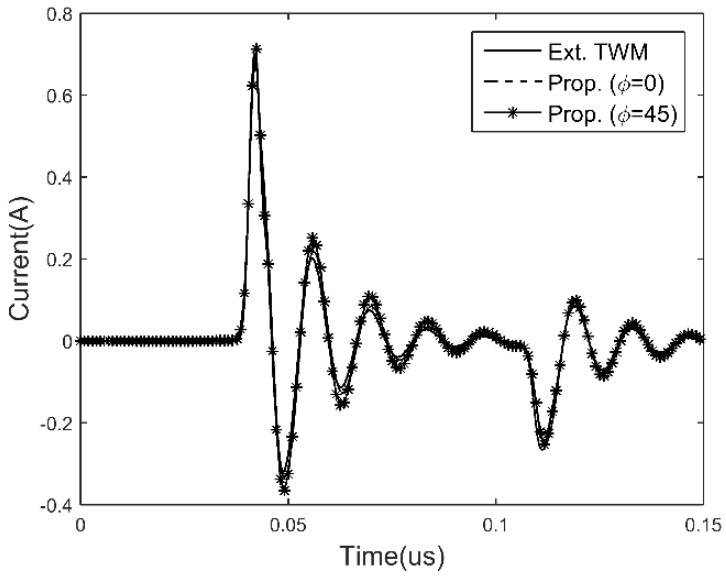

(a) Config A: P at cell corner

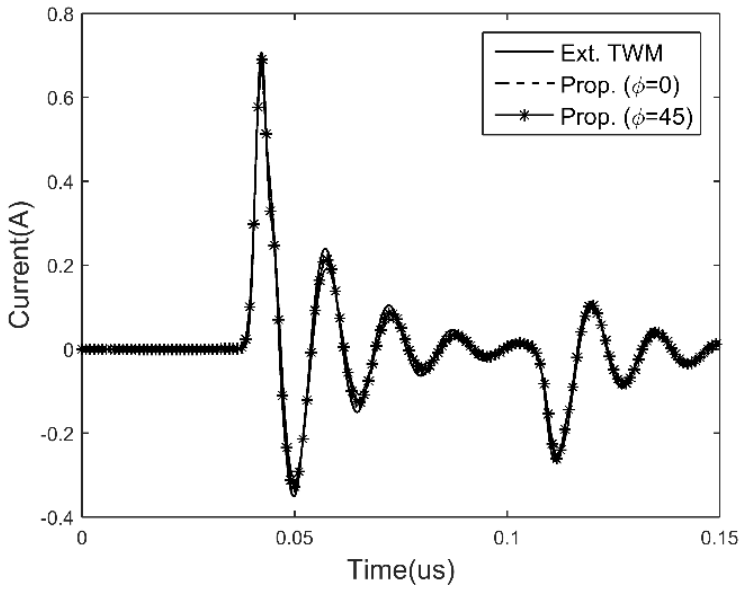

(b) Config B: P at cell center

Figure 4.12 Current waveforms at the middle of the core conductor considering the frequency-dependent loss

4.5 Summary

This chapter presented a series of inclined thin-wire models considering frequency-dependent losses for solid conductors, hollow tubes and coaxial conductors with reasonable accuracy. The Bessel functions and the vector fitting technique were adopted to incorporate the frequency-dependent parameters of the conductors into the time-domain auxiliary equations. Transmission line equations of coaxial conductors were established for wave propagation analysis and linking the wire structure current and conductor currents together. Boundary conditions for the coaxial wire structure were provided as well. The bidirectional coupling between core and sheath conductors was realized with these equations.

Transient simulations in three different cases were performed using the proposed inclined thin-wire models. It is found that wave propagation along inclined lossy conductors is correctly depicted, with the velocity error of less than 1% and the attenuation error of less than 1.5%. The transient currents in the inclined coaxial conductors match well with those obtained from the extended thin-wire models under the assumption that the wire structure is arranged to be in parallel with the FDTD cell edges.

4.6 Appendix

Consider a coaxial wire structure consists of a core conductor and a sheath conductor withe with radii r_a, r_b and r_c, as illustrated in Fig. 4.2. Surface

impedance $Z_{x,y}$ (x=*a, b* or *c,* and y=*co* or *sh*) on surface x contributed by the source current in y is represented as [87],

$$Z_{a,co} = \frac{j\omega\mu_{co}}{2\pi R_c} \cdot \frac{I_0(R_c)}{I_1(R_c)}$$

$$Z_{b,co} = j\omega\mu_{sh}\left[\frac{[K_1(R_a)R_a - K_1(R_b)R_b]I_0(R_a)}{2\pi R_a R_b[I_1(R_b)K_1(R_a) - I_1(R_a)K_1(R_b)]} - \frac{[I_1(R_b)R_b - I_1(R_a)R_a]K_0(R_a)}{2\pi R_a R_b[I_1(R_b)K_1(R_a) - I_1(R_a)K_1(R_b)]}\right]$$

$$Z_{b.sh} = j\omega\mu_{sh}\frac{1}{2\pi R_a R_b[I_1(R_b)K_1(R_a) - I_1(R_a)K_1(R_b)]}$$

$$Z_{c.co} = j\omega\mu_{sh}\left[\frac{[K_1(R_a)R_a - K_1(R_b)R_b]I_0(R_b)}{2\pi R_a R_b[I_1(R_b)K_1(R_a) - I_1(R_a)K_1(R_b)]} - \frac{[I_1(R_b)R_b - I_1(R_a)R_a]K_0(R_b)}{2\pi R_a R_b[I_1(R_b)K_1(R_a) - I_1(R_a)K_1(R_b)]}\right]$$

$$Z_{c.sh} = j\omega\mu_{sh}\frac{K_1(R_a)I_0(R_b) + I_1(R_a)K_0(R_b)}{2\pi R_b[I_1(R_b)K_1(R_a) - I_1(R_a)K_1(R_b)]}$$

where $R_x = \gamma r_x$ and $\gamma^2 = j\omega\mu(\sigma + j\omega\epsilon)$. σ is the conductivity of the conductor. I_n is the modified Bessel function of the first kind at order n. A solid conductor or a cylindrical tube is a special case of the coaxial wire structure, in which either the sheath or the core is absent.

5 Thin-wire models with non-circular cross section

In this chapter, an FDTD thin wire model integrated with the equivalent circuit and surface charge simulation methods is proposed to deal with lossy wire conductors with non-circular cross section. This model is developed from a traditional thin wire model [52], and is established by providing unique correction factors of EM fields around the conductors and electric field on the conductor surface. These parameters are both frequency-dependent and position-variant. The EM field distribution in and around the conductors are investigated with several numerical techniques under quasi-static conditions, such as surface charge simulation method, equivalent circuit method (ECM). Section 5.1 of this chapter presents a brief review of the traditional thin wire model. In Section 5.2 the detail of the proposed model is described, and several key issues are addressed, such as the correction factors and the frequency-variant conductor loss. Section 5.3 presents the analytical and numerical validation of the proposed model. Finally, this method is applied to analyze lightning surges in a light rail system under a direct lightning stroke.

5.1 Traditional Railton thin wire model

The thin wire model [52] proposed by Railton introduced the concepts of line/surface averaged field quantities, and mimicked a round and lossless conductor by implementing a modified assigned material parameters (MAMPs)

technique.

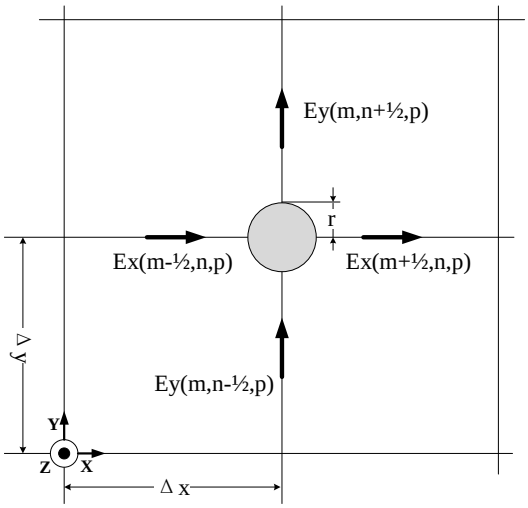

Figure 5.1 Cross section of a thin wire model with a circular cross section

During an FDTD updating period, the E field components, which are calculated by the H field components at half time step early, are the surface averaged field. At the next half time step, the E field components, as the line averaged field, are used to update H field components, and vice versa. Therefore, a line/surface averaged field transformation exists inherently between consecutive updating cycles in the FDTD method. Note that in a normal FDTD calculation region, the field distribution inside the corresponding cubic mesh is regarded as uniform. The line/surface-field transformation completes naturally without any further modification. However, the field distribution near a round conductor is no longer uniform.

Take a z-oriented round conductor as an example, as shown in Fig. 5.1. The line and surface averaged fields of $Ex(m+1/2,n,p)$ are defined as,

$$\left\langle\left\langle Ex\left(m+\tfrac{1}{2},n,p\right)\right\rangle\right\rangle_{yz}=\frac{\int_{(n-\frac{1}{2})\Delta y}^{(n+\frac{1}{2})\Delta y}Ex\left((m+\tfrac{1}{2})\Delta x,y,p\Delta z\right)dy}{\Delta y} \tag{5.1a}$$

$$\left\langle Ex\left(m-\tfrac{1}{2},n,p\right)\right\rangle_{x}=\frac{\int_{(m-1)\Delta x}^{m\Delta x-r}Ex\left(x,n\Delta y,p\Delta z\right)dx}{\Delta x} \tag{5.1b}$$

where $\langle a\rangle_x$ is the line averaged field along the x-oriented line, and $\langle\langle a\rangle\rangle_{yz}$ is the surface averaged field on the y-z surface. In (5.1) $\Delta x, \Delta y$ and Δz are the sizes of a cell in the x, y and z directions. These quantities in a cell around the conductor are generally not identical. Correction factors are then required to determine in advance for the line/surface averaged field transformation. A correction factor is defined as a ratio of the surface averaged field to the line averaged field. In the Railton's thin wire model, the correction factor is integrated into material parameters, which is equivalent to construct a thin wire by modifying assigned material parameters. For instance, the correction factor of Ex and Hx of a lossless round conductor associated with permittivity and permeability are represented as,

$$\varepsilon_x=\frac{\left\langle\left\langle Ex\right\rangle\right\rangle_{yz}}{\left\langle Ex\right\rangle_{x}}=\frac{2\tan^{-1}\left(\Delta y/\Delta x\right)}{\ln\left(\Delta x/a\right)}\frac{\Delta x}{\Delta y}, \tag{4.2a}$$

$$\mu_x=\frac{\left\langle\left\langle Hx\right\rangle\right\rangle_{yz}}{\left\langle Hx\right\rangle_{x}}=\frac{\ln\left(\Delta y/a\right)}{2\tan^{-1}\left(\Delta x/\Delta y\right)}\frac{\Delta x}{\Delta y}. \tag{4.2b}$$

5.2 Proposed thin wire model

It is known that correction factors of both E and H field components for a circular and lossless conductor are constant, symmetrical and frequency-invariant. However, for a lossy conductor with non-circular cross section, the EM field

distribution around the conductor is not rotationally symmetrical. In addition, H field distribution varies with frequency. It is impossible to have constant corrector factors in the FDTD updating equation, as well as constant surface impedance of the conductor.

To construct a thin wire model with non-circular cross section in a coarse FDTD mesh, the correction factors of E field and H field in four orthogonal directions and the conductor loss need to be considered separately in the FDTD initialization process. The E field correction factors are frequency-invariant, and can be adopted in the updating equations similar to the conventional thin wire model technique. The H field correction factors and conductor loss are frequency variant. Their frequency responses are obtained numerically and are approximated by rational functions with the vector fitting technique [91] in the initialization process. They are incorporated in the updating equation using an iterative convolution technique.

In a long conductor, the transverse dimension of the conductor is much less than its longitudinal dimension. Therefore, the charge and current densities, as well as electric and magnetic field around the conductor, are determined by 2D procedures, i.e., 2D surface charge simulation method and 2D equivalent circuit method. These procedures are executed one time in the initialization stage for one conductor type. Once the execution is completed, the FDTD method can proceed without extra calculation. Without losing generality, a z-oriented thin wire model is present in the following sections.

5.2.1 E field correction factors

Under quasi-static conditions, electric charge is situated on the surface of a conductor and is independent of frequency and conductivity. A surface charge simulation method is then applied to determine the surface charge of the conductor, subsequently the E field distribution around the conductor. Fig.2 shows the cross section of an arbitrary conductor. Its boundary carries surface electric charge, and is divided into N line segments, as shown in Fig. 5.2(a). The charge density in each segment is constant.

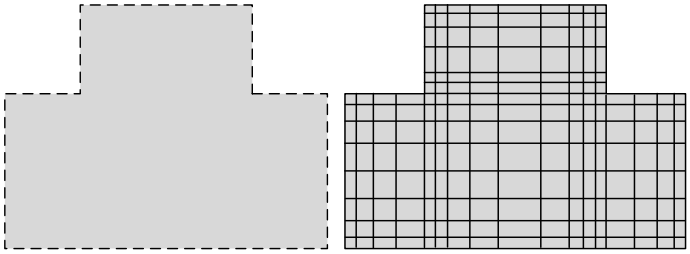

(a) Boundary meshing (b) Meshing of cross section area

Figure 5.2 Discretization of conductor cross section

Assume charge q_j situates on line segment L_j. With an arbitrary reference point located far away (its radial distance is much greater than wire cross-sectional dimensions), electric potential ϕ_i on the center of line segment L_i is calculated, as follow:

$$\phi_i = \sum_{j=1}^{N} \frac{q_j}{2\pi\varepsilon L_j} \int_{L_i} \int_{L_j} \ln \frac{1}{\rho_{i,j}} dl_i dl_j = \sum_{j=1}^{N} D_{ij} q_j \tag{5.3}$$

where $\rho_{i,j}$ is the distance between the point in the source segment and the middle point of the observation segment. Although the integrand is singular, the integral is convergent [92]. A technique in [93] was adopted to remove the singularity in

the integral. A matrix equation for potential vector $\boldsymbol{\phi}$ and charge vector $\mathbf{Q}$ on the boundary is established, as follows:

$$\begin{aligned} \boldsymbol{\phi} &= \mathbf{D} \cdot \mathbf{Q} \quad \text{or} \\ \mathbf{Q} &= \mathbf{D}^{-1} \cdot \boldsymbol{\phi} \end{aligned} \tag{5.4}$$

where $\mathbf{D} = \{D_{ij}\}$. Note that the potential is the same everywhere on the cross section. The following relationship between total charge q_0 on the boundary and conductor potential ϕ_0 is obtained, as follows:

$$q_0 = F_{sum}\phi_0 \,. \tag{5.5}$$

where F_{sum} is the summation of all elements in matrix $\mathbf{D^{-1}}$. Substituting (5.5) into (5.4), charge distribution along the boundary can be expressed in terms of total charge q_0, as follows:

$$\mathbf{Q} = \mathbf{D}^{-1} \cdot \mathbf{U} / F_{sum} \cdot q_0 \,, \tag{5.6}$$

where $\mathbf{U}$ is a unit vector with the dimensions of $N \times \mathbf{1}$**.** With charge distribution on the boundary, the electric field around the conductor is evaluated with the Coulomb's law, as follows:

$$\begin{aligned} Ex &= \sum_{j=1}^{N} \frac{q_j}{2\pi\varepsilon L_j} \int_{L_j} \frac{x_j - x_k}{\rho_{j,k}^2} dl \\ Ey &= \sum_{j=1}^{N} \frac{q_j}{2\pi\varepsilon L_j} \int_{L_j} \frac{y_j - y_k}{\rho_{j,k}^2} dl \end{aligned} \,, \tag{5.7}$$

Both line and surface averaged electric fields of a conductor can be then estimated, subsequently the correction factors of E field in the four orthogonal directions. Note that both line and surface averaged electric fields are proportional to total charge q_0. This parameter is cancelled out in the evaluation of the

correction factors. Therefore, the correction factors are not affected by the frequency of conductor current and total charge on the conductor. They are determined by the conductor geometry and cell size only. The modified E field correction factors are implemented directly in the FDTD updating equations.

5.2.2 H field correction factors

In a circular conductor with radius a, current density $J(r)$ on its cross section is calculated analytically by [94]

$$J(r) = \frac{j\omega}{2\pi\sqrt{j\omega\sigma_c\mu_c}\cdot a}\frac{I_0(\sqrt{j\omega\sigma_c\mu_c}\cdot r)}{I_1(\sqrt{j\omega\sigma_c\mu_c}\cdot a)} \tag{5.8}$$

where σ_c and μ_c are the conductivity and permeability of the conductor respectively.

However, no analytical formula could be possibly derived in case of conductors with arbitrary cross section. In this case, a numerical procedure based on the 2D equivalent circuit method (ECM) is applied. Consider a nonmagnetic conductor and divide it into M small rectangular elements on its cross section, as shown in Fig. 5.2(b) (the formulation of magnetic conductors is given in the Appendix). Current density in each element is constant. Under the quasi-static conditions, each element is represented with circuit components: resistance and inductance. With the relationship of electric potential ϕ and magnetic potential A on the conductor, $-\nabla\phi = J/\sigma + j\omega A$, a system of equations in the frequency domain can be established,

$$\begin{aligned} &\mathbf{V} = \mathbf{IR} + j\omega\mathbf{LI} = \mathbf{ZI} \quad \text{or} \\ &\mathbf{I} = \mathbf{Z}^{-1}\mathbf{V} \end{aligned} \tag{5.9}$$

where **V** is the potential difference (voltage) vector at the center of elements for a unit length and I is the current vector for these elements, In (9) the elements $R_{i,i}$ and $L_{i,j}$ of both resistance and inductance matrices are given by

$$\begin{aligned} R_{i,i} &= 1/(\sigma \Delta s_i) \\ L_{i,j} &= j\omega \frac{\mu_0}{2\pi \Delta s_j} \int_{\Delta S_j} \ln \frac{1}{\rho_{i,j}} ds_j \end{aligned}, \tag{5.10}$$

where Δs_j is the area of the jth element. The similar technique used for (5.3) is applied to deal with the singularity in the integral.

As the voltage of these elements is identical, the total current can be expressed using this voltage denoted by V_0, as follows:

$$I_{total} = Y_{sum} \cdot V_0 . \tag{5.11}$$

where Y_{sum} is the summation of all elements in matrix $\mathbf{Z^{-1}}$. Substituting (5.11) into (5.9) yields

$$\mathbf{I} = \mathbf{Z}^{-1} / Y_{sum} \cdot I_{total} = \mathbf{P} \cdot I_{total} . \tag{5.12}$$

Once the current distribution on the conductor is given, H field around the conductor is evaluated with the Biot-Savart law, as follows:

$$\begin{aligned} Hx(\omega) &= \sum_{j=1}^{M} \frac{I_j(\omega)}{2\pi \Delta s_j} \iint_{\Delta S_j} \frac{y_j - y_k}{\rho_{j,k}^2} dxdy \\ Hy(\omega) &= \sum_{j=1}^{M} \frac{I_j(\omega)}{2\pi \Delta s_j} \iint_{\Delta S_j} \frac{x_j - x_k}{\rho_{j,k}^2} dxdy \end{aligned}, \tag{5.13}$$

Then the H field correction factors in the four orthogonal directions can be estimated. Note that both line and surface averaged magnetic fields are proportional to total current I_{total}. The correction factors of H field are independent

of conductor current. However, it varies with current frequency due to the skin effect, and cannot be used directly in the line/surface averaged-field transformation. A time-domain correction factor would be necessary in the simulation. The VFT [91] is then applied to approximate the inverse of a correction factor with a rational function in *s* domain, as follows:

$$\mu^{\#}(s) = \frac{1}{\mu(s)} \approx d + sh + \sum_{m=1}^{N} \frac{r_m}{s - a_m} . \tag{5.14}$$

where a_m are poles and r_m are residues. After d, h, r_m and a_m are identified, time-domain response $\mu^{\#}(t)$ is obtained directly from the rational function in (5.14). The surface averaged field can be then transformed to line averaged field in an iterative convolution process. Now (5.2b) in the time domain is expressed as,

$$\langle Hx \rangle_x = \langle\langle Hx \rangle\rangle_{yz} * \mu^{\#} . \tag{5.15}$$

The updating equation (5.15) can be expanded as

$$\langle Hx \rangle_x^q = K_p \langle\langle Hx \rangle\rangle_{yz}^q + K_n \langle\langle Hx \rangle\rangle_{yz}^{q-1} + \sum_{m=1}^{N} \varphi_m^q , \tag{5.16}$$

where $K_p = d + h/\Delta t$ and $K_n = -h/\Delta t$.

The convolutional term on the right hand side of (5.16) is updated as

$$\varphi_m^q = \frac{r_m}{a_m}\left(e^{a_m \Delta t} - 1\right) \cdot \langle\langle Hx \rangle\rangle_{yz}^q + e^{a_m \Delta t} \cdot \varphi_m^{q-1} , \tag{5.17}$$

5.2.3 Factor for the conductor loss

It is known that surface electric field of a lossy conductor in its longitudinal direction is nonzero, and has to be included in the updating equations. Note that surface E-field varies along the wire boundary. Four separated E field components

are adopted to represent the lossy conductor in four associated cells. Taking a conductor with a rectangular cross section as an example, surface E field components Er1, Er2, Er3 and Er4 on the conductor shown in Fig. 5.3 are used in the updating equations.

These separated E field components are determined using the equivalent circuit method presented early. They are expressed by the total current in the frequency domain as,

$$Er_i = I_i \cdot R_{i,i} = T_i \cdot I_{total}\,, \tag{5.18}$$

where $T_i = P_i \cdot R_{i,i}$. As coefficient T_i is frequency dependent, the VFT is applied again to generate four rational functions in s domain, similar to (5.14). Time-domain response $T(t)_i$ are obtained directly from these rational functions in the initialization stage. Four separated E field components are then updated in an iterative convolution process in the FDTD updating period. The total conductor current of each FDTD element is obtained by integrating H field components at the previous time step in a contour path enclosing the conductor in the FDTD region, as follows:

$$\begin{aligned} I_{total}^{q}(p+1/2) \approx I_{total}^{q-1/2}(p+1/2) = \Delta x \cdot \left[Hx^{q-1/2}(m, n+1/2, p+1/2) - Hx^{q-1/2}(m, n-1/2, p+1/2) \right] \\ + \Delta y \cdot \left[Hy^{q-1/2}(m+1/2, n, p+1/2) - Hy^{q-1/2}(m-1/2, n, p+1/2) \right] \end{aligned}. \tag{5.19}$$

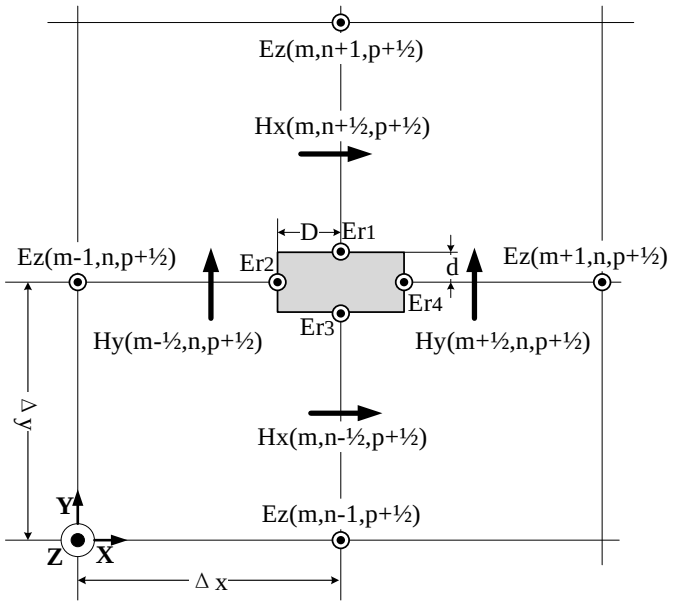

(a) x-y plan view

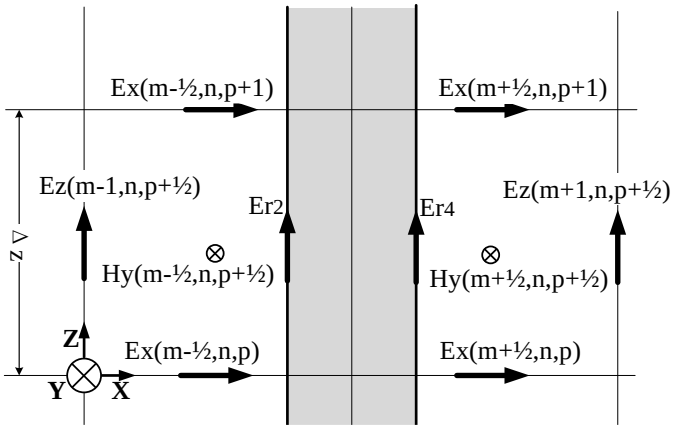

(b) x-z plan view

Figure 5.3 Thin wire and its adjacent electric and magnetic fields

H field components in the vicinity of the conductor are updated at next half time step with separated E field components. By taking Hy(m-1/2,n,p+1/2) as an example, the equation of surface averaged H field is shown as

$$\left\langle H_y^{q+1/2}(m-1/2,n,p+1/2)\right\rangle_y = \left\langle H_y^{q-1/2}(m-1/2,n,p+1/2)\right\rangle_y$$
$$-\frac{\Delta t}{\mu\Delta z}\cdot\left[E_x^q(m-1/2,n,p+1)-E_x^q(m-1/2,n,p)\right]+\frac{\Delta t}{\mu(\Delta x-D)}\cdot\left[E_{r2}^q(p+1/2)-E_z^q(m-1,n,p+1/2)\right]$$

(5.20)

5.2.4 Flow chart of the proposed model

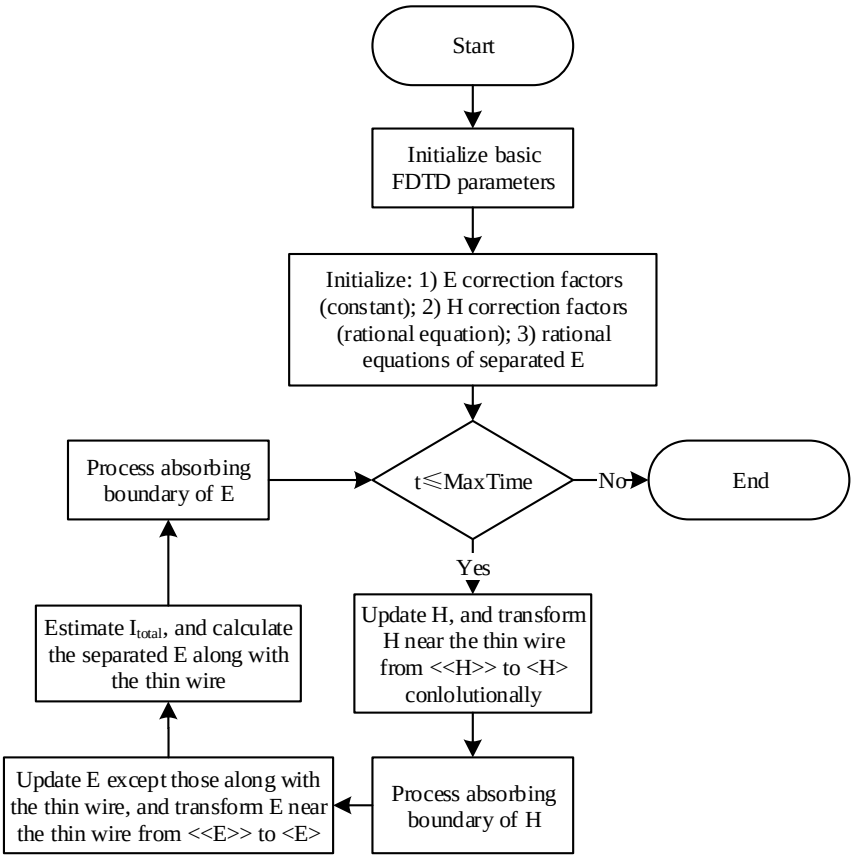

Figure 5.4 Flow chart of the proposed thin wire model calculation with the absorbing boundary condition

The complete procedure of the proposed thin wire model with the absorbing boundary condition (ABC) is shown in Fig. 5.4. There are two constraints of conductor zone meshing when applying this proposed method: 1) one longitudinal edge of the FDTD mesh should run through the conductor body; 2) the conductor cross section should be within the effective region of its longitudinal E fields. The effective region of the Ez(m,n,p+1/2) in the x-y plan (see Fig. 5.2 (a)), for example, is defined as

$$(m-1/2)\cdot\Delta x < x < (m+1/2)\cdot\Delta x,$$
$$(n-1/2)\cdot\Delta y < y < (n+1/2)\cdot\Delta y. \tag{5.21}$$

These requirements can be easily fulfilled in the FDTD meshing process.

5.3 Validations

The proposed thin wire model has been applied to analyze surge propagation on lossy wire structures with non-circular cross section. For validation, the results were compared with those obtained with analytical and numerical approaches.

5.3.1 Analytical validation for symmetrical cross section

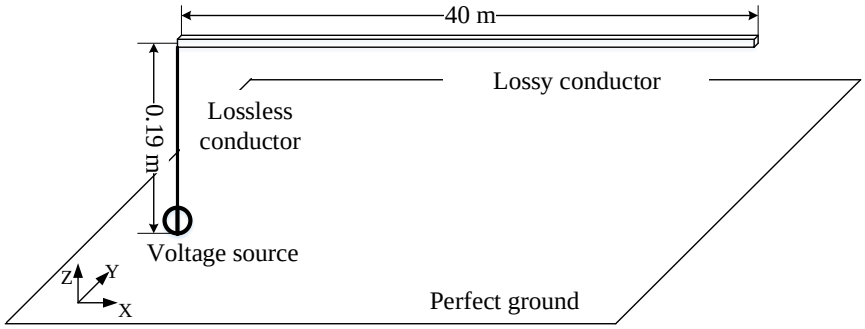

Figure 5.5 Configuration of the analytical validation arrangement

A horizontal conductor is arranged above a perfect ground for analytical validation as shown in Fig. 5.5. Three shapes of conductor cross section are selected in the test, i.e., rectangular, H and cross shapes, as shown in Fig. 5.6. The rectangular conductor is made of linear magnetic material. Its relative permeability and conductivity are respectively set to be 100 and $1 \times 10^6\ S/m$. Other shape conductors are made of non-magnetic material with the conductivity of $1 \times 10^5\ S/m$ to signify the effect of frequency-dependent losses on a short line. In testing, one terminal of the conductor is connected to the ground via a vertical

lossless wire and a voltage source, and the other terminal is left open. The voltage source generates a sinusoidal waveform with amplitude V_0 at the frequencies of 50 MHz and 150 MHz. The length and height of the conductor are 40 m and 0.19 m. Voltage is measured at 4 m, 8 m, 12 m, 16 m and 20 m along the non-magnetic conductor and 2 m, 4m, 6m and 8m along the magnetic conductor, before the reflected wave arrives.

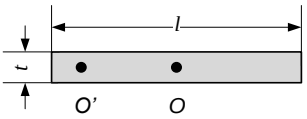

(a) Rectangular shape

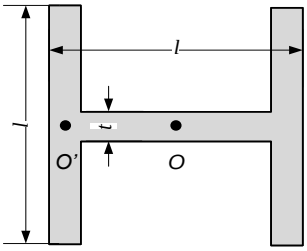

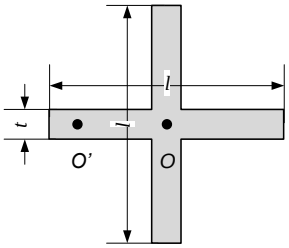

(b) H shape (c) Cross shape

Figure 5.6 Configurations of three cross section shapes (t=0.5mm, l=3mm)

Wave propagation over the tested conductor can be analyzed analytically with the transmission line theory (TLT) [85]. The peak voltage between the conductor and the PEC ground with no reflected wave at angular frequency ω is given by,

$$V(x,t) = V_0 e^{-\alpha x} \sin(\omega t - \beta x). \tag{5.22}$$

where parameters α and β are expressed with frequency-dependent L and R, and frequency-independent C as,

$$\alpha = \sqrt{[(\omega^2 LC)^2 + (\omega RC)^2]^{1/2} - \omega^2 LC} \Big/ \sqrt{2}$$
$$\beta = \sqrt{[(\omega^2 LC)^2 + (\omega RC)^2]^{1/2} + \omega^2 LC} \Big/ \sqrt{2}$$

Note that it is difficult to determine L, R and C of a non-circular conductor by analytical formulas. Actually, these parameters are calculated numerically with the boundary element method (L and R) and the finite element method (C) at selected frequencies, as shown in Table 5.1.

Table 5.1 R and C of three conductor shapes calculated by the boundary element method and the finite element method

Type	Freq./MHz	L/μH	R/ohm	C/pF
Rectangular shape	50	5.072	42.80	9.321
	150	4.952	76.45	
H shape	50	1.097	5.930	10.30
	150	1.091	9.655	
Cross shape	50	1.161	8.385	9.773
	150	1.153	13.33	

In the FDTD simulation with the proposed thin wire model, the working volume is set to 40.5 m × 0.4 m × 0.4 m. The 7-layer PML absorbing boundary condition is adopted to absorb unwanted reflections. A uniform mesh scheme is adopted with the cell size of 0.01m. To test the accuracy of different geometrical arrangements, one longitudinal edge of the FDTD mesh runs at the center (O) or the biased location (O') within the cross section as shown in Fig. 5.6. The time step is set to

0.8 times of the maximum Courant-Friedrich-Levy (CFL) time step to maintain the simulation stability. In the initialization process of the proposed method, the conductor is discretized into 2D cells with the size of less than one-tenth of its skin depth to determine its current density. The investigated frequency range of the current density distribution is from DC to 1 GHz. The fourth order VFT is used to approximate the frequency responses of both the H correction factors and the separated longitudinal E field components. The relative error of the frequency approximation is lower than 0.1%.

Table 5.2 Voltage amplitude of a rectangular conductor calculated by the proposed thin wire model and TLT (Sig=1e6 S/m, μr=100)

Freq.	Method	Voltage/V				Averaged error
		x=2	x=4	x=6	x=8	
Grid line at the position O						
50MHz	Proposed	973.9	914.4	863.2	812.3	0.29%
	TLT	971.4	916.6	864.9	816.2	
150MHz	Proposed	949.9	847.2	761.3	680.1	0.95%
	TLT	948.9	854.4	769.3	692.6	
Grid line at the biased position O’						
50MHz	Proposed	973.4	913.3	862.2	813.0	0.32%
	TLT	971.4	916.6	865.0	816.2	

Table 5.3 Voltage amplitude of a H-shape conductor calculated by the proposed thin wire model and TLT (Sig=1e5 S/m, μr=1)

Freq.	Method	Voltage/V				Averaged error
		x=8	x=12	x=16	x=20	
Grid line at the position O						
50MHz	Proposed	968.2	935.5	905.0	875.0	0.62%
	TLT	964.3	929.9	896.7	864.7	
150MHz	Proposed	948.9	899.7	853.8	806.4	1.24%
	TLT	942.4	888.2	836.9	788.8	
Grid line at the biased position O'						
50MHz	Proposed	940.8	884.1	831.7	792.9	0.35%
	TLT	942.4	888.2	837.0	788.8	

The voltage amplitudes at several points calculated by both the proposed thin wire model and TLT are shown in Tables 5.2, 5.3 and 5.4. The voltages at $x = 1$ m and $x = 4$ m are set as the reference (1kV) for the rectangular-shape conductor and other conductors, respectively. It is found that the proposed thin wire model matches the analytical result well with the averaged relative error of 0.54%. These tables also show the results when one longitudinal edge at the biased location (O'). No significant difference is found. This indicates the proposed method is rigid, and is insensitive to the selection of the local center of the conductor in FDTD meshing.

Table 5.4 Voltage amplitude of a cross-shaped conductor calculated by the proposed thin wire model and TLT (Sig=1e5 S/m, μr=1)

Freq.	Method	Voltage/V				Averaged error
		x=8	x=12	x=16	x=20	
Grid line at the position O						
50MHz	Proposed	952.9	907.1	864.2	822.4	0.03%
	TLT	952.5	907.2	864.1	823.1	
150MHz	Proposed	922.2	852.1	783.4	724.3	0.62%
	TLT	925.3	856.1	792.2	733.1	
Grid line at the biased position O’						
50MHz	Proposed	928.2	860.5	798.6	737.6	0.45%
	TLT	925.3	856.2	792.3	733.1	

Table 5.5 TLT parameters of each type of thin wire models with asymmetrical cross sections

Type	Freq/MHz	L/uH	R/ohm	C/pF
L shape	10	1.0165	4.3105	11.2860
	20	1.0105	5.0650	
T shape	10	1.0325	4.5790	11.1788
	20	1.0230	5.5650	
U shape	10	0.9770	2.9755	11.6970
	20	0.9725	3.6305	

5.3.2 Analytical validation for asymmetrical cross section

Three types of asymmetrical cross section shapes will be tested, including L shape, T shape and U shape, as shown in Fig. 5.7. Three scenarios are considered: 1) the FDTD grid line (E field components in longitudinal direction) passes through the cross section center O, and edges of cross section center in parallel with Cartesian axes; 2) the FDTD grid line passes through the biased center O' , and edges of cross section center in parallel with Cartesian axes; 3) the FDTD grid line passes through the cross section center O, and the cross section rotated with a certain angle.

The configuration of validation cases is shown in Fig. 5.8. A lossy thin wire structure is arranged 0.1 m above a perfect electrical conductor (PEC) ground. The conductivity, relative permittivity and relative permeability are 1e5 S/m, 1 and 1. One of the terminals are opened, the other terminal is connected to the ground via an ideal current source and a lossless thin wire. The current source generates 10 MHz or 20 MHz sinusoidal waveform to test the model accuracy under different frequency. The length of the thin wire model is 120 m. Five current sensors are defined on the wire structure. They are located 5 m, 10 m, 20 m, 30 m, 40 m away from the grounded terminal.

The capacitance, inductance and resistance of the TLT equation are obtained numerically with "ANSYS" software package (C) and "OERSTED" software (L and R). These TLT parameters of thin wire models with cross sections of L shape,

T shape and U shape are listed in Table 5.5.

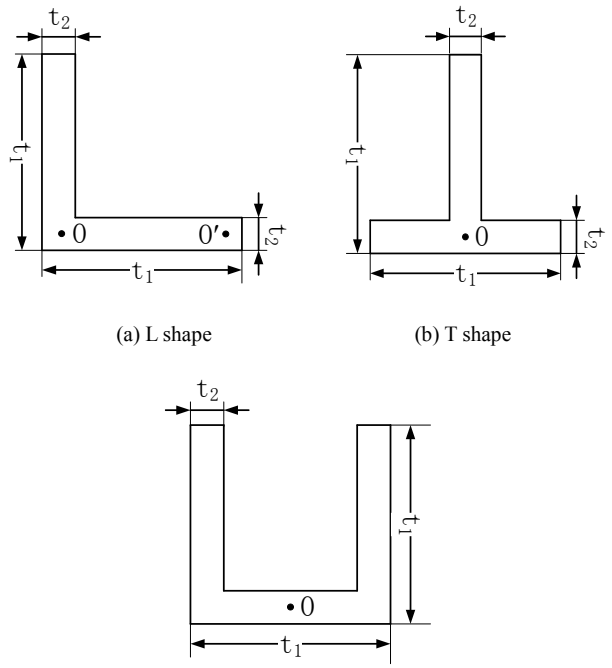

Figure 5.7 Three types of asymmetrical cross sections (t1=3mm, t2=0.5mm)

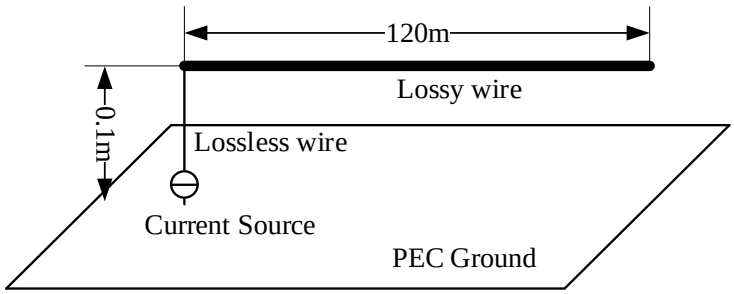

Figure 5.8 The configuration of validation cases with asymmetrical cross sections

For the FDTD method, uniform mesh technique is adopted, and the cell size is defined as 2 cm. The computation region is defined as $6060 \times 60 \times 40$. The bottom boundary is left as PEC condition, and the other boundaries are assigned as perfectly matched layer (PML) absorbing condition to absorb unwanted wave reflection. The Courant Friedrichs Lewy (CFL) limit is reduced with multiplying

a factor of 0.8 to maintain computation stability. The current measured at 5 m on the lossy wire from the grounded terminal is set as a reference (1A).

Table 5.6 Current amplitudes of thin wire models with asymmetrical cross section. The FDTD grid line at the position O

Freq/MHz	Method	Length			
		10m	20m	30m	40m
L shape cross section, and grid line at the position O					
10	Prop.	0.9643	0.8977	0.8340	0.7753
	TLT	0.9647	0.8979	0.8357	0.7778
20	Prop.	0.9570	0.8763	0.8026	0.7365
	TLT	0.9586	0.8808	0.8093	0.7437
T shape cross section, and grid line at the position O					
10	Prop.	0.9639	0.8968	0.8326	0.7734
	TLT	0.9630	0.8932	0.8284	0.7683
20	Prop.	0.9538	0.8675	0.7890	0.7193
	TLT	0.9551	0.8712	0.7946	0.7248
U shape cross section, and grid line at the position O					
10	Prop.	0.9736	0.9237	0.8745	0.8283
	TLT	0.9746	0.9257	0.8793	0.8351
20	Prop.	0.9688	0.9093	0.8536	0.8029
	TLT	0.9690	0.9099	0.8544	0.8023

Table 5.7 Current amplitudes of thin wire models with L-shape cross section. The FDTD grid line at the biased position O'

Freq/MHz	Method	Length			
		10m	20m	30m	40m
10	Prop.	0.9658	0.9020	0.8405	0.7837
	TLT	0.9647	0.8979	0.8357	0.7778
20	Prop.	0.9584	0.8803	0.8087	0.7444
	TLT	0.9586	0.8808	0.8093	0.7437

Table 5.8 Current amplitudes of thin wire models with L-shape cross section rotated 30° clockwise, FDTD grid line at the position O

Freq/MHz	Method	Length			
		10m	20m	30m	40m
10	Prop.	0.9621	0.8906	0.8246	0.7635
	TLT	0.9647	0.8977	0.8354	0.7774
20	Prop.	0.9567	0.8759	0.8019	0.7365
	TLT	0.9585	0.8805	0.8089	0.7431

The current amplitudes of thin wire models with three types of asymmetrical cross sections calculated by the proposed thin wire model and TLT are listed in Table 5.6. The FDTD grid line passes through the conductor cross section at the position O. The averaged relative error of three conductor types is 0.36%. The

maximum and minimum relative errors are 0.96% and 0.02%. The current amplitudes obtained from two numerical methods match well. The case that the FDTD grid line passes through the biased position O' is investigated in L shaped conductor, and simulation results are shown in Table 5.7. The averaged, maximum and minimum relative errors are 0.27%, 0.76% and 0.02%. According to the simulation results, the proposed thin wire model can simulate thin wire structures with asymmetrical cross sections well. The FDTD grid line can pass through an arbitrary position on the conductor cross section.

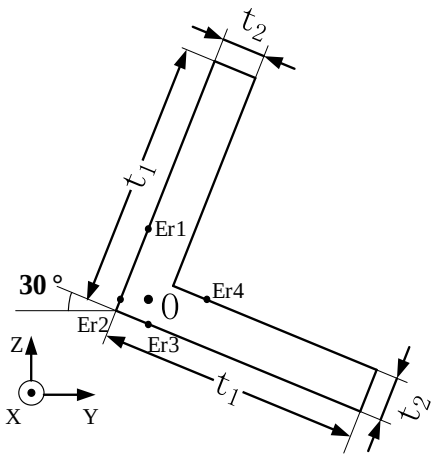

Figure 5.9 The L-shape cross section with a 30° rotation clockwise

The L-shaped cross section rotated 30° clockwise, and the FDTD grid line passes through the position O, as shown in Fig. 5.9. Two comparisons between original frequency dependent parameters and frequency characteristics fitted by vector fitting techniques are shown in Fig. 5.10. The current amplitudes of thin wire models with a rotated cross section are listed in Table 5.8. In this case, the correction factors of material parameters are extremely imbalanced. To obtain a

stable result, the time step is multiplied with a factor of 0.5. The averaged, maximum and minimum relative errors are 0.82%, 1.79% and 0.18%. This indicates that the proposed thin wire model can simulate the rotated thin wire structures with reasonable accuracy.

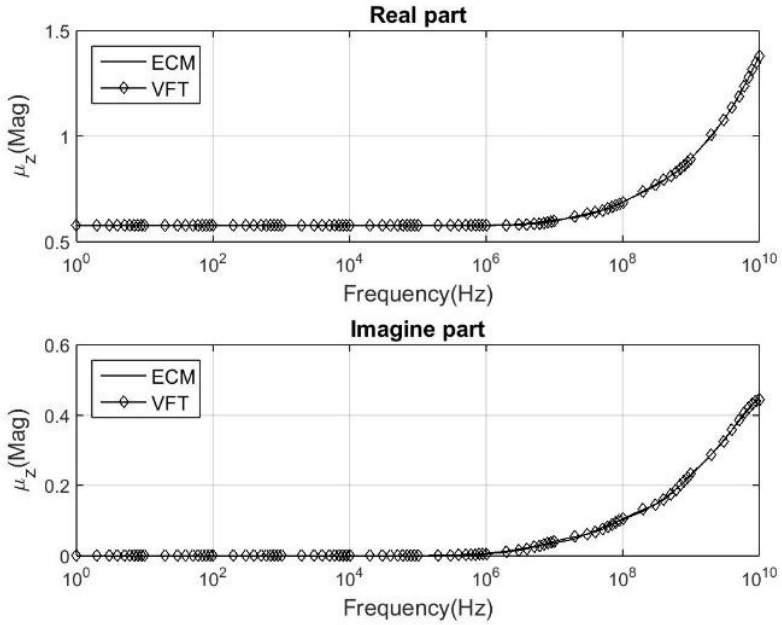

(a) The correction factor of Hy in the positive z direction

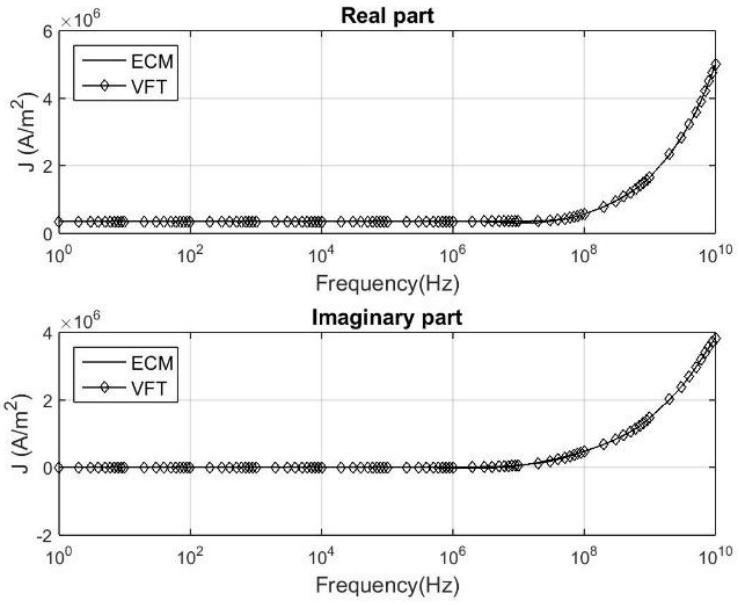

(b) The normalized current density at the position Er1

Figure 5.10 Comparisons between original and fitted frequency characteristics of a rotated L-shaped conductor

5.3.3 Numerical validation

The numerical validation has been also performed for comparing transient waveforms of the surge on a wire structure. The conventional FDTD method was employed for comparison. Fig. 5.11 shows the configuration of the tested system, which is constructed by a central-fed conductor with a rectangular cross section in free space. Two conductor arms having the dimensions of $2\ \mathrm{m} \times 3\ \mathrm{mm} \times 0.5\ \mathrm{mm}$ are connected to a hard voltage source. The voltage source generates a 1 V Gaussian pulse waveform ($\sigma = 1.5 \times 10^{-9}, \mu = 5 \times 10^{-9}$). The working volume for the central-fed conductor is $5\ \mathrm{m} \times 0.5\ \mathrm{m} \times 0.5\ \mathrm{m}$. The conductors have the conductivity and relative permittivity of $5.96 \times 10^5\ \mathrm{S/m}$ and 1.

Table 5.9 Meshing schemes for the central-fed conductor used by the proposed thin wire model and traditional FDTD method

Methods	Mesh sizes	
	Longitudinal size	Transverse size
Proposed	10 mm	FDTD: 10 mm × 10 mm ECM: from 1 μm to 20 μm
Traditional	10 mm	FDTD: from 10 μm to 10 mm

The PML absorbing boundary condition was applied to absorb unwanted reflection in all cases. An extremely fine meshing scheme was adopted in the

conventional FDTD method. The mesh sizes adopted in these two methods are given in Table 5.9. The time step in the proposed case was set to 0.8 of its maximum CFL time step. No instability problem was encountered after 6.4×10^4 time steps.

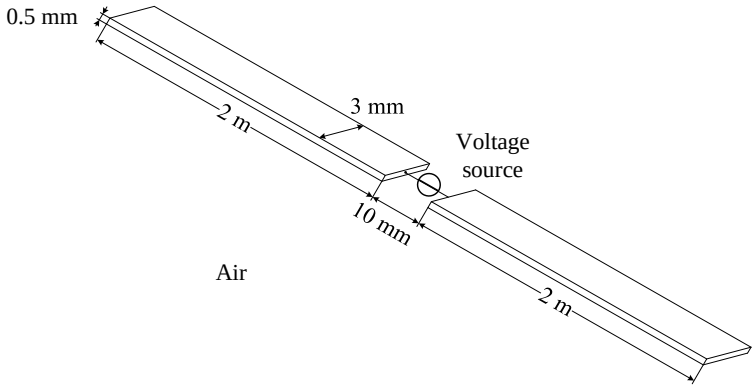

Figure 5.11 Configurations of the central-fed conductor

Fig. 5.12 shows the original frequency characteristics and fitted characteristics of one Hy correction factor and normalized current density at the position of Er4 shown in Fig. 5.3(a). With the 4th order rational-function approximation, good agreements are observed between the original and fitted results.

Fig. 5.13 shows the simulation results of the pulse current at the feeding point of a central-fed conductor obtained with the conventional FDTD method and proposed thin wire model. It is found that the current waveforms of the proposed model match well in both amplitude and waveform. The error at the wave crest is less than 5%. This indicates that the proposed thin wire model can mimic a lossy conductor with non-circular cross section without compromising result accuracy. The computational resources required by these two methods are compared by

performing the simulation on the same personal computer with a graphics processing unit (NVIDIA® Tesla™ K40C GPU Computing Accelerator). The traditional method consumed 3 GB memory space and ran 49 hours. While, the proposed method consumed 0.9 GB memory space and ran only 25 minutes. Both the computational resources and simulation time are significantly reduced with the proposed thin wire model.

The errors of the pulse currents may be caused by the meshing scheme adopted in the conventional FDTD method. Note that the mesh sizes are not less than 1/2 of the skin depth. In order to obtain more accurate results, much finer meshing is required in the conventional method. However, this will require unacceptable computation resources in the simulation.

5.4 Transient analysis in a light rail system

The proposed thin wire model has been applied to evaluate lightning transients in a point controller (PC) of the light rail system under a direct lightning stroke. Fig. 5.10 shows a representative configuration of the railway system of concern. Electric trains are powered by an overhead line (OHL) system at +750 VDC. The OHL system is comprised of contact wires (CW), messenger wire (MW), fault current return wire (FCRW), insulators, lightning arresters (LA), poles and other accessories. It is fed from a rectifier substation (RS) via traction power cables (TPS) and traction return cable (TRP), as seen in Fig. 5.14. The poles are located

separately every 25 m, and are provided with 1 m deep reinforced concrete foundation at each location. The rails have a typical non-circular cross section, as shown in Fig. 5.15, and are positioned at a height of 0.4 m above the ground level. The FCRW is hinged 5.2 m above the ground, and is bonded to every pole along the track, and to the rails via diodes.

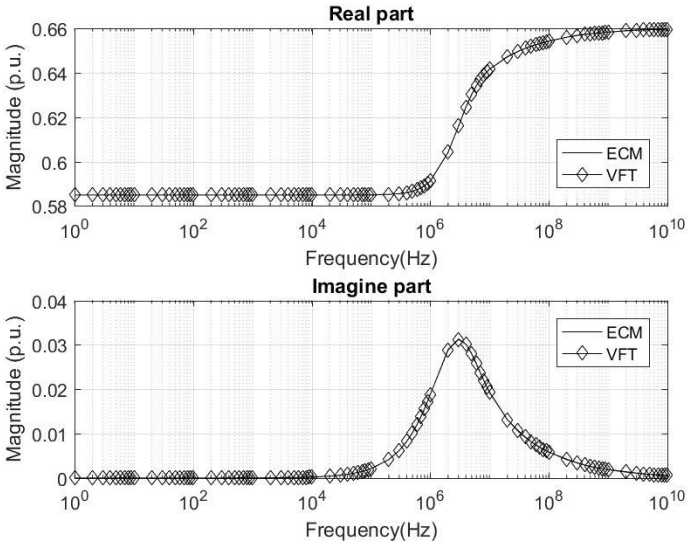

(a) The correction factor of Hy in the positive x direction

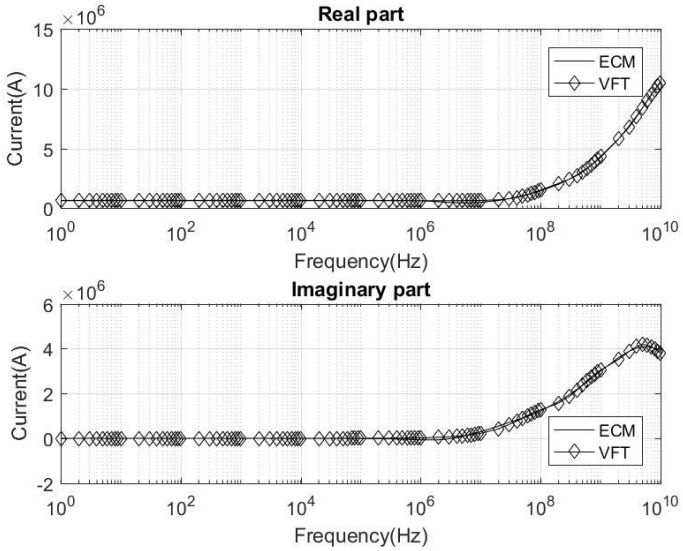

(b) Normalized current density in the positive x direction

Figure 5.12 Comparison between original and fitted frequency characteristics of a rectangular-shaped conductor

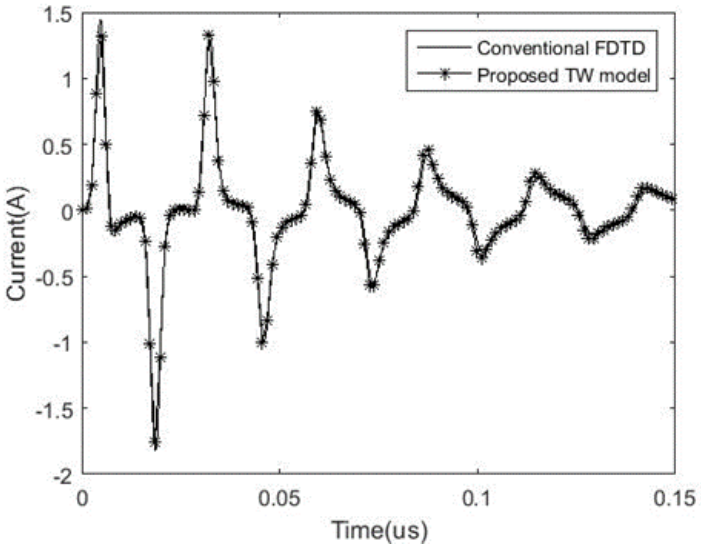

Figure 5.13 Pulse current in the central-fed conductor calculated with two methods

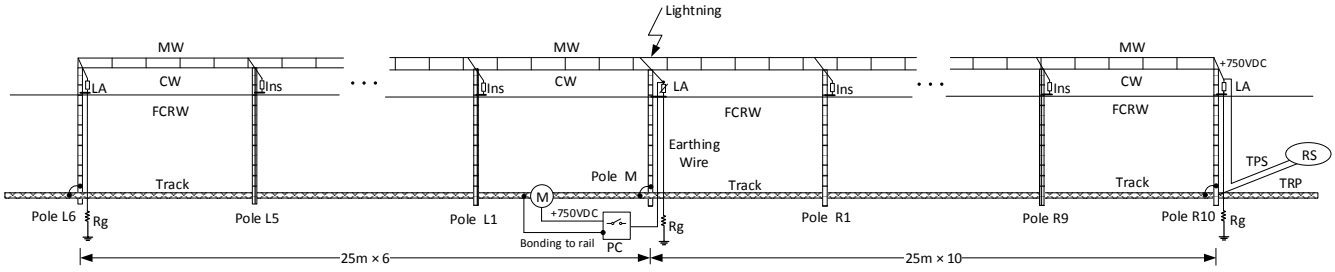

Figure 5.14 Configuration of the light rail system

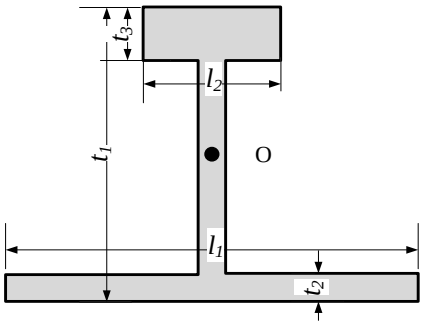

Figure 5.15 The configuration of the rail track cross section (l1=150mm, l2=75mm,

t1=175mm, t2=15mm, t3=35mm

The trackside PC is supplied at +750VDC via a power cable connected to CW/MW at pole M. The PC is located 6.3 m away from pole M. The cable runs

on the ground level to a miniature circuit breaker (MCB) installed inside the PC cabinet, and goes further to a trackside motor (e.g. Point Machine) for track movement. The PC cabinet is bonded to the rail 6.27 m away. The cabinet and all the connecting wires are placed on the ground. Lightning arresters (LA) are provided at pole L1, M and R10 to protect traction feeder cables and other equipment connected to the overhead line. They are grounded via insulated conductors to local grounding electrodes.

The rail is presented by a linear magnetic conductor and is simulated by the proposed thin wire model. Its conductivity and relative permittivity are respectively equal to 1e6 S/m and 100. In the initialization stage, the cross section of the rail, as shown in Fig. 5.15, is divided into 6765 non-uniform cells for analyzing the frequency dependent current distribution from DC to 10 MHz. The 6^{th} order VFT is then applied to obtain H field correction factors and factors for calculating surface E field components. The perimeter of the cross section is divided into 795 sections to derive the E field correction factors by the surface charge simulation method.

As CW and MW are electrically connected at a regular interval, they are modeled as a wire conductor situated at the height of 5.6 m above track rail. Those wires are supported and registered on hinged cantilever assemblies to poles with insulators. The traditional thin wire model [52] is applied to mimic these wires as well as FCRW. The insulators on other poles are simulated as breakdown models.

The insulating level of the insulators is 30 kV. Considering the volt-time flashover curve, the breakdown voltage is defined as 1.5 times of the insulating level [95], i.e. 45 kV. The LAs are modeled as active current sources by piecewise linear method [96]. The residual voltage is set as 3.9 kV. The lightning return stroke is represented by a hard current source connected to the CW/FW on the top of pole M. It generates an $4/10\ \mu s$ impulse current with $50\ kA$ amplitude according to EN50124-2.

The working domain of the problem is divided into $375\times160\times110$ cells. Both the OHLs and rails run continuously to the domain boundary at their two ends. Six planes of PML absorbing boundary condition are adopted to absorb unwanted reflection at its boundary. The non-uniform mesh technique is adopted. The cell sizes are 0.05 m and 0.2 m near the mast and rail track, and increase to 25 m gradually. The soil conductivity is 0.01 S/m, and relative permittivity is 4. The time step is determined by the minimum cell size, i.e. 9.6225e-11 s.

It was reported that arcing marks were found in the power supply compartment of some PCs in a light railway system. In the simulation both current on the rail and voltage between the busbars and the PC enclosure were then examined. Fig. 5.16 shows the current on the rails at pole M. Its waveform is similar to the lightning current. The maximum current amplitude is 17.21 kA. A substantial amount of lighting current is discharged via the rails. Fig. 5.17 shows the transient voltage between the busbars and the PC enclosure. A transient stage containing

high frequency oscillation is observed at the initial part of the curve. The amplitude and frequency are mainly affected by the slope of the lightning current waveform, frequency dependent characteristics of the track and reflections within the power cable. The voltage waveform tends to zero as the lightning current decreases. The oscillation appears at the initial part of induced voltage is caused by wave propagation and reflection between the PC terminal and the earthing wire terminal of the LA on pole M.

According to the simulation result, it is found that flashover likely occurs under a direct lightning stroke during the rising stage of the lightning waveform inside the PC cabinet. Extra protection schemes should be considered to avoid lightning flashover within the cabinet.

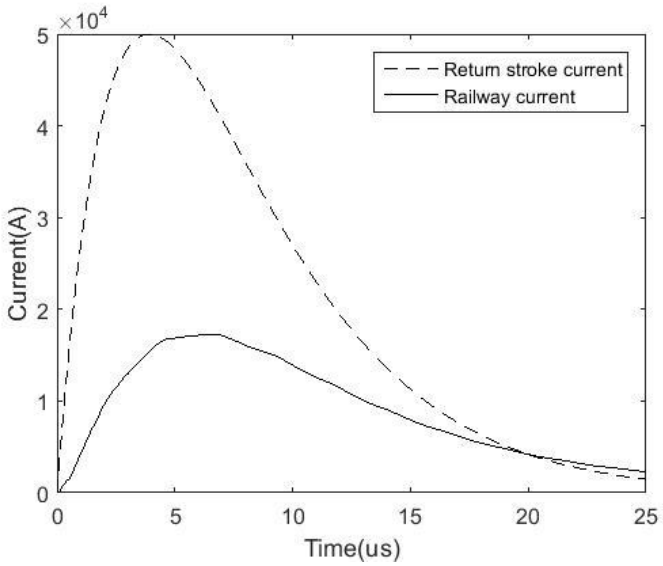

Figure 5.16 Lightning return stroke current and rail current at pole M

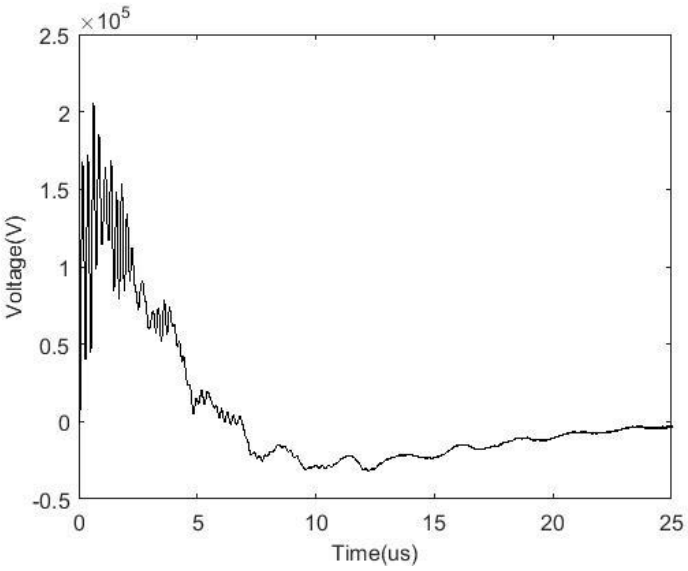

Figure 5.17 Lightning voltage at the PC cabinet

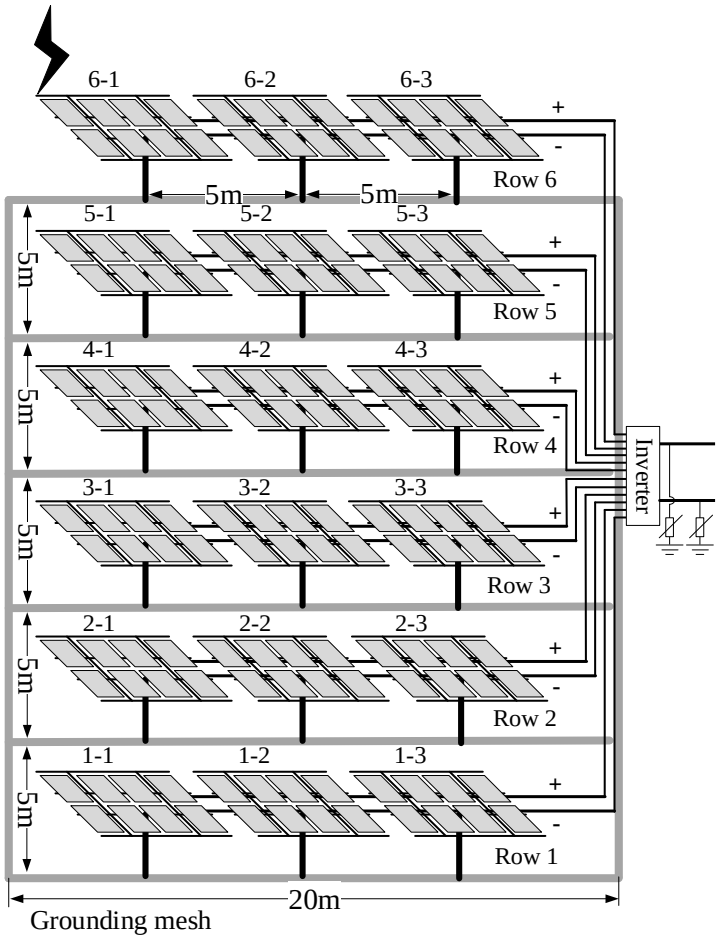

Figure 5.18 The configuration of a PV array

5.5 Transient analysis in a PV power system

Solar energy is an important source of clean and renewable energy [97]. Thanks to the cost reduction of photovoltaic (PV) panel, solar energy becomes a highly appealing source of electricity. The large-scale PV power plants are established widely nowadays. Since the PV plants are usually installed in an open area, they are vulnerable to be damaged by lightning strokes. The lightning protection system (LPS) and wiring mode are crucial to protecting PV plants from loss of human life and economic value. In this section, a PV array is investigated under a lightning stroke by applying the proposed thin wire model.

The configuration of the PV array is shown in Fig. 5.18. This PV array consists of six PV strings. Their positive and negative terminals connected to an inverter 6m away for AC/DC inversion. The output terminals of the inverter are grounded via surge protection devices (SPD) and extend to infinitely long. Another SPD is installed between the positive and negative points inside the inverter. The interval between two PV strings is 5 m. Each PV string contains three PV frames with 5 m interval. 8 PV modules are installed above a PV frame, and 24 PV modules are connected in series in a PV string. The PV frames are made of 6 steel bars with U-shaped cross sections, as shown in Fig. 5.19 (a). The lengths of horizontal and vertical steel bars are 4m and 3 m, and the intervals are 1m and 2 m respectively, as shown in Fig. 5.20. A steel rod with a circular cross section supports the PV frame 1m above a lossy ground. 1m length of the steel rod is buried underground.

Non-isolated LPS [98] is adopted. The lightning channel strikes the 6-1 PV frame directly. All the PV frames are connected underground. A 20×25 m grounding mesh connects all the PV frames with 1m depth. This grounding mesh is made of slabs with rectangular cross sections, as shown in Fig. 5.19 (b). The conductivity, relative permittivity and permeability of the slab and U-shaped PV frame are 1e6 S/m, 1 and 100. The voltage difference between PV frame and DC circuit, as well as the voltage difference between the positive and negative terminals in every row are measured.

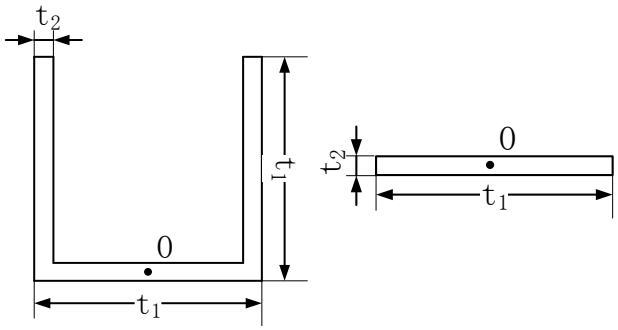

(a) U shape (b) Rectangular shape

Figure 5.19 The cross sections of PV frames and slabs underground (t1=60mm, t2=2mm)

The PV array is investigated by the FDTD method. The computation area contains $230 \times 230 \times 150$ cells, and it is covered with six planes of the perfectly matched layer (PML) absorbing boundary condition to absorb unwanted reflection. The universal non-uniform mesh technique is adopted. The cell size near the PV array is 0.2 m, and increases to 4 m gradually. The lightning channel is simulated by a current source. The negative terminal connects to a corner of the PV 6-1. The current source generates a waveform of the first negative stroke, i.e. 1/200 μs,

with 100 kA amplitude. Under a lightning strike, the connection of input terminals within the inverter is regarded as paralleled. An SPD is installed between the positive and negative points. Output terminals of the inverter are grounded via two SPDs and attached to PML boundary. The non-linear lumped components, SPD, are modeled as active current sources with piece-wise linear method [96]. The clamp voltage is set as 1.5 kV. The electric circuits embedded in the PV modules are simplified as return circuits above the PV frames. The time step is defined as 3e-10 to maintain computational stability. The wire structures, including PV frames and underground slabs, are simulated by the proposed thin wire models. To speed up the simulation, the grounding mesh and PV frames in row 5 and 6 are modeled as lossy wire structure with considering frequency-dependent parameters. The other PV frames, which located far away from the lightning channel, are regarded as perfectly electrical conductors (PEC) with U shaped cross section.

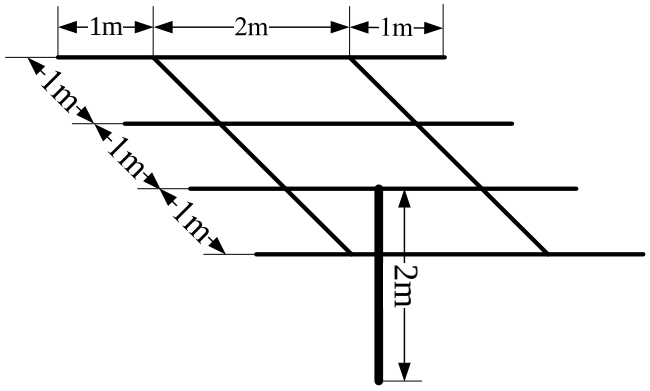

Figure 5.20 The configuration of a single PV frame

The voltage differences between the PV frames and DC return circuits of PV 6-1, 3-1 and 1-1 are shown in Fig. 5.21. A voltage surge is observed at PV frame 6-

1 during the rising edge of the lightning channel. The surge amplitude is as large as 2 MV. After 1μs, the voltage differences are tend obtain a steady state. The maximum and minimum steady stage voltages are 56.5 kV and -13.5 kV. It is possible that the PV frame and DC return circuits are broke down during a direct lightning stroke. Special protection schemes are required.

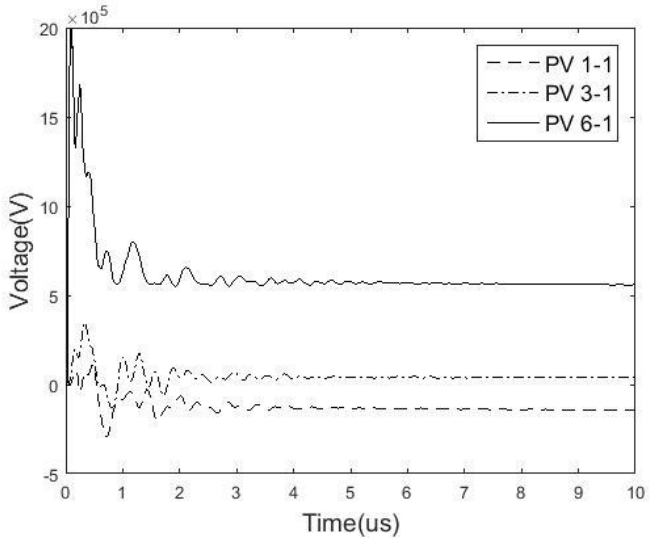

Figure 5.21 The voltage differences between the PV frames and DC return circuits of PV 6-1, 3-1 and 1-1

5.6 Summary

In this chapter, an FDTD thin wire model with the equivalent circuit and surface charge simulation methods were proposed to simulate lossy thin wire conductors with arbitrary cross sections, such as rectangular shape, H-shape, cross shape, L-shape, T-shape, U-shape and others. In this method, frequency-dependent and position-variant field quantities were evaluated with the surface charge simulation method and equivalent circuit method in the initialization process. Time-domain

field correction factors are obtained with the vector fitting technique. The frequency-dependent conductor loss is fully taken into account by four-separated E field components, which are also obtained with the vector fitting technique. All the frequency dependent parameters are embedded into the FDTD calculation in a convolutional approach. General guidelines on wire zone meshing are provided as well.

The proposed model has been validated analytically and numerically. It is shown that this improved thin wire model can achieve good accuracy with much fewer computation resources in transient simulations. It is found that the computation time is reduced to 1% of that with the conventional FDTD method, and the computer memory to 30% in the tested case. The model has been applied to simulate lightning transients in a light rail system and in a PV power system. The frequency response of the lossy rail track can be simulated by a thin wire model rather than extremely fine meshes. The voltage difference between the PV frame and DC return circuits is measured. The FDTD calculation remains stable after 312 thousand time steps.

5.7 Appendix

In a conductor made of linear magnetic material, contribution resulting from magnetic polarization has to be included in the voltage equation. According to the constitutive equation for a linear magnetic material, the following matrix equation

in terms of element current (I_c) and magnetization vector (M_x and M_y) is established [99] for 2D conductor under quasi-static conditions,

$$\begin{bmatrix} j\omega\mathbf{G_{11}} + K_e\mathbf{E} & j\omega\mathbf{G_{12}} & j\omega\mathbf{G_{13}} & \mathbf{I} \\ \mathbf{G_{21}} & \mathbf{G_{22}} - K_m\mathbf{E} & \mathbf{G_{23}} & \mathbf{0} \\ \mathbf{G_{31}} & \mathbf{G_{32}} & \mathbf{G_{33}} - K_m\mathbf{E} & \mathbf{0} \\ \mathbf{S} & \mathbf{0} & \mathbf{0} & 0 \end{bmatrix} \begin{bmatrix} \mathbf{J_c} \\ \mathbf{M_x} \\ \mathbf{M_y} \\ \Delta V \end{bmatrix} = \begin{bmatrix} \mathbf{0} \\ \mathbf{0} \\ \mathbf{0} \\ I_{total} \end{bmatrix}$$

where $K_e = 1/\sigma$ and $K_m = \mu_0\mu_r/(\mu_r - 1)$. **E** is a unit diagonal matrix and **I** is a unit vector. Matrix **S** contains the areas of rectangular elements. Entries in parameter matrixes **G** of (A1) are given, as follows:

$$G_{11.i,j} = \sum_{j=1}^{M} \frac{\mu_0}{2\pi\Delta s_j} \int_{S_j} \ln\frac{1}{\rho_{i,j}} ds_j$$

$$G_{12.i,j} = \sum_{j=1}^{M} \frac{\mu_0}{2\pi} \int_{S_j} \frac{y_j - y_k}{\rho_{i,j}^{\ 2}} ds_j$$

$$G_{13.i,j} = \sum_{j=1}^{M} \frac{\mu_0}{2\pi} \int_{S_j} \frac{-(x_j - x_k)}{\rho_{i,j}^{\ 2}} ds_j$$

$$G_{21.i.j} = -\sum_{j=1}^{M} \frac{\mu_0}{2\pi\Delta s_j} \int_{S_j} \frac{y_j - y_k}{\rho_{i,j}^{\ 2}} ds_j$$

$$G_{31.i,j} = -\sum_{j=1}^{M} \frac{\mu_0}{2\pi\Delta s_j} \int_{S_j} \frac{-(x_j - x_k)}{\rho_{i,j}^{\ 2}} ds_j$$

$$G_{23.i,j} = G_{32.i,j} = \sum_{j=1}^{M} \frac{\mu_0}{2\pi} \int_{S_j} \frac{2\left(x_j - x_k\right)\left(y_j - y_k\right)}{\rho_{i,j}^{\ 4}} ds_j$$

$$G_{22.i,j} = -G_{33.i,j} = \sum_{j=1}^{M} \frac{\mu_0}{2\pi} \int_{S_j} \frac{\left(x_j - x_k\right)^2 - \left(y_j - y_k\right)^2}{\rho_{i,j}^{\ 4}} ds_j$$

By performing elementary matrix operations, element current or current density on the cross section can be obtained in terms of total conductor current I_{total}. Magnetic field components in the vicinity of the conductor are estimated by

$$\begin{bmatrix} H_x \\ H_y \end{bmatrix} = \begin{bmatrix} \mathbf{G_{21}} & \mathbf{G_{22}} - K_m\mathbf{E} & \mathbf{G_{23}} \\ \mathbf{G_{31}} & \mathbf{G_{32}} & \mathbf{G_{33}} - K_m\mathbf{E} \end{bmatrix} \begin{bmatrix} \mathbf{I_c} \\ \mathbf{M_x} \\ \mathbf{M_y} \end{bmatrix} \frac{1}{\mu}$$

6. Surges induced in building electrical systems

Electronic equipment has proliferated in buildings to meet the ever-increasing demand of businesses. Such equipment is susceptible to electrical disturbances generated by lightning. In the past few years the surge environment in buildings has become worse, particularly when insulated down conductors were adopted in lightning protection systems. To protect sensitive equipment against lightning it is necessary to evaluate and characterize the surge environment in buildings.

Lightning surges in buildings can be generated via (a) inductive/capacitive coupling and (b) resistive coupling. The mechanism of resistive coupling has been discussed widely in the past decades. The surge currents/voltages dispersed on low voltage systems have been analyzed under different scenarios and were well documented. Location categories have been introduced in IEEE standards. The lightning surges experienced in buildings have been characterized, and the waveform and amplitude of the surges in different locations have been specified. These surges generally impinge at the service entrance from the circuits outside the buildings. However, little work has been done on the surges arising from inductive/capacitive coupling in buildings during a direct lightning strike.

This chapter presents an analysis of induced surge voltages and currents in a building distribution system during direct lightning. The building is protected by a lightning protection system with insulated down conductors placed in the vicinity

of building distribution circuits. In this chapter both the lightning protection system and distribution circuits are modeled using the Finite-Difference Time-Domain (FDTD) method. Simulations are then performed to study the induced surges in the distribution circuits. Different circuit parameters, such as spacing and distance, are considered in the study, and their impact on the induced surges is revealed. The impact of loads connected to the circuits is investigated as well. A protective measure for suppressing induced surges in a distribution system is presented finally.

6.1 Simulation models

Insulated down conductors (IDCs) are adopted in modern buildings. They are installed in an electrical duct, and run in parallel with power distribution circuits. When a building is struck by lightning, the lightning current in the down conductors emits electromagnetic fields and propagates downwards to the ground. The lightning electromagnetic pulses will induce surge voltages and currents in the adjacent conductors, such as distribution power cables. These conductors are finite in length, and run vertically above the ground. The traditional transmission line theory is not applicable for surge analysis in such cases. The FDTD method is then applied to study the induced surge voltages and currents in these conductors.

The power distribution circuits in the buildings are made with single-core cables. These cables run vertically from distribution transformer to users' equipment on

different floors. Note that transformers are normally modeled as an entrance capacitance in fast transient analysis. For simplicity of discussion, the entrance capacitance is removed in the reference configuration.

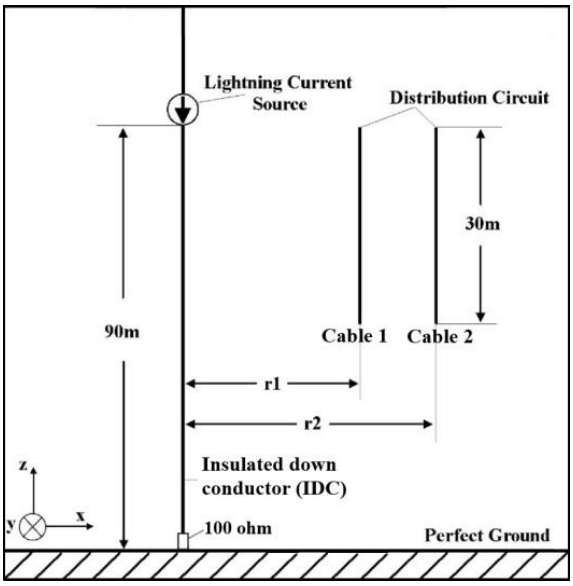

Figure 6.1 Configuration of the down conductor and an adjacent distribution circuit

Fig. 6.1 shows the configuration of a simplified system under investigation. It consists of a single down conductor and two single-core cables situated over the ground. For worst-case analysis the contribution from other down conductors is not taken into account. The down conductor is represented by a 90m-tall cylinder with the radius of 5mm. It is connected to a perfect ground via a 100ohm lumped resistance, and to a current source at another end. An upward conductor is placed at the upper end to mimic a lightning channel. Two distribution cables are modeled by cylinders as well with the height (l_0) of 30m and the radius (r_0) of 5mm. The distances of the down conductor to two conductors are r_1 and r_2, respectively. In the reference case, both r_1 and r_2 are equal to 0.5m and 0.7m, respectively. The

bottom end of the distribution circuit is 60m away above the ground. A lightning return stroke current is injected at the top end of the down conductor.

The working volume of the simulation model is 4m×4m×92.1m. It is surrounded by six planes of perfectly-matched layers (PML) with absorbing boundary conditions being enforced. There are seven layers of the absorbing surfaces in the model, so that the reflected wave on the planes can be effectively minimized. It is assumed that the upward conductor runs to infinity, and no reflected surge in the upward channel travels back to the down conductor. PML absorbing boundary conditions are then applied at the height of 92.1m in the simulation model, as seen in Fig. 6.1. The volume is divided into cuboid cells. The side length of cuboid cells in the z-direction is 50mm near the conductors, and is increased to 500mm gradually to the boundary. The side lengths in the x and y directions are 0.5mm near the conductors, and are increased to 500mm gradually. Time step is determined by the Courant condition,

$$\Delta t \le \frac{1}{c\sqrt{\frac{1}{(\Delta x)^2}+\frac{1}{(\Delta y)^2}+\frac{1}{(\Delta z)^2}}} \tag{6.1}$$

where c is the speed of light, and Δx, Δy, Δz are the side lengths of the smallest cell in meter.

6.2 Induced surges in open circuits

A subsequent return stroke current is applied in the simulation to investigate

induced surges in the distribution circuit. The current source is a fast-front pulse with the rise time of 0.3μs and the amplitude of 10kA. Fig. 6.2 shows waveforms of the surge current (I_{IDC}) at different positions of the down conductor. Because of the surge reflection on the ground the surge current at a lower position of the down conductor is generally higher. The oscillation frequency is determined by the travel time of two round trips on the IDC. As the induced surge is greatly affected by the wave front of an injected surge, time-domain results of the surges for the time period of 2μs are given in the figures.

The induced voltages in the distribution circuit without any connected load were simulated as well. For comparison, the 10kA source current with the rise time of 0.3μs and 1.0μs was respectively applied. The results are presented in Fig. 6.3. It is observed that the induced voltage is linearly proportional to I_{IDC} in the wave front. The induced surges with different rise times tend to reach the same peak value if there is no other surge traveling on the down conductor. Note that there is surge reflection at the bottom of the down conductor. The reflected surge travels back to the observation point before the surge current reaches its peak value when the rise time of the source current is 1.0μs. The induced surge voltage is then lower than that under fast-front current source, as seen in Fig. 6.3.

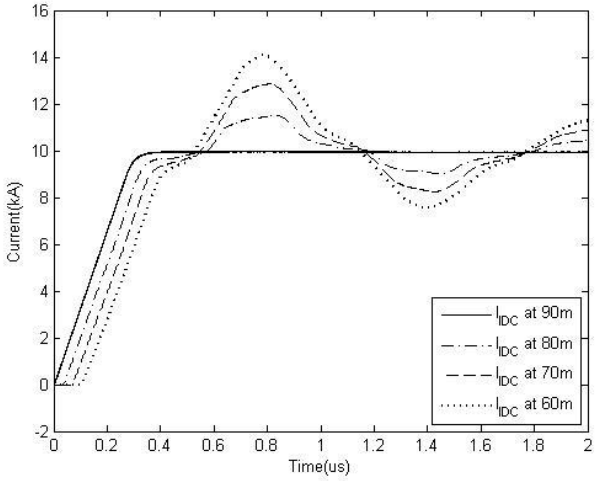

Figure 6.2 Surge currents (I_{IDC}) along the down conductor at different heights

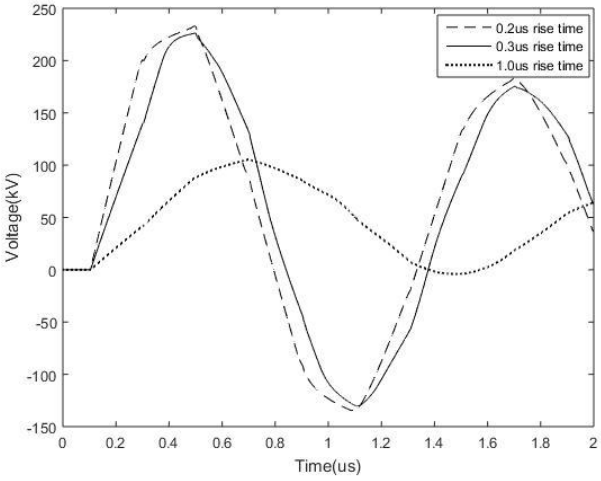

Figure 6.3 Induced voltage at the lower end of the distribution circuit

Computer simulation was also performed to investigate the effect of the distance to the distribution circuit. As the surge voltage was induced between two phase conductors of the circuit, distances of two phase conductors r_1 and r_2 to the IDC were of concern. The peak voltage in the distribution circuit was then evaluated by varying distances r_1 and r_2.

The induced voltage at the bottom end of the distribution circuit was computed

with different values of distances r_1 and r_2. Tables 6.1 and 6.2 show respectively the peak values of the voltage when the spacing d (H = ct$d$=r_1-r_2) is fixed to be 200mm, and the distance r_1 is fixed to be 0.5m. It is noted that the peak value of the voltage decreases with increasing distance to the phase conductor, but increases with increasing conductor spacing. Further investigation reveals that the surge amplitude is linearly proportional to a logarithmic function of r_2/r_1. Tables 6.1 and 6.2 also present the verification results in two cases, that is, (1) with variable r_1, and (2) with variable d.

Table 6.1 Ratio K of peak voltage to ln(r2/r1) with variable r1 (d is fixed)

r_1	Peak Voltage (kV)	r_2/r_1	$\ln(r_2/r_1)$	K(kV)
0.5m	223.980	0.7/0.5	0.336	666.6
1.5m	82.061	1.7/1.5	0.125	656.5
2.5m	49.621	2.7/2.5	0.077	644.4

Table 6.2 Ratio K of peak voltage to ln(r2/r1) with variable d (r1 is fixed)

d	Peak Voltage (kV)	r_2/r_1	$\ln(r_2/r_1)$	K(kV)
0.2m	223.98	0.7/0.5	0.336	666.6
0.5m	462.35	1/0.5	0.693	667.2
1.0m	728.76	1.5/0.5	1.098	663.7

6.3 Induced surges in short circuits

6.3.1 Induced surges in a circuit with two close ends

In this case, the distribution circuit is shorted at both two ends, which mimic a

short circuit at two ends or connection of SPDs to the circuit at both highest and lowest floors. There are apparently zero surge voltages at two far ends because of the short circuit. Induced currents, however, are observed along the distribution circuit between two ends.

Fig. 6.4 shows the waveforms of induced currents at two ends of the distribution circuit when a lightning current is injected at the top end of the down conductor. It is known from the figure that the induced current at the top end has a waveform similar to that of the source current. It reaches 475A approximately around 0.3μs. However, the surge current at the bottom end has a waveform and a peak value different from those of the current on the top end although they are in the same closed loop. The difference is primarily caused by the surge reflection of the IDC current at the ground.

For comparison, induced current using the low-frequency approximation was evaluated as well. At low frequency only the magnetic coupling caused by the current on the down conductor is considered. Assume that the distribution circuit is made of perfect electrical conductors and the source current remains the same along the IDC. According to the Faraday's law, magnetic flux contributed by the source current is balanced by induced currents I_{cab1} and I_{cab2}on two conductors of the closed loop, that is,

$$\Phi_{IDC-loop} = \Phi_{cab1-loop} + \Phi_{cab2-loop} \tag{6.2}$$

where Φ_{X-loop} represents the magnetic flux of the closed loop associated with the

current in conductor X. The flux per unit length in the z direction is expressed by

$$\begin{aligned}\Phi_{IDC\cdot loop} &= \int_{r_1}^{r_2} \frac{\mu_0 I_{IDC}}{2\pi x}\cdot dx \\ \Phi_{cab1\cdot loop} &= -\int_{r_0}^{r_2-r_1} \frac{\mu_0 I_{cab1}}{2\pi x}\cdot dx \\ \Phi_{cab2\cdot loop} &= \int_{r_0}^{r_2-r_1} \frac{\mu_0 I_{cab2}}{2\pi x}\cdot dx\end{aligned} \tag{6.3}$$

Substituting (6.3) into (6.2) yields an equation for both the induced currents and IDC current. Note that the IDC current varies with position on the IDC. The average induced current I_{avr} at position z on the distribution circuit is determined approximately by

$$\begin{aligned}I_{avr}(z) &= \frac{-I_{cab1}(z)+I_{cab2}(z)}{2} \\ &= \frac{\ln(r_2/r_1)}{2\ln\left[(r_2-r_1)/r_0\right]}\cdot I_{IDC}(z)\end{aligned} \tag{6.4}$$

Both induced currents I_{cab1} and I_{cab2} in (6.4) are generally different. However, they turn to be the same at two far ends.

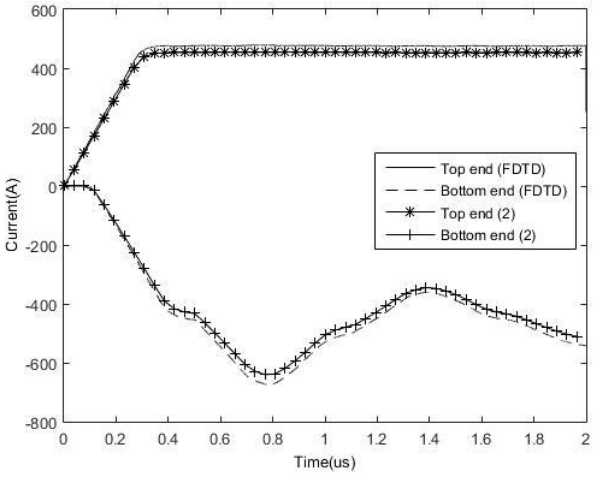

Figure 6.4 Induced currents at two far ends of a shorted distribution circuit

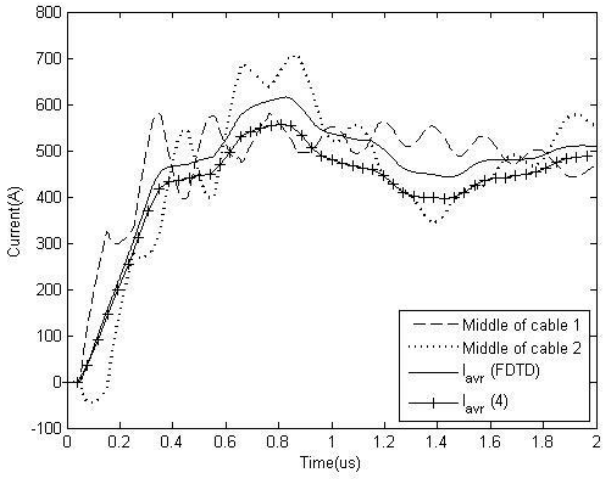

Figure 6.5 Induced currents in the middle of a shorted distribution circuit

The results made with the FDTD method and the low-frequency approximate formula are presented in both Fig. 6.4 and 6.5. Fig. 6.4 shows the surge currents at the two far ends of the distribution circuit. It is seen that the current waveforms match very well, and the difference of surge currents is generally less than 5%. Fig. 6.5 shows the surge currents at the middle of the distribution circuit (75 m above the ground). It is found that both I_{cab1} and I_{cab2} calculated with the FDTD methods are significantly different, and are different from the estimated result with (6.4) as well. However, the waveform of the average current matches well with the low-frequency approximate result, as shown in Fig. 6.4. The difference in magnitude between the FDTD and estimated results of the average current at the middle point is less than 9%.

6.3.2 Induced surges in a circuit with one open end and one closed end

Fig. 6.6 shows the induced voltage along the distribution circuit when the top end is closed and the bottom end is open. It is found that the induced voltage is not equal to zero although a short circuit is made at the top end. The amplitude of oscillation voltage is increased gradually towards the open end, and reaches the maximum at the open end. The peak value of the induced voltage can reach 170kV.

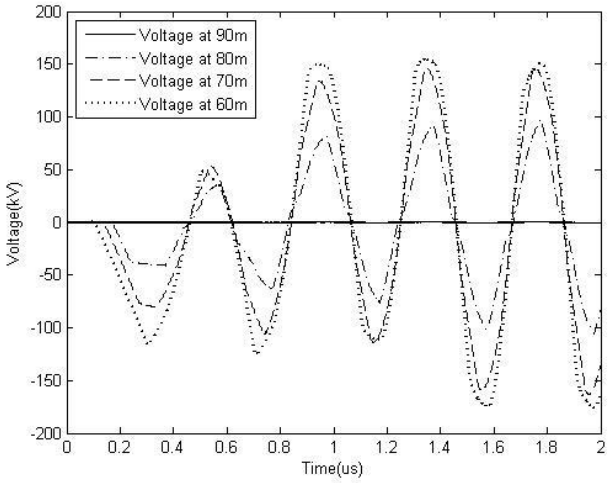

Figure 6.6 Induced voltages on the distribution circuit with one open end and one close end

When a surge propagates downwards on the IDC, the induced voltage in the distribution circuit remains zero initially. This is due to the interaction between the IDC current and induced current in the circuit. When the induced surge arrives at the bottom end, a substantial voltage is observed there. This is because the induced surge current in the distribution circuit could not go further at the bottom end, and a full surge reflection of surge voltage yields at this location. The induced surge

current then travels back towards the closed end, and generates the surge voltage along the circuit.

The surge current continues to propagate along the circuit, and has subsequent reflections at the top end (short circuit) and at the bottom end (open circuit). This leads to an oscillation waveform for the surge voltage in the circuit. The oscillation frequency is determined by the travel time of two round trips. This is because the surge current in a circuit with one open end and one close end changes its polarity for a time period of a round trip. The induced voltage at other location has the same pattern as that at the open end. The magnitude of the induced voltage at other location is less generally, as seen in Fig. 6.6.

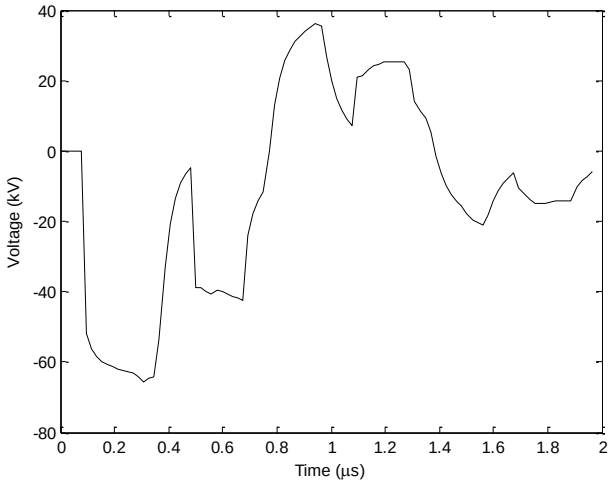

Figure 6.7 Induced voltages on the distribution circuit with the open end and the closed end with the approximate formula

Similar to the induced current in the closed loop, induced voltage at the open end is estimated using the magnetic coupling formula. Induced voltage V_{ind} due

to low-frequency magnetic coupling is expressed by

$$V_{ind}(z) = \frac{\mu_0 l_0}{2\pi} \ln\left(\frac{r_2}{r_1}\right) \cdot \frac{dI_{IDC}(z)}{dt} \tag{6.5}$$

where l_0 is the length of the distribution circuit. Fig. 6.7 shows the induced voltage calculated with (6.5) at the bottom end of the distribution circuit. It is found that induced voltage calculated with (6.5) is totally different from that obtained with the FDTD method. The low-frequency result is proportional to the derivative of the IDC current, and decays quickly as the current derivative becomes small. The FDTD result is an oscillation surge. The amplitude gradually increases to its peak level, and then decays to zero. This is because electric coupling at the open end is significant, but is not taken into account in the low-frequency approximation.

6.4 Induced surges in loaded circuits

Most of the equipment used in buildings has an input circuit (e.g., EMI filter). It is connected to the supply circuit even in standby mode. The input circuit generally has a capacitor, which could suppress the surge induced on the distribution circuit connected. The effect of an input capacitor on induced surges in a distribution circuit is then investigated in this section.

In the simulation the distribution circuit is loaded with a capacitor at the bottom end, and is open or close on the top end. The capacitor placed at the circuit is an "X" capacitor, which is normally used in EMI filters for switching mode power supply. Two different models of the capacitor are considered in the simulation.

Model A is a pure capacitance of 0.22uF. Model B is a series RLC circuit with R=0.122ohm, L=0.38uH and C=0.22uF. In the second model the frequency response of the capacitor is considered.

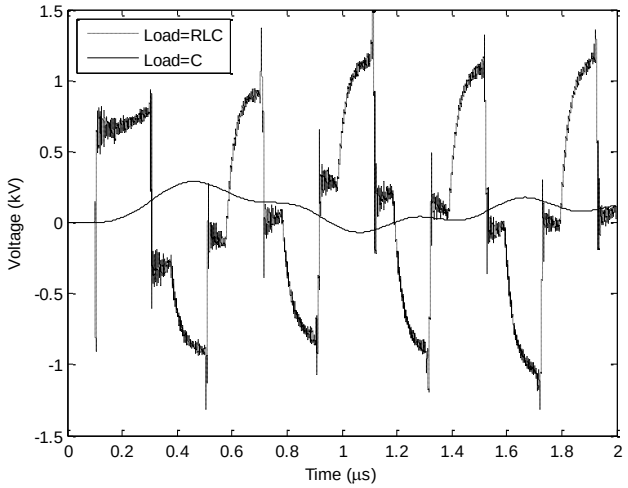

(a) Surge voltages

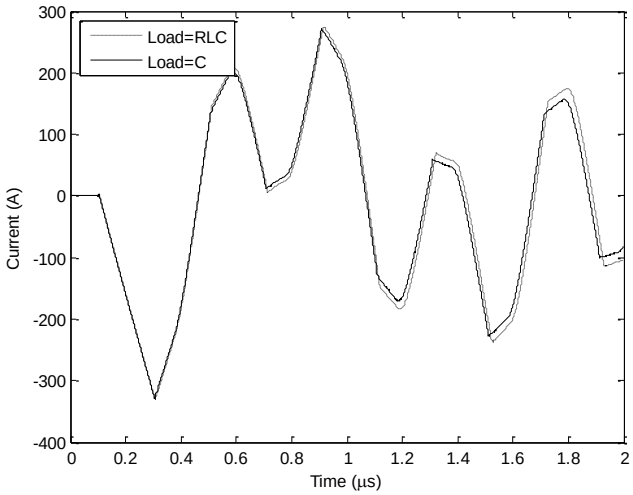

(b) Surge currents

Figure 6.8 Surge voltages and currents on the loaded circuit with an open end on the top

Fig. 6.8(a) shows the waveforms of the surge voltage at the capacitor using these two different models when the top end is open. It is found that the peak voltage

across the Model A capacitor reaches 300V. Compared with the results in Fig. 6.2, the pure capacitance can suppress the induced surge voltage significantly. The induced voltage is highly affected by rise time or change rate of the injected surge current. When the Model B capacitor is connected to the distribution circuit, the induced surge voltage is increased to several kilo-volts. This is caused by the stray inductance of the capacitor, which exists physically in a practical component. The oscillation of the induced surge voltage is determined by the multiple reflections of the surge current on the IDC.

Fig. 6.8(b) shows the waveforms of the surge current on the capacitor. As the circuit eventually behaves like an open circuit, the induced current on the capacitor decays quickly to zero. It is also found that the surge current under two different models matches well. This shows that the surge current does not change significantly, as long as the variation of load impedance is small.

Fig. 6.9 shows the waveform of both surge voltage and surge currents when the distribution circuit is shorted at the top end. In this case the distribution circuit is loaded with a Model A capacitor. It is found that the surge currents are very similar to those in the case of short circuit in the early time period, and are primarily determined by the IDC current. This is because the capacitor behaves like a short circuit at high frequency. Both induced voltage and current eventually have slow-oscillation waveforms, as seen in Fig. 6.9. Actually a resonant circuit is formed because of the capacitance at the bottom end and the equivalent inductance of the

distribution circuit. It is noted that the capacitor voltage is much higher than that when the top end is open, and could cause damage to the capacitor or connected loads. But it is much lower than the induced voltage when the distribution circuit is open at two ends.

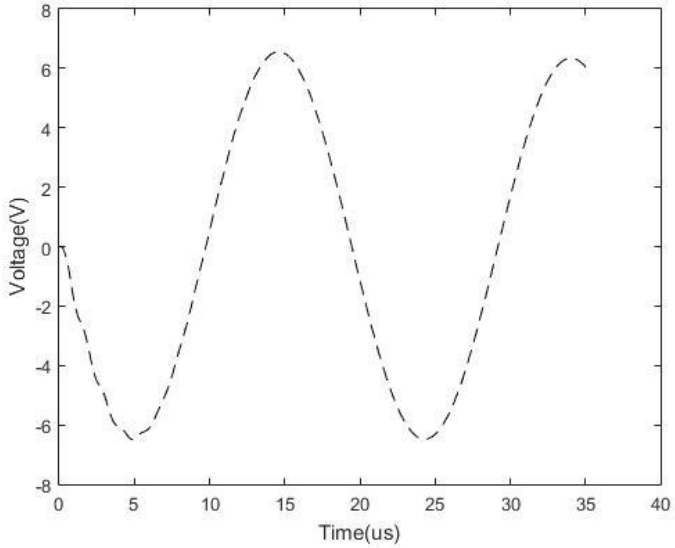

(a) Surge voltage

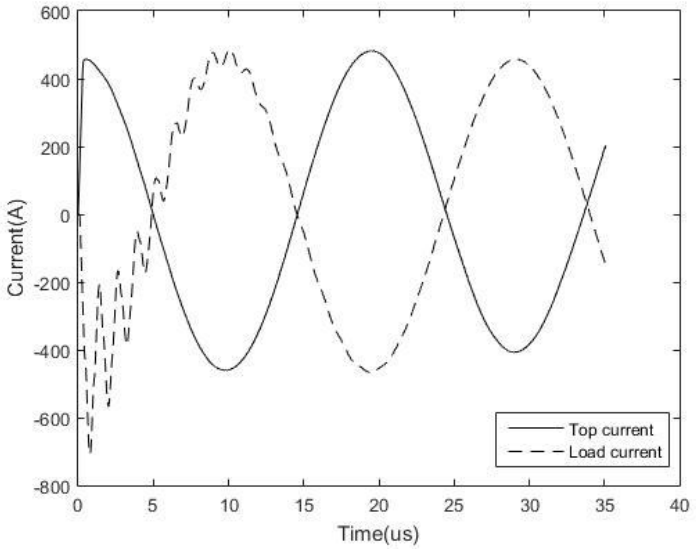

(b) Surge current

Figure 6.9 Surge voltage and currents on the loaded circuit with a close end on the top

6.5 Protection of induced surges with SPDs

Surge protective devices (SPDs) are effective in suppressing lightning surges propagating in the distribution circuits. In modern high-rise buildings, lightning surges may impinge at a service entrance, or be induced from the down conductor. In the latter case, the surges will propagate downwards from the top end of the distribution circuit. To suppress induced lightning surges, it is necessary to install an SPD at the top end. It is noted from Section IV that the induced surge continues to increase towards the bottom end even if a short circuit is made at the top end. A second SPD then is required at the bottom end to suppress the surge there. This pair of SPDs also serves to suppress any surge impinging at the service entrance from the circuit outside. Fig. 6.10 illustrates the protection scheme adopted for the distribution circuit within a building.

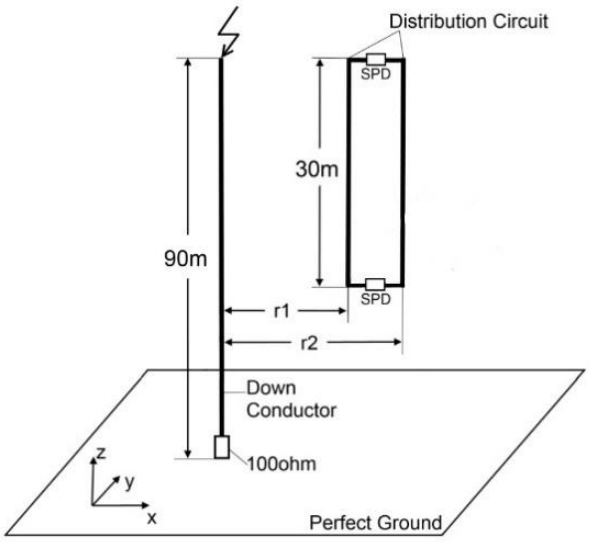

Figure 6.10 Protection scheme for a building distribution circuit

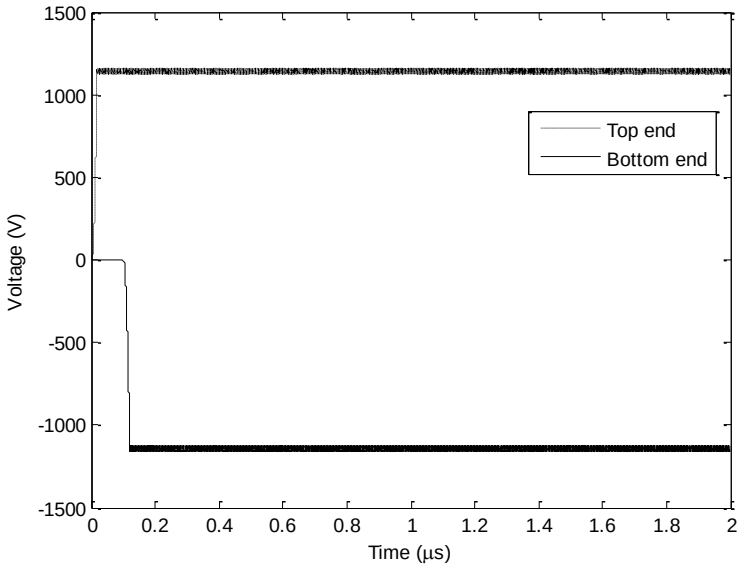

Figure 6.11 Surge voltages on the circuit with SPDs installed at two ends

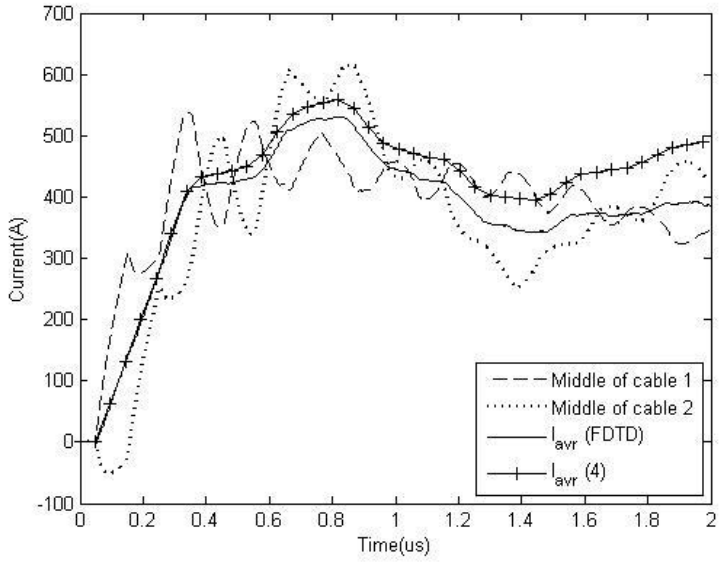

Figure 6.12 Surge currents in the circuit with SPDs installed at two ends

Computer simulation of induced surges is performed using the model shown in Fig. 6.10. Both SPDs in the model have a residual voltage of 1150V, and actually provide a means of a short circuit under the lightning surge environment. The simulation results of SPD voltages and currents are presented in Fig. 6.11 and 6.12.

It is noted from the figures that surge voltages at both ends are limited to the residual voltage of SPDs. It is also noted that the surge currents in the SPDs are very similar in waveform to those found in the short circuit, and are determined by I_{IDC}. This indicates that induced current in a closed loop can be treated an independent current source, and is not affected by load impedance significantly. It is noted that in Annex E of IEC standard 62305-1 that the induced current has a waveform of 8/20μs in a closed loop, given by a 10/300μs lightning return stroke current to a structure. This is different from what is found in this study. The SPD currents are found to be small generally, and are just a few hundred Amperes in peak, compared with the 10kA in the down conductor. Therefore, SPDs installed in the distribution circuit are only used to limit the surge voltages, and are not required to dissipate substantial lightning surge energy observed on the IDC.

6.6 Simulations with thin wire model

The simulations described previously are calculated with the traditional FDTD method which discretizes the thin wire structures into extremely dense mesh. Although the simulation can be optimized by the non-uniform mesh technique, the calculation requires large memory space and long computation time. The thin wire models in the FDTD method is one of the methods to improve calculation efficiency. It is realized by modifying material parameters near the thin wire conductors according to the field distribution pattern to obtain a required equivalent radius. The radius of the thin wire model is smaller than the cell size,

which means there is no need to discretize the thin wire structures with dense mesh. The extended thin wire model proposed in chapter 3 can also be applied to investigate the induced current and voltage in lossy conductors.

In this section, the traditional thin wire model and the extended thin wire model with circular cross section are adopted to simulate induced surges in vertical conductors. Two configurations are selected: 1) the distribution conductors are open at both upper and lower ends; 2) the distribution conductors are closed at both upper and lower ends. For the first configuration, the voltage difference at the lower ends of distribution conductors are measured. The current flow at the lower ends of distribution conductors in the second configuration is calculated.

The working volume is divided into $74\times60\times1860$ cells and is covered with five planes of PML absorbing boundary conditions to absorb unwanted reflected waves. The PEC boundary is selected at the bottom to mimic a perfect ground. The non-uniform mesh technique is adopted in z directions. Cell sizes in x and y directions are 0.05m. The cell size under 90 m in z direction is 0.05 m, then it is increased to 2.5 m gradually. The radius of the thin wire conductors is 0.005 m. The upper terminal of the down conductor is attached to the absorbing boundary to simulate infinitely long.

The induced voltage and current simulated by the traditional FDTD method, traditional thin wire model and extended thin wire models are shown in Fig. 6.13 and Fig. 6.14. The three groups of waveforms match well for the first impulse. A

small discrepancy is observed at the subsequent impulse, especially in the case of two ends open. This discrepancy may be caused by the non-uniform mesh setting in the traditional FDTD method. The waveforms of lossy and lossless thin wire models have no significant difference in these two cases.

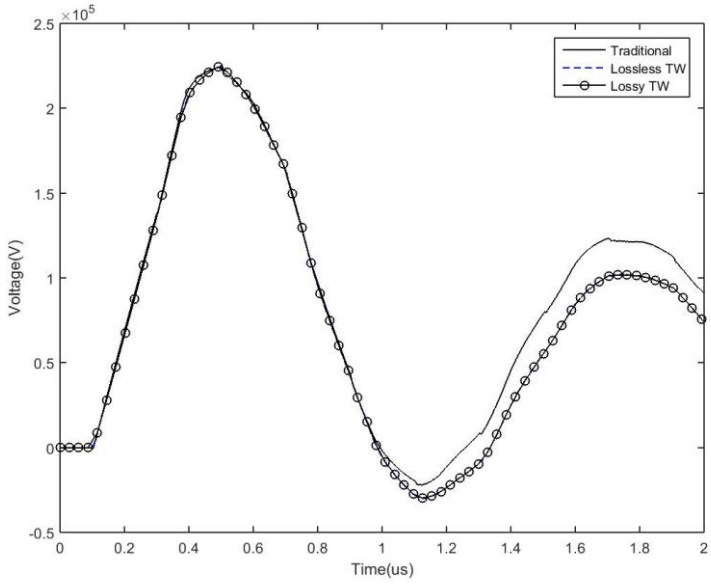

Figure 6.13 Induced voltage at the lower end of distribution conductors

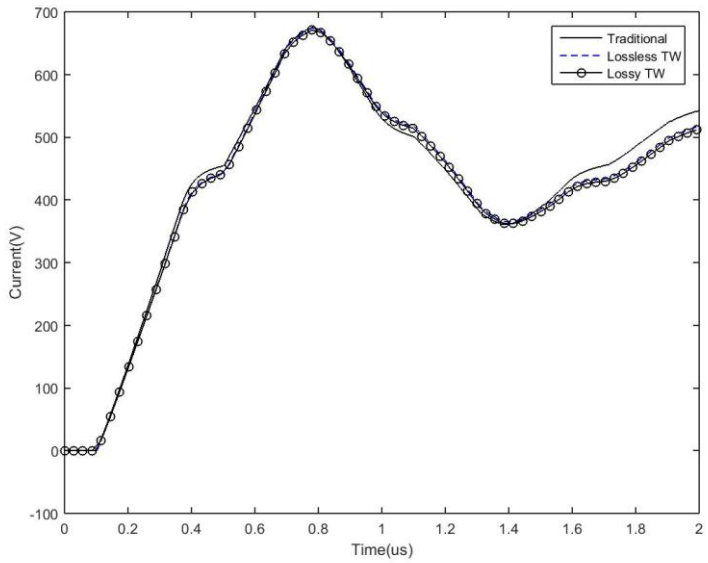

Figure 6.14 Induced current at the lower end of distribution conductors

6.7 Summary

This chapter presented a numerical investigation into lightning-induced surges in building distribution circuits. When the lightning current to the building is discharged by an insulated down conductor, substantially induced surges are generated in the adjacent circuits due to both electric coupling and magnetic coupling. The induced surges are different from those obtained using quasi-static models.

It is concluded that the induced surge voltage in an open circuit is linearly proportional to wave-front parameters of the lightning discharge current at the rising stage, and is determined by the logarithmic function of a distance ratio of two circuit conductors. It is found that capacitors connected to the circuit can reduce the induced surge voltage, but may not be effective in suppressing the voltage down to an acceptable level. It is recommended installing SPDs at two far ends of a distribution circuit. As the surge currents are relatively small, those SPDs are not required to dissipate substantial lightning surge energy observed on the down conductor. It is also found that the surge currents in SPDs are very similar to those in short circuits. The induced current can be treated as an independent current source. It is determined by the current in the down conductor, and has a waveform similar to the down-conductor current. The surge induced current can be estimated using a low-frequency approximate formula.

7. Lightning analysis of a tall tower

Lightning protection systems (LPS) play an important role in protection for buildings and other grounded structures. The LPS discharges huge lightning current into the earth in a short time in case of a lightning strike, and it is intended to provide safety protection for the personnel and equipment in or around the grounded structures. It then is necessary to analyze the lightning discharge currents in the grounded structure and ground potential rise (GPR) in its vicinity during a lightning strike.

In this chapter, lightning-induced electromagnetic environments in a meteorological (lightning) observation tower are analyzed. The FDTD method is employed to simulate the performance of the LPS under a direct lightning strike. The current distribution within the tower is analyzed first. The ground potential rise of the tower and step voltage in the vicinity of the tower then are calculated with different tower configurations.

Voltage can be derived by both electric field and magnetic vector potential especially under high frequency excitation. In the FDTD method, voltage (potential difference) and current on thin wires are directly calculated from electric and magnetic fields along specific paths. At low frequency, the potential difference can be calculated using a line integral of the electric field. However, in transient analysis significant frequency components of a surge current may be extended to

MHz or above. The inductive influence on the potential cannot be ignored. In this chapter, the inaccuracy reason for the voltage measurement in the FDTD domain will be investigated theoretically. Two cases with and without considering magnetic vector potential in voltage measurement will be compared.

7.1 Inaccuracy of the voltage measurement in the FDTD domain

A complete calculation method of potential difference should be used, which includes the contribution from both the electric field and the current in the wires, as follows:

$$V = \int_l \vec{E} dl + \int_l \frac{\partial \vec{A}}{\partial t} dl \,, \tag{7.1}$$

where l is the path for evaluating the voltage. In (7.1), the first item is calculated directly using FDTD results. The second item is determined by vector potential A, which can be approximately expressed by

$$\vec{A} = \frac{\mu_0}{4\pi} \int_{l'} \frac{1}{r} I\left(\vec{r}, t-\tau\right) dl' \,. \tag{7.2}$$

where $\vec{r}$ is the vector of a field point from the source current point, and τ is the traveling time of an electromagnetic wave from the source point to the field point (time delay). Substituting (7.2) in (7.1) yields the potential difference expressed by both electric field along the path and current along the wires, as follows:

$$V = \int_l \vec{E} dl + \frac{\mu_0}{4\pi} \int_l \int_{l'} \frac{1}{r} I\left(\vec{r}, t-\tau\right) dl' dl \tag{7.3}$$

Taking a 2×2 horizontal grid network with the mesh size of $2m\times2m$ as an example to investigate the difference between the voltage measurements

considering magnetic vector potential or not, as shown in Fig. 7.1. It is buried under the ground with a depth of 0.5m. An impulse current source, which represents the 2nd lightning return stroke, is placed at the height of 2m and is connected to the grounding system via a vertical conductor. The source current has the amplitude of 10 kA, and is expressed mathematically by

$$I(t) = kI_0\left(e^{-\alpha t} - e^{-\beta t}\right), \tag{7.4}$$

where $\alpha = 6.93147 \times 10^3 S^{-1}$, $\beta = 1.76310 \times 10^7 S^{-1}$, $I_0 = 1A$, and $k = 10000$. The conductors used in air and under the ground have the radius of 5mm. These conductors are represented by the thin-wire model in the simulation, in which electric field components are forced to be zero [2]. For simplicity of discussion, the ground soil is assumed to be homogeneous and non-dispersive. It has the conductivity of 0.01S/m and relative permittivity of 4.

There are two different approaches for the ground potential rise (GPR) calculation, that is, with and without the voltage reference connected to remote earth at 50 m away. In case of presence of the reference wire, the voltage is evaluated across the gap at the local earth. The inductive voltage contributed by the magnetic vector potential is negligible. Fig. 7.2 shows the inductive voltage contributed by the magnetic vector potential in the case of absence of the reference wire. It is relatively significant in the wave front.

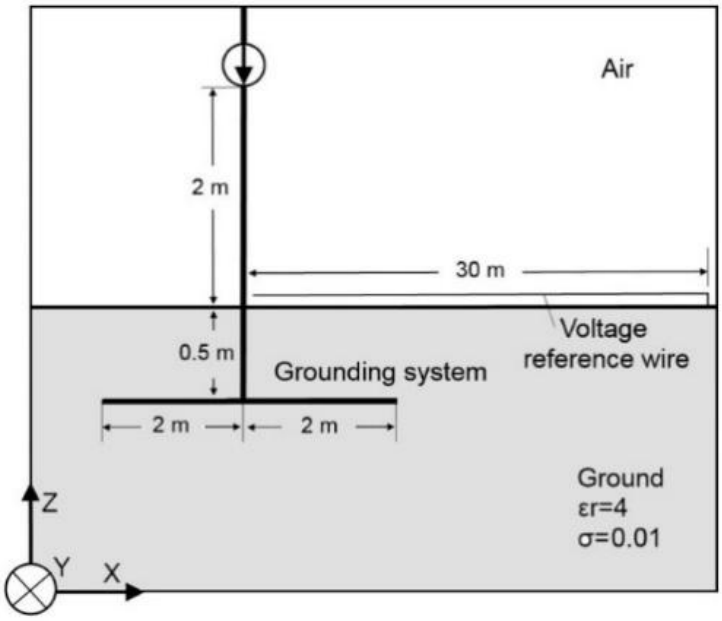

(a) Side view

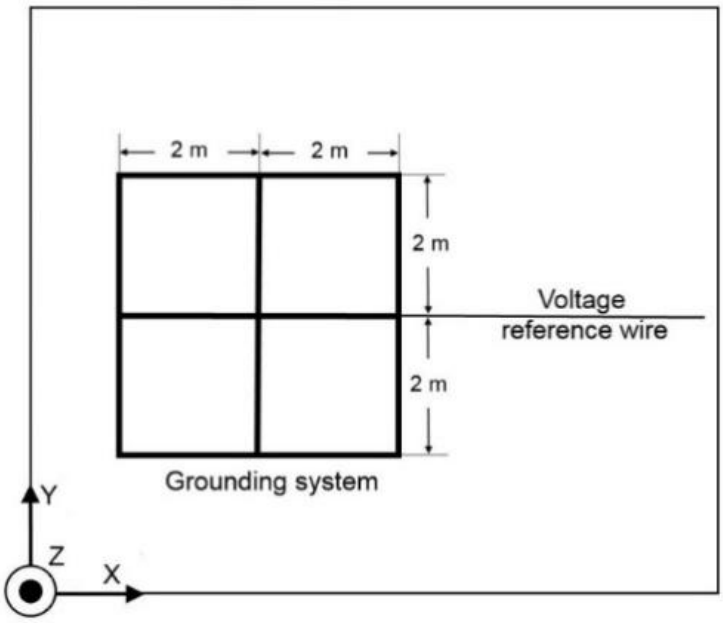

(b) Plan view

Figure 7.1 Grounding system configuration B

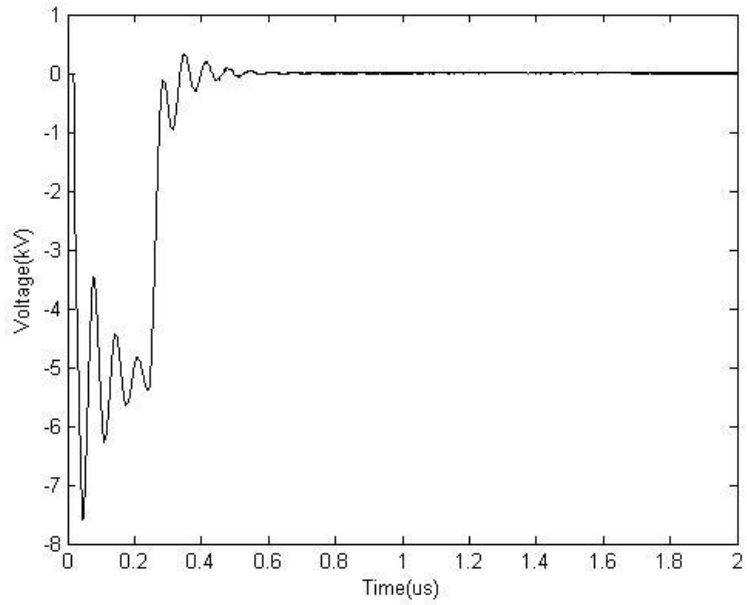

Figure 7.2 Inductive voltage generated by the grounding system

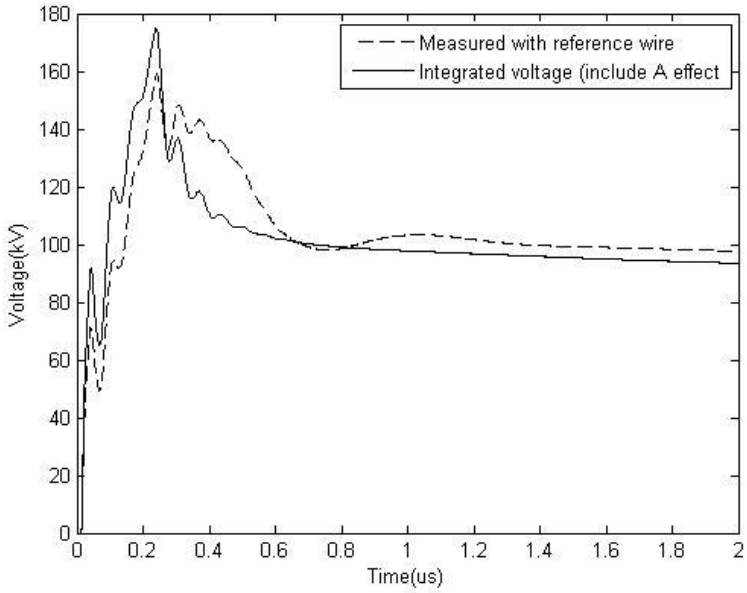

Figure 7.3 GPR measured with and without the voltage reference wire

Fig. 7.3 shows the waveforms of the GPR in two different cases. It is found that the oscillation around the peak of GPR is contributed by the vector potential contributed by the current in the grounding system. Using a reference wire leads

the slow oscillation after the peak in the GPR waveform. The resistive component of the GPR in this case is slightly higher than that without the reference wire. The component contributed by the vector potential may be significant at the wave front. It can be neglected when the surge current changes slowly.

7.2 Tall towel system modelling

The structure of the meteorological observation tower consists of four parts: a 350 m tall vertical main body, a grounding mesh, four horizontal grounding bars and a number of steel cables, as shown in Fig. 7.4. The grounding mesh and four horizontal grounding bars are buried under the ground with a depth of 3 meters from the ground surface. The grounding mesh consists of a wire network and pillars. A number of vertical rods are connected to the intersectional points of the mesh. The detailed geometric information of the mesh is shown in Fig. 7.5. The horizontal grounding bars with the length of 262m, are extended from the edge of the grounding mesh along two orthogonal directions. A number of steel cables are provided to strengthen the structural stability of the tower. One terminal of the steel cables attach the tower main body on its top end, and the other terminal is tied to the foundation on the ground.

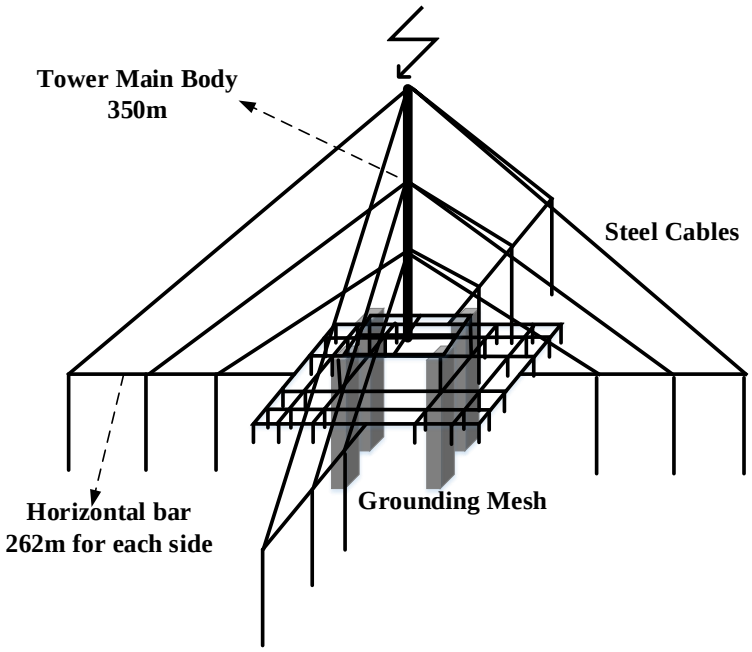

Figure 7.4 Configuration of the meteorological observation tower

In the FDTD working volume, a simulation model is established based on the geometrical information given in Fig. 7.4 and Fig. 7.5. The working volume is divided into $310 \times 250 \times 230$ cells, which represents $1134\text{m} \times 2584\text{m} \times 1369\text{m}$ in space. A non-uniform mesh technique is adopted. The cell size in the vicinity of the tower foundation is 0.5 m, and is gradually increased to 16 m at the boundary. The conductive components, including the tower main body, grounding mesh and vertical rods, are regarded as a perfect electrical conductor (PEC), and are represented by a thin wire model. The pillars in the tower foundation and cable foundations are represented by discretized cuboid Yee cells. The inclined steel cables are modeled using the approach of staircase approximation [90]. The ground soil is assumed to be homogeneous with a conductivity of 0.001S/m and relative permittivity of 10. The PML absorbing boundary condition is adopted on

its boundary to absorb unwanted reflections at the boundary.

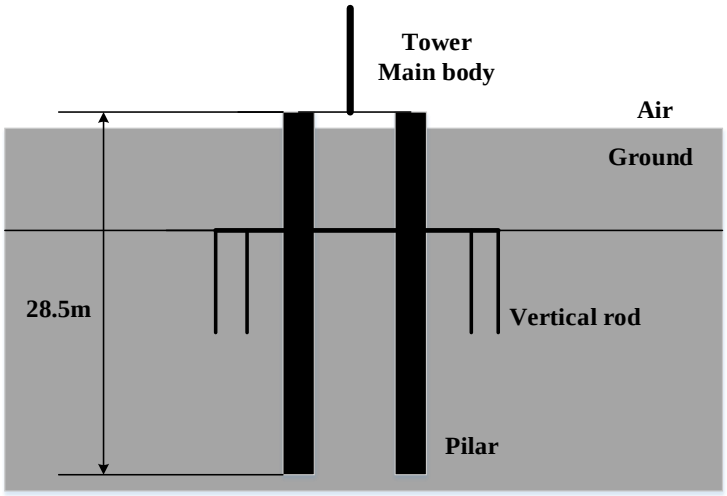

(a) Front view

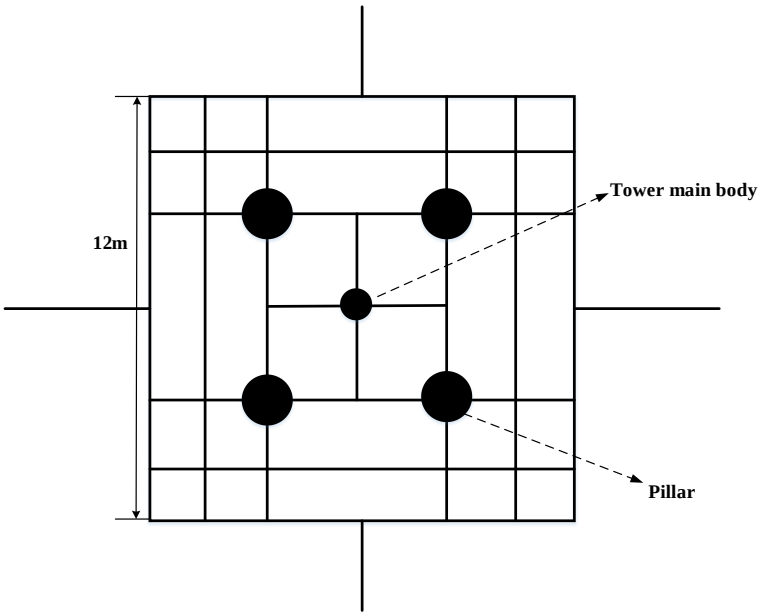

(b) Top view

Figure 7.5 Detail of the grounding mesh geometry

The lightning stroke is mimicked by a current source connected to the main body of the tower. The lightning channel is represented by a thin conductor. It is connected to the top end of the tower model, and runs upward through the PML

boundary. The mathematical expression of the current source waveform is

$$I(t) = I_0(e^{-\alpha t} - e^{-\beta t}) \tag{7.1}$$

where $\alpha = 1.93147 \times 10^3\ \mathrm{S}^{-1}$, $\beta = 4.76310 \times 10^5\ \mathrm{S}^{-1}$, $I_0 = 10\ \mathrm{kA}$. In this case, the current reaches the peak at 10 μs and attenuates to half of the amplitude at 350 μs.

7.3 Simulation results

When the tower is struck by lightning, the lighting current will be discharged into the earth via the main body as well as a large number of steel cables. Although the inclined steel cables are constructed for stabilizing the tower structure, they do affect the current distribution within the tower as well as the electromagnetic environments in the vicinity. The horizontal copper bars, vertical rods as well as pillars are buried under the ground. They serve as the grounding electrodes for dissipating lightning energy into the earth. It would be necessary to investigate the lightning current distribution among different tower components, the ground potential rise of the tower, and step voltage in the vicinity of the tower.

7.3.1 Current distribution

Computer simulation with the FDTD method is performed to investigate the current distribution in the tower shown in Fig. 7.4. The surge currents in the main body and three steel cables on one side of the tower are measured. Fig. 7.6(a) shows the current waveforms of these currents recorded at the surface of the

ground. It is found that the main body carries a small portion of the lightning discharge current containing low frequency components only. The current reaches 300 A at 40-50 μs, compared with the 10 kA at 10 μs for the lightning current injected to the tower. The majority of the lightning discharge current flows through four outmost steel cables. The current in one outermost cable can reach 2.8kA in the early time period, and contains significant high-frequency components due to wave reflection at the ground. If the tower is considered as a metallic cone, the surge current tends to flow along its surface due to the skin effect.

Four measurement points are selected along one of the horizontal bars to study the lightning energy dissipation underground. These points are located at 7 m, 60 m, 140 m and 266 m away from the main body. Fig. 7.3(b) shows all the currents are negatively polarized, which means all the currents flow from the foundation for the outermost steel cables to the foundation of the main body. It is noted that the peak of the surge current on horizontal grounding bar current generally decreases when moving towards the center of the tower. The difference of the currents between at the outermost steel cable and the main body is the current dissipated into the earth through the horizontal copper bar.

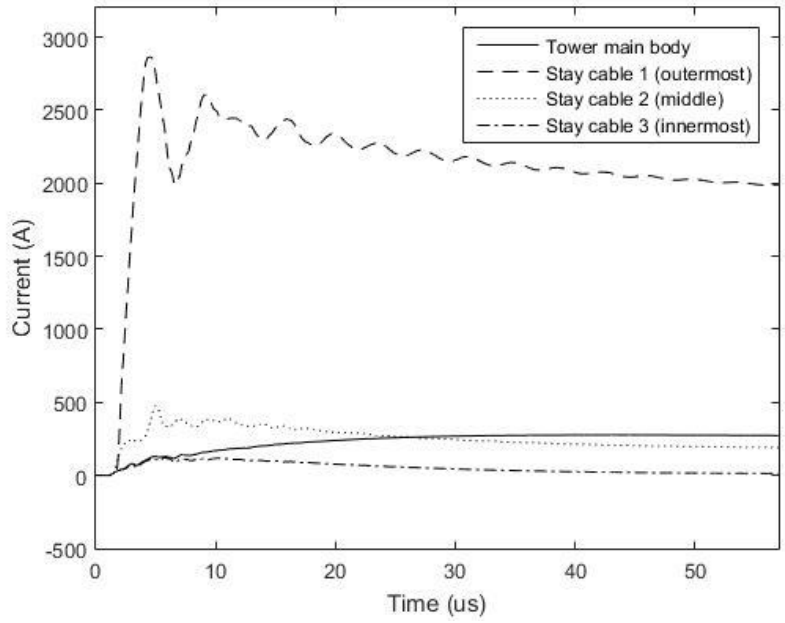

(a) Surge currents in tower and steel cables

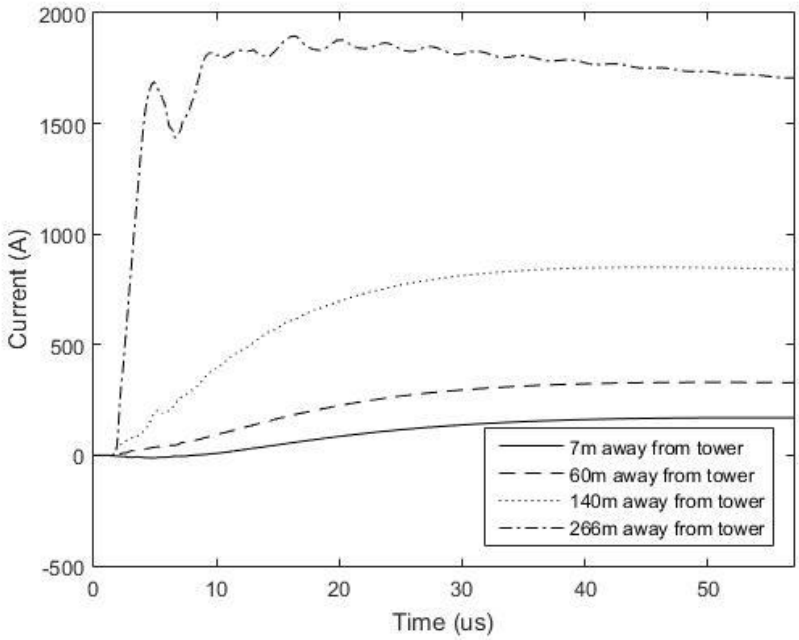

(b) Surge current along the horizontal grounding bars

Figure 7.6 Surge current in the tower system

7.3.2 Ground potential rise

To investigate the influence of the inclined steel cables and horizontal bars on the ground potential rise, three grounding configurations are selected for study,

that is, (1) reference configuration (a), (2) simplified configuration (b) and (3) simplified configuration (c). The reference configuration is illustrated in Fig. 7.1 and Fig. 7.5, which contains all the tower components, such as the tower main body, grounding mesh, horizontal grounding bars and inclined steel cables. In the simplified configuration (b) the horizontal grounding bars are removed. In the simplified configuration (c) both horizontal grounding bars and the grounding electrodes for steel cables are removed. In measuring GPR, a voltage measurement wire is arranged at the height of 1 m over the ground, and runs from the measurement point to a reference point 370 m away from the center.

Fig. 7.7(a) shows the waveforms of GPR measured at the foundation for the main body in three different grounding configurations. It is found that GPR under the reference configuration is relatively low, and is approximately equal to 30kV in peak. There is no much difference of GPR in both configuration (a) and configuration (b). This is probably because the surge current in the foundation for the main body is small. In simplified configuration (c), GPR is increased significantly to 200kV as all the lightning discharge current will flow through the tower foundation.

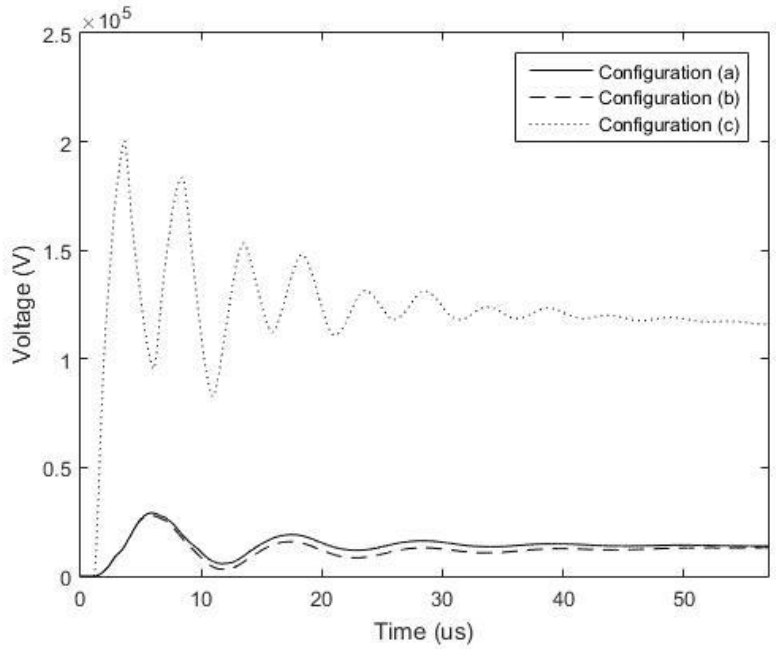

(a) GPR of the tower foundation

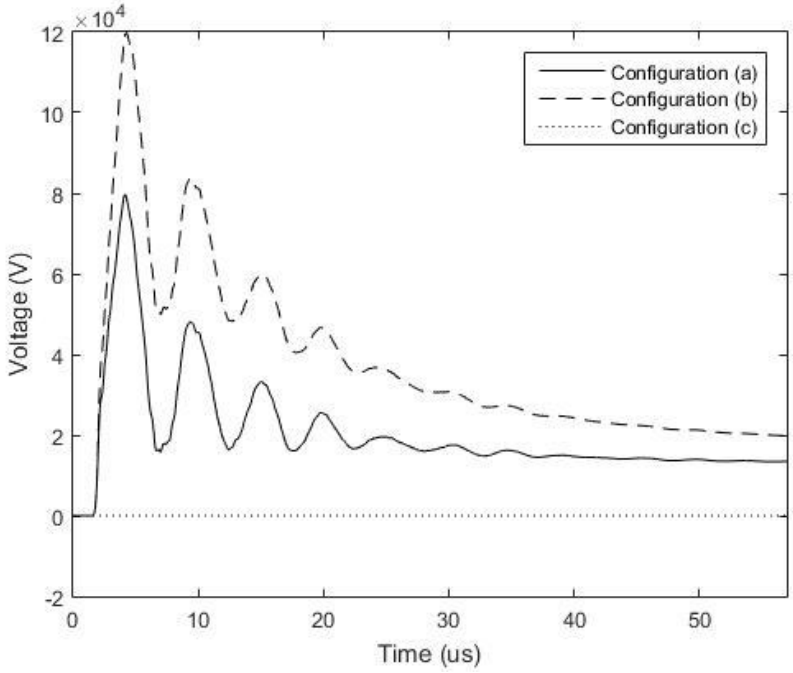

(b) GPR of the cable foundation

Figure 7.7 GPR waveforms measured in three configurations

GPR at the far end of the horizontal grounding bar is measured as well. The waveforms of GPR in three different configurations are presented in Fig. 7.7(b). It

is noticed that GPR along the grounding bar is significantly different due to the inductance effect at high frequency. The GRP at the far end of the grounding bar is greater than that at the tower foundation. In the simplified configuration (b) without the horizontal grounding bar, the GPR is even higher as the majority of the lightning discharge current flows through the grounding electrode of the outermost steel cables.

7.3.3 Step voltage

Step voltage is one of the key issues addressed in the lightning protection. It could be significant in the vicinity of grounding electrodes, and may cause fatalities of human beings or livestock. It is quite important to understand how step voltage varies in the vicinity of the grounding systems for the tower.

In the reference configuration, step voltage was measured in the zone adjacent to the tower foundation, as well as the cable foundation. Fig. 7.8 shows the measured waveforms of step voltage in these two different zones. It is found that the step voltage is very small, and reach the local maximum at the edge of the mesh network. When the observation point is a little bit away from the mesh network, the step voltage will decrease with increasing distance to the tower. Step voltage reaches the maximum value at the foundation of the outermost steel cables.

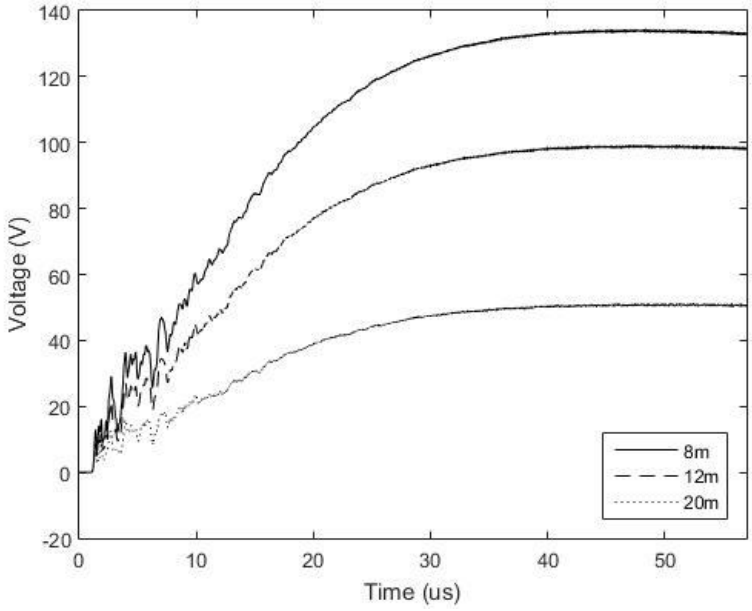

(a) Distance less than 20m

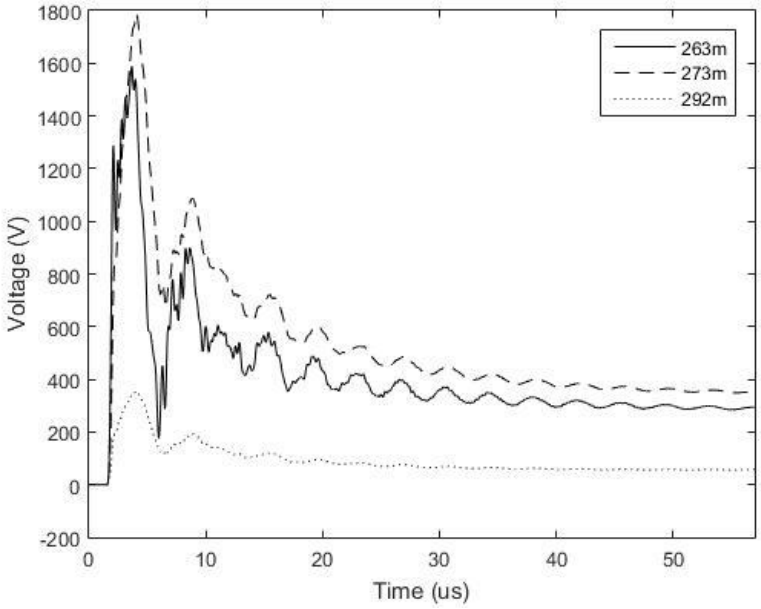

(b) Distance more than 20m

Figure 7.8 Step voltage in the reference configuration

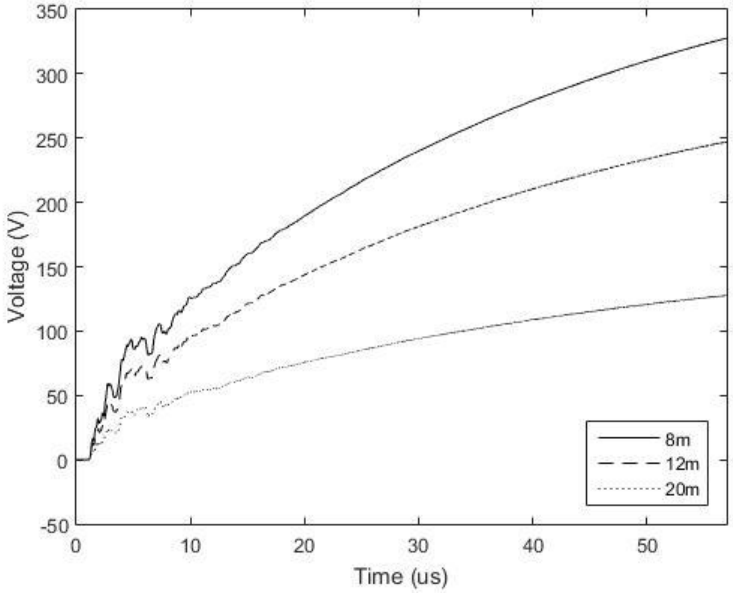

(a) Distance less than 20m

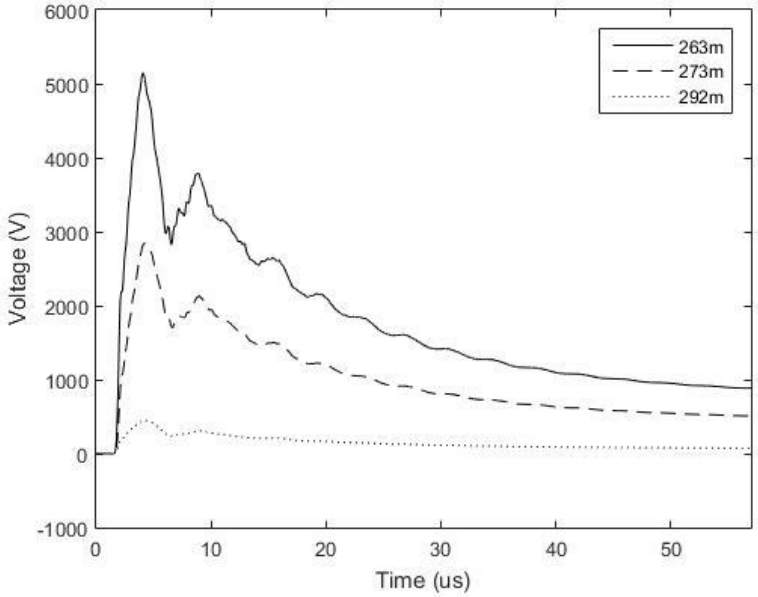

(b) Distance more than 20m

Figure 7.9 Step voltage in simplified configuration (b)

Similar results are observed in the simplified configuration (b), in which the horizontal grounding bars are moved. Fig. 7.9 shows the measured waveforms of step voltage in this configuration. However, the relative values of step voltage are

higher at the foundation of the outermost steel cables, and are 2.5 times as much as those in the reference configuration in the corresponding locations. This is because the lightning current is primarily dissipated into the earth via the foundation of the steel cables. There is no much change of step voltage in other locations.

It is known that the safety step voltage is determined based on the energy passing through a human being in a short duration [100]. The energy absorbed by a human being during a lightning strike can be calculated with

$$\frac{1}{R_b}\sum_{i=1}^{n} V_{step}^2 \Delta t = E_{human} \tag{7.2}$$

where R_b stands for the foot to foot resistance, and Δt is the sample period. In this chapter, R_b is assumed to be 1000 Ω for a 70 kg human, and Δt to be 9.6225×10^{-10}s. The energy threshold of lightning danger to a human being is assumed to be 27 J. Table 7.1 shows the lightning energy absorbed by a human being arising from step voltage in both configuration (a) and configuration (b). The lightning stroke current is assumed to be 100kA. It is found that the lightning energy absorbed by a human being is less than the safety limit in the reference configuration. The location near the foundation for the outermost cables has the largest energy. Similar results are observed in the configuration without the horizontal grounding bar. However, the largest energy in the vicinity of the cable foundation is increased significantly.

Table 7.1 Energy absorbed by the human body

Configuration (a) – Reference Config.		Configuration (b) – Simplified Config.	
Distance X (m)	Energy (J)	Distance X (m)	Energy (J)
8	0.535	8	3.154
12	0.292	12	1.794
20	0.077	20	0.479
263	3.565	263	44.841
273	5.488	273	14.742
292	0.155	292	0.311

7.4Summary

In this chapter, lightning discharge current, ground potential rise and step voltage in or around a meteorological (lightning) observation tower were investigated with the FDTD method. The current distribution among the tower main body and inclined steel cables at the ground surface was measured. It is found that more than 90% of the lightning discharge current is carried by the stay cables. The tower body just carries a small portion of the discharge current with relatively low frequency components only. The majority of the discharge current is dissipated into the earth via the horizontal grounding bars. The step voltage and GPR are analyzed and compared for three different configurations, including the reference

configuration, and two simplified configurations. It is found that the steel cables and horizontal grounding bars affect the grounding performance significantly. The lightning energy absorbed by a human being in the vicinity of the tower with the reference grounding configuration is lower than the safety limit under the 2nd lightning stroke current of 100kA.

8. Lightning surge analysis in light rail transit

Light rail transit is an efficient, clean and convenient massive transportation system. It has been constructed in many cities to alleviate the problems of traffic jam and air pollution. The system normally operates under DC power supply, and requires special grounding and bonding arrangements to satisfy the safety requirements. Electric trains are powered from a rectifier substation (RS) via traction power cables (TPC) and overhead lines (or a third rail). The traction current returns back to RS through rails and traction return cables (TRC). The bonding arrangement of a DC electrified railway system should maintain the amplitude of leakage currents within a safety limit [101]. Otherwise, the leakage current could cause corrosion to metallic parts underground. The diode boxes implemented between rails and fault current return wires (FCRW) are one of the bonding arrangement in a DC electrified light rail system. They can limit the leakage current, and restrict the fault current to the rails from FCRW, instead of other metallic parts on or in the ground.

The light railway usually runs in an open area, and is highly susceptible to lightning. During a lightning stroke, a considerable surge voltage will be generated or induced between the rails and FCRW, which may cause diode breakdown and affect the normal operation of diode boxes. It is necessary to analyze the voltage surge behavior during a lightning stroke under different conditions.

In this chapter, the lightning surges in a light railway system is analyzed using the FDTD method. The surge voltage on the diode boxes between the FRCW and the rails is evaluated under both direct lightning and indirect lightning. The impact of various influential factors is discussed, including the lightning striking point, return stroke current waveform, grounding mesh of structures nearby and soil conductivity. The configuration of the light railway system, as well as the model set in the FDTD domain, is described in section 8.1. The surge voltages under different conditions are presented in the following sections.

8.1 Light railway system model

In this chapter, lightning surges in a DC electrified light railway system is analyzed using the FDTD method. The light railway system configuration is shown in Fig. 8.1. Electric trains are powered by an overhead line (OHL) system at 750 VDC. The OHL system is comprised of contact wires (CW), messenger wires (MW), fault current return wire (FCRW), and poles, insulators (Ins), lightning arresters (LA) and other accessories. Trackside poles are located 1.8 m away from the track with 25 m intervals. The running rails are located 0.4 m above ground with 1.4 m separation. CW and MW are situated 5.6 m above the rail track, and are supported and registered on hinged cantilever assemblies to trackside poles. They are insulated from the poles with insulators. Lightning arresters (LA) are provided at pole L1 and pole R10, and are grounded via dedicated down conductors to the local earth. The grounding resistance is approximately equal to

8 ohm. FCRW is hinged 4 m above the ground, and is bonded to poles directly (except pole L1 and pole R10). Two diode boxes (DB) are mounted between rails and FCRW at pole L4 and pole R6. The maximum inverse voltage of these diodes is 3 kV. A rectifier substation (RS), close to pole R10, feeds CW/MW via traction power cables (TPC) and traction return cables (TRC). TRC is grounded at RS. The rails are also grounded near the pole L1. The surge voltage on the diode boxes at the locations of pole L4 and pole R6 are measured under different conditions.

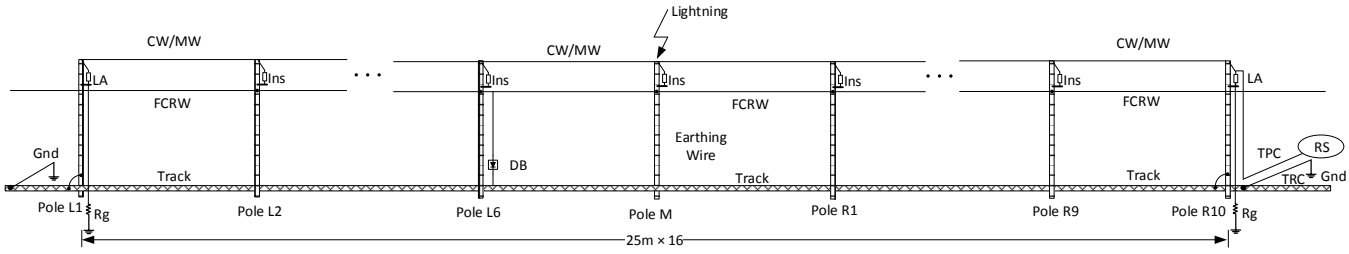

Figure 8.1 The configuration of the light rail system

The model of a light railway system is built in the FDTD domain having $375\times160\times110$ cells. The FDTD domain is surrounded by six planes of perfectly matched layer (PML) absorbing boundary condition (ABC). The PML boundary has seven layers to absorb unwanted wave reflection. The wire conductors with round cross sections, including CW/MW and FCRW, are simulated using the thin wire model for lossy conductors presented in Section II(A). The rails are mimicked by the thin wire model for non-circular conductors presented in Section II(B). CW/MW, FCRW and rails run into the PML boundaries to simulate their infinite length. To investigate the surge voltage on the diode boxes, the diodes are represented by cells with the resistance of 1 MΩ. Insulators are represented by

breakdown models. The insulating level of the insulators is assumed to be 30 kV. Considering the volt-time flashover curve, the breakdown voltage is set to be 1.5 times of the insulating level [95], i.e. 45 kV. The LAs are modeled as active current sources using the piecewise linear method [96]. The lightning return stroke is represented by a hard current source. It generates a 4/10 μs impulse current with 50 kA amplitude according to EN50124-2. The non-uniform FDTD mesh technique is adopted. The cell size is 0.05m and 0.2m near the wire structures and poles, then is increased to 25m gradually at the boundary. The permittivity and conductivity of the lossy ground are set to be 4 and 0.01 S/m. The time step is determined based on the minimum cell size, which is equal to 9.6225e-11 s.

8.2 Lightning surge simulation

8.2.1 Direct lightning to a trackside pole

In this section, a lightning stroke terminates directly on the top of a pole, i.e., pole M or pole R10. The surge voltage on diodes at pole L4 and pole R6 is evaluated, and the simulation results are shown in Fig. 8.2. When the lightning strikes the pole M, the surge voltages on two diodes oscillate with comparable amplitudes. The voltages have their amplitudes around 60 kV at first or second peak voltage, then decreases to zero gradually. In case of the striking point at pole R10, the surge voltages on diodes have greater amplitudes during the first four microseconds. Furthermore, the voltage peak at pole R6 is almost twice as much as that at pole L4. This indicates that diodes are likely damaged by direct lightning

under the worst scenarios.

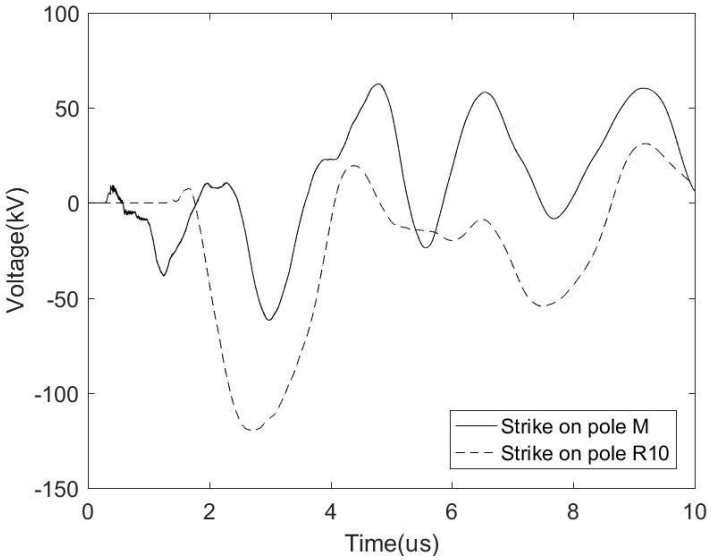

(a) Pole L4

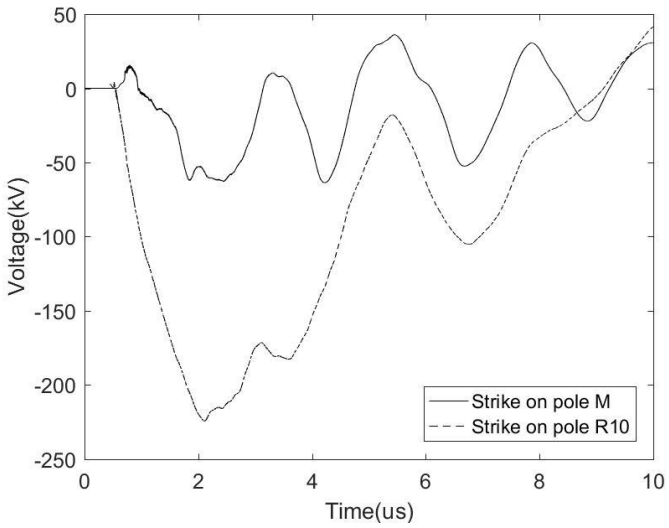

(b) Pole R6

Figure 8.2 Diode voltages at pole L4 and pole R6 during a direct lightning to the top of pole M or pole R10

8.2.2 Lightning current waveforms

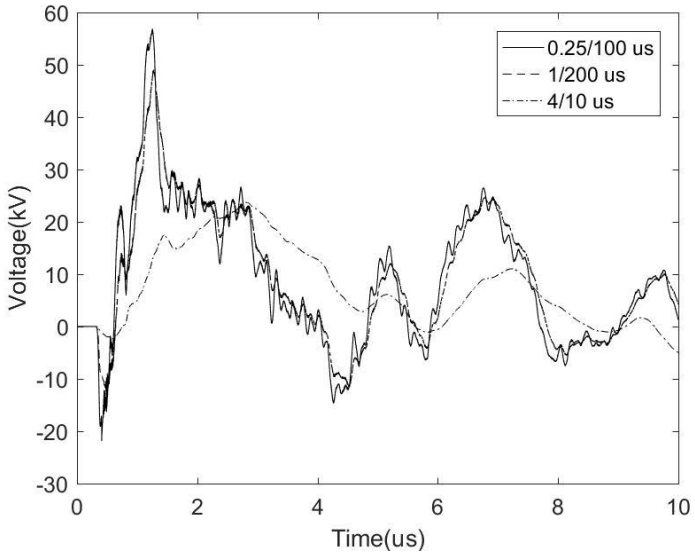

(a) Pole L4

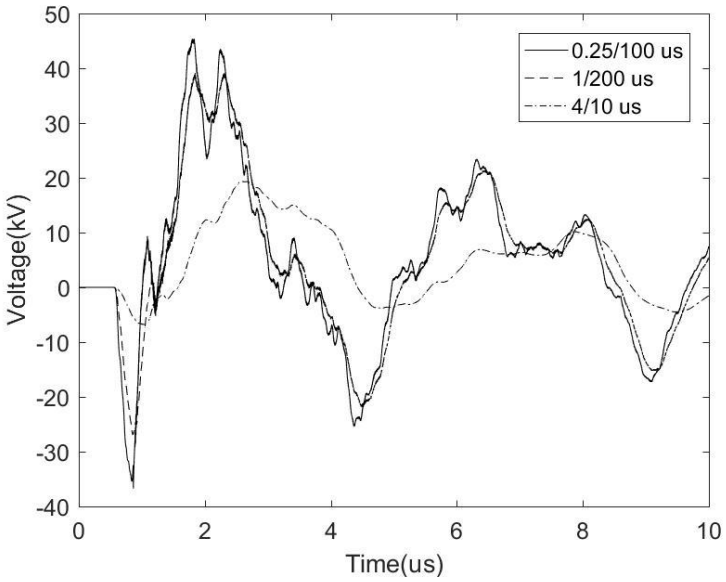

(b) Pole R6

Figure 8.3 Diode voltages at pole L4 and pole R6 when lightning strikes a building nearby.

The lightning waveforms include three types: 0.25/100 μs, 1/200 μs and 4/10 μs.

Damages caused by indirect lightning are more common in the light rail system.

In this case, lightning strikes a building located in the vicinity of a light railway. The lightning impulse electromagnetic field around the light railway will induce surge voltages on the wire structures, which could damage the diodes. To investigate the surge voltage behavior under an indirect lightning stroke, a building structure is constructed 50 m away from the pole M. For simplicity, the structure has the dimensions of $20\text{m} \times 20\text{m} \times 10\text{m}$, and has a grounding mesh buried 5 m underground with dimensions of $40\text{m} \times 40\text{m}$. The building structure is represented in the FDTD simulation with the lossless thin wire model [49, 50]. It is assumed that lightning strikes the middle point of the building roof. Three waveforms are considered, including the first negative stroke ($1/200\ \mu\text{s}$), subsequent stroke ($0.25/100\ \mu\text{s}$) and $4/10\ \mu\text{s}$ impulse current waveforms. They are all negatively polarized with 50 kA amplitude for comparison.

The simulation results are shown in Fig. 8.3. The surge voltages on diode boxes induced by first and subsequent strokes have similar waveforms and compatible amplitude. The amplitudes of induced surge voltages caused by the $4/10\ \mu\text{s}$ impulse current are much smaller. The maximum amplitudes of voltages at pole L4 and pole R6 are 57.49 kV and 45.32 kV respectively. It is observed that the steep rising front of lightning current waveforms will induce large surge voltages. In this configuration, the diodes could be possibly damaged during the indirect lightning stroke with first or subsequent lightning waveforms. The indirect lightning stroke transfers lightning energy by radiation and induction. The coupled

energy is affected by the rising time of the lightning current. A short front-time current will cause a large induced current or voltage in the light railway system.

8.2.3 Grounding resistance of the building structure

Except for the coupling effect, indirect lightning can also influence the rail system via the discharging current underground. Assume that the shortest distance between the grounding mesh of the building and the rail tracks is around 30 m. In a lightning stroke terminated on the building, the lightning current will be discharged through the building ground and increase the local ground potential, which may lead to an increase of potential rise at pole M in the light railway system. To test the significance of energy transfer via conduction, the building structure is revised by replacing original grounding mesh with a $20\text{m} \times 20\text{m}$ grounding mesh. $4/10\ \mu\text{s}$ impulse current waveform is applied to the top of the building. The simulation results are shown in Fig. 8.4. It is observed that the surge voltages on diode boxes have almost identical amplitudes in case of two mesh sizes. The surge voltages on the diode boxes are mainly caused by the coupling effect, rather than the conduction effect in this configuration.

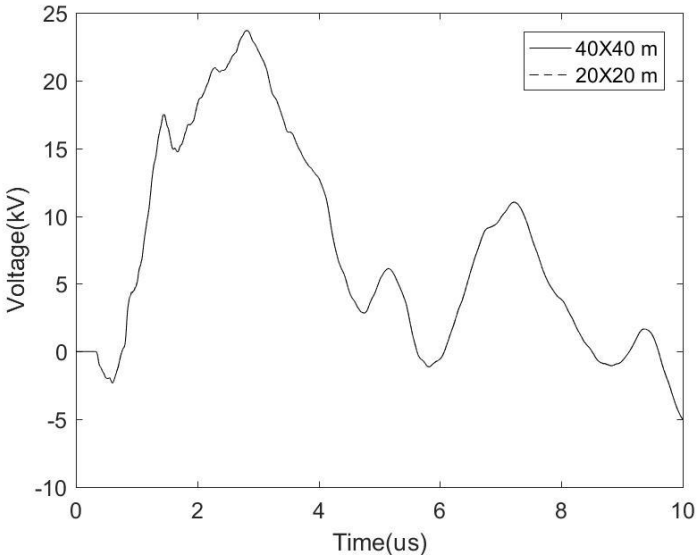

(a) Pole L4

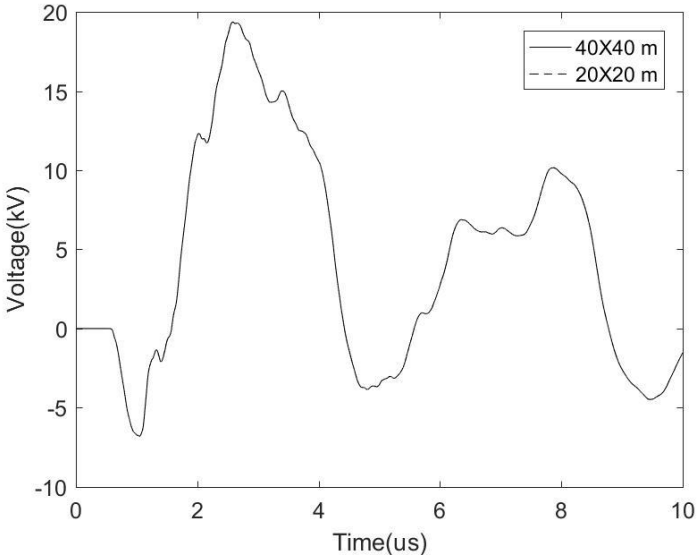

(b) Pole R6

Figure 8.4 Diode voltages at pole L4 and pole R6 when lightning strikes a building. The structure is well grounded or not grounded

8.2.4 Soil conductivity

The surge voltages on the diode boxes during an indirect lightning stroke with different soil conductivity are simulated. The conductivity parameters are set to be

0.001 S/m, 0.01 S/m or 0.1 S/m. Simulation results are shown in Fig. 8.5. It is observed that the surge voltage tends to decrease as the soil conductivity increases. No flashover is found on the insulators during the lightning strike. The FCRW and rails are isolated electrically. The voltages on the diode boxes are mainly determined by the electric potential difference between MW/CW (or rails) and FCRW. As the conductivity of soil decreasing, the grounding resistance of track side poles and grounding meshes are reduced accordingly, which will decrease the electric potential of MW/CW and FCRW, as well as the electric potential difference between MW/CW and FCRW. Therefore, the induced voltage on the diode boxes is lower in case of high soil conductivity.

8.3 Summary

In this chapter, voltage surges between rail tracks and FCRW in a light rail system under lightning strokes are analyzed by the FDTD method. The frequency dependent loss of CW/MW, FCRW and rail tracks are simulated by extended thin wire models proposed recently. The other wire structures are modeled by a traditional thin wire model. Both direct and indirect lightning strokes are simulated.

The amplitude of the surge voltage is affected by the lightning striking points, the wave-front slope of the return stroke current and the soil conductivity. A lighting stroke terminated on the OHL directly tends to cause a destructive voltage on the diode box. During an indirect lightning stroke, lightning waveforms with steep rising front and low soil conductivity could lead to damaging voltages on the

diode boxes. It is also found that the conduction coupling during a lightning stroke to a building nearby is no significant.

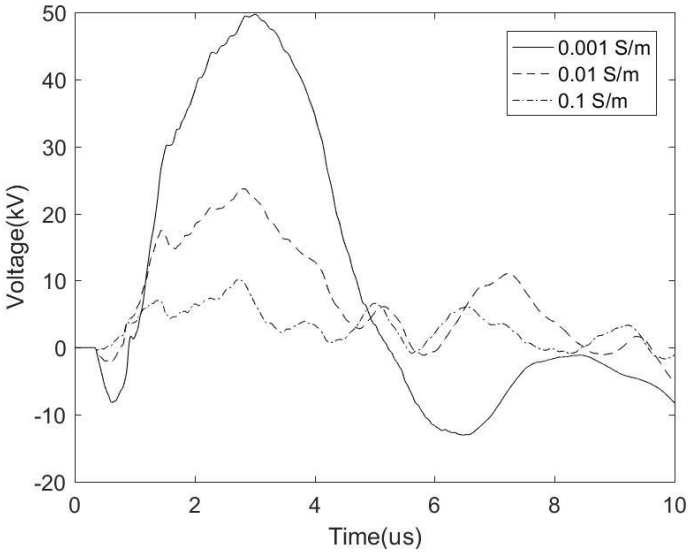

(a) Pole L4

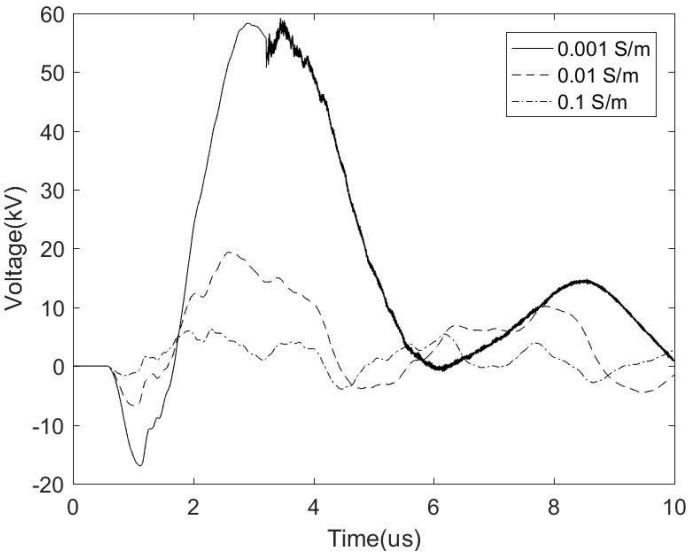

(b) Pole R6

Figure 8.5 Diode voltages at pole L4 and pole R6 when lightning strikes a building structure. The ground conductivity is set to 0.001 S/m, 0.01 S/m or 0.1 S/m

9. Conclusions and future works

9.1 Conclusions

The FDTD method is a straightforward and powerful analysis technique to solve electromagnetic (EM) problems in the time domain. The basic theory of solving equations in a staggered manner in both time and space domain was used firstly in computational fluid dynamics problems. The FDTD algorithm meshes the whole problem volume into hexahedral cells with orthogonal structure. By solving Maxwell's equations in a fully explicit way, it is not necessary to construct a large matrix during the computation procedure which will cost much less memory space. Besides, since Maxwell's equations are solved in the time domain, it performs an excellent broadband characteristic with the range from near-DC through microwaves to visible light. Thanks to its excellent parallelization characteristics, the graphics processing unit (GPU) techniques can be applied in the FDTD method conveniently to improve calculation efficiency.

One of the biggest challenges of the FDTD application is the simulation of subtle-structured models with reasonable accuracy. Theoretically, the FDTD method can model any geometric structures only if the mesh is fine enough, while, since the whole working volume is as large as hundreds of meters occasionally, an extra huge computational resource will be required. The non-uniform mesh and the traditional thin-wire model have been proposed to solve this problem, but there

remain several important issues unsolved, like skin effect, corona, frequency variant characteristics and ferromagnetic features, etc.

Chapter 3 proposed an extended thin wire model for simulating wave or surge propagation on a lossy wire structure. A time-domain cascade circuit was developed to represent the wire structure, and the skin effect was fully considered in the circuit modelling. This circuit was integrated into a traditional thin-wire model in the FDTD simulation, and the updating equations were derived for solid round wires, hollow cylindrical tubes, and coaxial cables with and without conductors being bonded. In the coaxial structure, a lossy transmission line equivalent circuit, which incorporated cascade circuits for both inner and outer conductors, was established. The currents in both inner and outer conductors were not necessarily balanced. The extended thin-wire model has been validated analytically and numerically. This model has been applied to analyze lightning current sharing in a lossy RF coaxial cable. Compared with the traditional FDTD method, this extended thin-wire model requires less memory space and less computation time in the simulation. The extended thin-wire model is shown to be stable for 1.25 million time steps.

Chapter 4 presented a series of inclined thin-wire models considering frequency-dependent losses for solid conductors, hollow tubes and coaxial conductors with reasonable accuracy. The Bessel functions and the vector fitting technique were adopted to incorporate the frequency-dependent parameters of the

conductors into the time-domain auxiliary equations. Transmission line equations of coaxial conductors were established for wave propagation analysis and linking the wire structure current and conductor currents together. Boundary conditions for the coaxial wire structure were provided as well. The bidirectional coupling between core and sheath conductors was realized with these equations. Transient simulations in three different cases were performed using the proposed inclined thin-wire models. It is found that wave propagation along inclined lossy conductors is correctly depicted, with the velocity error of less than 1% and the attenuation error of less than 1.5%. The transient currents in the inclined coaxial conductors match well with those obtained from the extended thin-wire models under the assumption that the wire structure is arranged to be in parallel with the FDTD cell edges.

Chapter 5 proposed an FDTD thin wire model with the equivalent circuit and surface charge simulation methods to simulate lossy thin wire conductors with arbitrary cross section, such as rectangular shape, H-shape, cross shape, L-shape, T-shape, U-shape and others. In this method, frequency-dependent and position-variant field quantities were evaluated with the surface charge simulation method and equivalent circuit method in the initialization process. Time-domain field correction factors are obtained with the vector fitting technique. The frequency-dependent conductor loss is fully considered by four-separated E field components, which are also obtained with the vector fitting technique. All the frequency

dependent parameters are embedded in the FDTD calculation in a convolutional approach. General guidelines on wire zone meshing are provided as well. The proposed model has been validated analytically and numerically. It is shown that this improved thin wire model can achieve good accuracy with much fewer computation resources in transient simulations. It is found that the computation time is reduced to 1% of that with the conventional FDTD method, and the computer memory to 30% in the tested case. The model has been applied to simulate lightning transients in a light rail system and in a PV power system. The frequency response of the lossy rail track can be simulated by a thin wire model rather than extremely fine meshes. The voltage difference between the PV frame and DC return circuits is measured. The FDTD calculation remains stable after 312 thousand time steps.

Chapter 6 investigated lightning-induced surges in building distribution circuits. It is concluded that the induced surge voltage in an open circuit is linearly proportional to wave-front parameters of the lightning discharge current at a rising stage, and is determined by the logarithmic function of a distance ratio of two circuit conductors. It is found that capacitors connected to the circuit can reduce the induced surge voltage, but may not be effective in suppressing the voltage down to an acceptable level. It is recommended installing SPDs at two far ends of a distribution circuit. As the surge currents are relatively small, those SPDs are not required to dissipate substantial lightning surge energy observed on the down

conductor. It is also found that the surge currents in SPDs are very similar to those in short circuits. The induced current can be treated as an independent current source. It is determined by the current in the down conductor, and has a waveform similar to the down-conductor current. The surge induced current can be estimated using a low-frequency approximate formula.

Chapter 7 and 8 described two simulation cases with applying proposed thin wire models. In chapter 7, a meteorological (lightning) observation tower was investigated with the FDTD method. The current distribution among the tower main body and inclined steel cables at the ground surface was measured. It is found that more than 90% of the lightning discharge current is carried by the stay cables. The tower body just carries a small portion of the discharge current with relatively low frequency components only. Most of the discharge current is dissipated into the earth via the horizontal grounding bars. The step voltage and GPR are analyzed and compared for three different configurations, including the reference configuration, and two simplified configurations. It is found that the steel cables and horizontal grounding bars affect the grounding performance significantly. The lightning energy absorbed by a human being in the vicinity of the tower with the reference grounding configuration is lower than the safety limit under the 2nd lightning stroke current of 100kA. In chapter 8, voltage surges between rail tracks and FCRW in a light rail system under lightning strokes are analyzed by the FDTD method. The frequency dependent loss of CW/MW, FCRW and rail tracks are

simulated by extended thin wire models proposed recently. The other wire structures are modeled by a traditional thin wire model. Both direct and indirect lightning strokes are simulated. The amplitude of the surge voltage is affected by the lightning striking points, the wave-front slope of the return stroke current and the soil conductivity. A lighting stroke terminated on the OHL directly tends to cause a destructive voltage on the diode box. During an indirect lightning stroke, lightning waveforms with steep rising front and low soil conductivity could lead to damaging voltages on the diode boxes. It is also found that the conduction coupling during a lightning stroke to a building nearby is no significant.

9.2 Future works

Most of my works during the Ph.D. period is focused on developing various thin wire models considering special cross sections, frequency dependent parameters etc. There are still some interesting thin wire models to be developed. Besides, some meaningful topics are worthwhile to be discussed as well in the future. They are summarized as follows.

1. Cables with multiple cores.

In the thesis, the thin wire models proposed in chapter 3 and 4 can simulate cables with a single core. However, multiple-core structures inside the cable sheath are quite common. For instance, cables with multi-layer structures, i.e. more than two conductor layers. By means of the idea proposed in chapter 3, as long as the

existence of sheath conductor, all kinds of thin wire models in the FDTD method can be established similarly which is divided the working volume into two zones: 1) a thin wire zone and 2) an FDTD zone. The thin wire zone contains thin wire structures only to simulate wave propagation inside the sheath conductor with other numerical and analytical method. The FDTD zone evaluates EM coupling among objects. During each updating procedure, information exchange is required on the interface of two zones.

2. Inclined wires with irregular cross sections

In chapter 4, the proposed thin wire model can mimic lossy inclined wire with a circular cross section. Actually, this model can be extended to simulate lossy inclined wire with irregular cross section. The in-cell inductance of the extended model should be evaluated section by section and frequency by frequency. Then the frequency dependent parameters can be considered by the vector fitting technique and convolutional method in time domain calculation. Even though the initialization stage will be prolonged, the in-cell inductance will be evaluated once for all. Furthermore, the stable condition of the inclined thin wire model is one of its shortages. It should be improved in the future.

3. Applications in nanotechnology

Thin wire models are widely used in power systems, railway systems and building structures. They are also applied in nanotechnologies, such as nanotubes

and nanoribbons. The major difference between the micro-material and macro-material is that the conductivity of nanostructure is a dependent parameter. Its value is dependent on frequency, chemical potential and temperature and so on. By appropriate modification of the proposed thin wire model, it is possible to investigate nanotechnology problems with thin wire models.

4. Non-linear ferromagnetism

The thin wire models proposed in this thesis can consider linear ferromagnetism in the simulation. It is hard to mimic non-linear ferromagnetism, such as saturation effect, hysteretic phenomenon and reversal loops. In the case of current distribution among multi-conductors of ferromagnetic and non-ferromagnetic characteristics, significant errors may be observed if the non-linear ferromagnetism is not considered. Since the cross section of the models proposed in chapter 3 and 5 are discretized into dense elements, and the EM field on each element is regarded as uniform, it is possible to mimic non-linear ferromagnetism by selecting an appropriate mathematic model of ferromagnetism.

5. Inclined thin sheet

Sub-cell technique in FDTD method is one of the hot tops these years. Except for the thin wire technique, the thin sheet model is also interesting and worthy to investigate. Up to now, the thin sheet model in the FDTD method must be arranged in parallel with the Cartesian axis. With the reference of the Holland thin wire

model, an arbitrary inclined thin sheet model is possible to develop by in-cell inductance technique and interpolation method. The DC parameters can be considered first, then the frequency dependent parameters.

References

[1] K. S. Yee, "Numerical solution of initial boundary value problems involving Maxwell's equations in isotropic media," *IEEE Trans. Antennas Propag,* vol. 14, no. 3, pp. 302-307, 1966.

[2] A. Taflove and M. E. Brodwin, "Numerical solution of steady-state electromagnetic scattering problems using the time-dependent Maxwell's equations," *IEEE Transactions on Microwave Theory and Techniques,* vol. 23, no. 8, pp. 623-630, 1975.

[3] A. Taflove and M. E. Brodwin, "Computation of the electromagnetic fields and induced temperatures within a model of the microwave-irradiated human eye," *IEEE Transactions on Microwave Theory and Techniques,* vol. 23, no. 11, pp. 888-896, 1975.

[4] D. M. Sullivan, D. T. Borup, and O. P. Gandhi, "Use of the finite-difference time-domain method in calculating EM absorption in human tissues," *IEEE Transactions on Biomedical Engineering,* no. 2, pp. 148-157, 1987.

[5] R. Holland, "THREDE: A free-field EMP coupling and scattering code," *IEEE Transactions on Nuclear Science,* vol. 24, no. 6, pp. 2416-2421, 1977.

[6] S. Hagness, D. Rafizadeh, S. Ho, and A. Taflove, "FDTD microcavity simulations: design and experimental realization of waveguide-coupled single-mode ring and whispering-gallery-mode disk resonators," *Journal of Lightwave Technology,* vol. 15, no. 11, pp. 2154-2165, 1997.

[7] J. Pereda, L. Vielva, M. Solano, A. Vegas, and A. Prieto, "FDTD analysis of magnetized ferrites: Application to the calculation of dispersion characteristics of ferrite-loaded waveguides," *IEEE Transactions on Microwave Theory and Techniques,* vol. 43, no. 2, pp. 350-357, 1995.

[8] A. C. Cangellaris, "Numerical stability and numerical dispersion of a compact 2-D/FDTD method used for the dispersion analysis of waveguides," *Microwave and Guided Wave Letters, IEEE,* vol. 3, no. 1, pp. 3-5, 1993.

[9] W. Sui, D. A. Christensen, and C. H. Durney, "Extending the two-dimensional

FDTD method to hybrid electromagnetic systems with active and passive lumped elements," *IEEE Transactions on Microwave Theory and Techniques,* vol. 40, no. 4, pp. 724-730, 1992.

[10] M. Piket-May, A. Taflove, and J. Baron, "FD-TD modeling of digital signal propagation in 3-D circuits with passive and active loads," *IEEE Transactions on Microwave Theory and Techniques,* vol. 42, no. 8, pp. 1514-1523, 1994.

[11] V. A. Thomas, M. E. Jones, M. Piket-May, A. Taflove, and E. Harrigan, "The use of SPICE lumped circuits as sub-grid models for FDTD analysis," *IEEE microwave and guided wave letters,* vol. 4, no. 5, pp. 141-143, 1994.

[12] P. Ciampolini, P. Mezzanotte, L. Roselli, and R. Sorrentino, "Accurate and efficient circuit simulation with lumped-element FDTD technique," *IEEE Transactions on Microwave Theory and Techniques,* vol. 44, no. 12, pp. 2207-2215, 1996.

[13] K. Tanabe, "Novel method for analyzing dynamic behavior of grounding systems based on the finite-difference time-domain method," *IEEE Power Engineering Review,* vol. 21, no. 9, pp. 55-57, 2001.

[14] Y. Baba and V. Rakov, "Voltages induced on an overhead wire by lightning strikes to a nearby tall grounded object," *IEEE Transactions on Electromagnetic Compatibility,* vol. 48, no. 1, pp. 212-224, 2006.

[15] O. Goni, F. Hossain, S. U. Yusuf, M. Rahman, E. Kaneko, and H. Takahashi, "Simulation and experimental analyses of electromagnetic transients behaviors of lightning surge on vertical conductors," *IEEE Transactions on Power Delivery,* vol. 21, no. 4, pp. 1778-1786, 2006.

[16] Y. Baba and V. Rakov, "Electromagnetic fields at the top of a tall building associated with nearby lightning return strokes," *IEEE Transactions on Electromagnetic Compatibility,* vol. 49, no. 3, pp. 632-643, 2007.

[17] Y. Du, B. Li, and M. Chen, "Lightning-induced surges in building electrical systems," in *Lightning Protection (ICLP), 2014 International Conference o*, 2014, pp. 1217-1222: IEEE.

[18] R. Courant, K. Friedrichs, and H. Lewy, "On the partial difference equations of mathematical physics," *IBM journal of Research and Development,* vol. 11, no. 2, pp. 215-234, 1967.

[19] R. F. Harrington, *Time-harmonic electromagnetic fields*. McGraw-Hill, 1961.

[20] G. Mur, "Absorbing boundary conditions for the finite-difference approximation of the time-domain electromagnetic-field equations," *IEEE Transactions on Electromagnetic Compatibility,* no. 4, pp. 377-382, 1981.

[21] Z.-P. Liao, H. L. Wong, B.-P. Yang, and Y. Yuan, "A transmitting boundary for transient wave analysis," *Scientia Sinica,* vol. 27, no. 10, pp. 1063-1076, 1984.

[22] J.-P. Berenger, "A perfectly matched layer for the absorption of electromagnetic waves," *Journal of computational physics,* vol. 114, no. 2, pp. 185-200, 1994.

[23] J. A. Roden and S. D. Gedney, "Convolutional PML (CPML): An efficient FDTD implementation of the CFS-PML for arbitrary media," *Microwave and optical technology letters,* vol. 27, no. 5, pp. 334-338, 2000.

[24] D. T. Prescott and N. Shuley, "A method for incorporating different sized cells into the finite-difference time-domain analysis technique," *Microwave and Guided Wave Letters, IEEE,* vol. 2, no. 11, pp. 434-436, 1992.

[25] S. Xiao and R. Vahldieck, "An improved 2D-FDTD algorithm for hybrid mode analysis of quasi-planar transmission lines," *IEEE MTT-S International* in *Microwave Symposium Digest*, 1993, pp. 421-424: IEEE.

[26] H. Jiang and H. Arai, "3d fdtd analysis by using non-uniform mesh," in *Microwave and Millimeter Wave Technology Proceedings, 1998. ICMMT'98. 1998 International Conference on*, 1998, pp. 947-950: IEEE.

[27] M. H. Kermani and O. M. Ramahi, "The complementary derivatives method: A second-order accurate interpolation scheme for non-uniform grid in FDTD simulation," *Microwave and Wireless Components Letters, IEEE,* vol. 16, no. 2, pp. 60-62, 2006.

[28] R. Xiong, B. Chen, B.-H. Zhou, and C. Gao, "Optimized programs for shaped

conductive backfill material of grounding systems based on the FDTD simulations," *IEEE Transactions on Power Delivery,* vol. 29, no. 4, pp. 1744-1751, 2014.

[29] B. U. Musa, W. H. Siew, and M. D. Judd, "Computation of transient electromagnetic fields due to switching in high-voltage substations," *IEEE transactions on power delivery,* vol. 25, no. 2, pp. 1154-1161, 2010.

[30] A. Tatematsu, S. Moriguchi, and T. Ueda, "Switching Surge Analysis of an EHV Air-Insulated Substation Using the Three-Dimensional FDTD Method," *IEEE Transactions on Power Delivery,* 2018.

[31] M. E. Rizk, F. Mahmood, M. Lehtonen, E. A. Badran, and M. H. Abdel-Rahman, "Computation of Peak Lightning-Induced Voltages due to the Typical First and Subsequent Strokes Considering High Ground Resistivity," *IEEE Transactions on Power Delivery*, , 2017, 32(4): 1861-1871.

[32] Q. Zhang, L. Zhang, X. Tang, and J. Gao, "An approximate formula for estimating the peak value of lightning-induced overvoltage considering the stratified conducting ground," *IEEE Transactions on Power Delivery,* vol. 29, no. 2, pp. 884-889, 2014.

[33] H. Sumitani *et al.*, "3-D FDTD computation of lightning-induced voltages on an overhead two-wire distribution line," *IEEE Transactions on Electromagnetic Compatibility,* vol. 54, no. 5, pp. 1161-1168, 2012.

[34] A. Tatematsu and T. Noda, "Three-dimensional FDTD calculation of lightning-induced voltages on a multiphase distribution line with the lightning arresters and an overhead shielding wire," *IEEE Transactions on Electromagnetic Compatibility,* vol. 56, no. 1, pp. 159-167, 2014.

[35] T. H. Thang *et al.*, "A simplified model of corona discharge on overhead wire for FDTD computations," *IEEE Transactions on Electromagnetic Compatibility,* vol. 54, no. 3, pp. 585-593, 2012.

[36] T. H. Thang, Y. Baba, N. Nagaoka, A. Ametani, N. Itamoto, and V. A. Rakov, "FDTD simulation of insulator voltages at a lightning-struck tower considering ground-wire corona," *IEEE Transactions on Power Delivery,* vol.

28, no. 3, pp. 1635-1642, 2013.

[37] T. Noda, "A tower model for lightning overvoltage studies based on the result of an FDTD simulation," *IEEJ Transactions on Power and Energy,* vol. 127, pp. 379-388, 2007.

[38] T. Noda, A. Tatematsu, and S. Yokoyama, "Improvements of an FDTD-based surge simulation code and its application to the lightning overvoltage calculation of a transmission tower," *Electric power systems research,* vol. 77, no. 11, pp. 1495-1500, 2007.

[39] T. Noda, "A numerical simulation of transient electromagnetic fields for obtaining the step response of a transmission tower using the FDTD method," *IEEE Transactions on Power Delivery,* vol. 23, no. 2, pp. 1262-1263, 2008.

[40] O. Goni, F. Hossain, S. U. Yusuf, M. Rahman, E. Kaneko, and H. Takahashi, "Simulation and experimental analyses of electromagnetic transients behaviors of lightning surge on vertical conductors," *IEEE transactions on power delivery,* vol. 21, no. 4, pp. 1778-1786, 2006.

[41] Y. Du, B. Li, and M. Chen, "Surges induced in building electrical systems during a lightning strike," *Electric Power Systems Research,* 2016 , 139: 68-74.

[42] Y. Du, B. Li, and M. Chen, "The Extended Thin-Wire Model of Lossy Round Wire Structures for FDTD Simulations," *IEEE Transactions on Power Delivery,* vol. 32, no. 6, pp. 2472-2480, 2017.

[43] K. Yamamoto, T. Noda, S. Yokoyama, and A. Ametani, "Experimental and analytical studies of lightning overvoltages in wind turbine generator systems," *Electric Power Systems Research,* vol. 79, no. 3, pp. 436-442, 2009.

[44] M. Ishii, K. Miyabe, and A. Tatematsu, "Induced voltages and currents on electrical wirings in building directly hit by lightning," *Electric Power Systems Research,* vol. 85, pp. 2-6, 2012.

[45] B. Li, Y. P. Du, and M. Chen, "An FDTD thin wire model for lossy wire structures with non-circular cross section," *IEEE Transactions on Power*

Delivery, 2018 , 33(6): 3055-3064.

[46] R. Holland and L. Simpson, "Finite-difference analysis of EMP coupling to thin struts and wires," *IEEE Transactions on Electromagnetic Compatibility,* no. 2, pp. 88-97, 1981.

[47] C. Guiffaut, A. Reineix, and B. Pecqueux, "New oblique thin wire formalism in the FDTD method with multiwire junctions," *IEEE Transactions on Antennas and Propagation,* vol. 60, no. 3, pp. 1458-1466, 2012.

[48] K. R. Umashankar, A. Taflove, and B. Beker, "Calculation and experimental validation of induced currents on coupled wires in an arbitrary shaped cavity," *IEEE Transactions on Antennas and Propagation,* vol. 35, no. 11, pp. 1248-1257, 1987.

[49] T. Noda and S. Yokoyama, "Thin wire representation in finite difference time domain surge simulation," *IEEE Transactions on Power Delivery,* vol. 17, no. 3, pp. 840-847, 2002.

[50] Y. Baba, N. Nagaoka, and A. Ametani, "Modeling of thin wires in a lossy medium for FDTD simulations," *IEEE Transactions on Electromagnetic Compatibility,* vol. 47, no. 1, pp. 54-60, 2005.

[51] Y. Taniguchi, Y. Baba, N. Nagaoka, and A. Ametani, "An improved thin wire representation for FDTD computations," *IEEE Transactions on Antennas and Propagation,* vol. 56, no. 10, pp. 3248-3252, 2008.

[52] C. J. Railton, D. L. Paul, I. J. Craddock, and G. S. Hilton, "The treatment of geometrically small structures in FDTD by the modification of assigned material parameters," *IEEE Transactions on Antennas and Propagation,* vol. 53, no. 12, pp. 4129-4136, 2005.

[53] M. Bingle, D. B. Davidson, and J. H. Cloete, "Scattering and absorption by thin metal wires in rectangular waveguide-FDTD simulation and physical experiments," *IEEE Transactions on Microwave Theory and Techniques,* vol. 50, no. 6, pp. 1621-1627, 2002.

[54] A. Tatematsu, "A technique for representing coaxial cables for FDTD-based

surge simulations," *IEEE Transactions on Electromagnetic Compatibility,* vol. 57, no. 3, pp. 488-495, 2015.

[55] B. Kordi, J. LoVetri, and G. E. Bridges, "Finite-difference analysis of dispersive transmission lines within a circuit simulator," *IEEE transactions on power delivery,* vol. 21, no. 1, pp. 234-242, 2006.

[56] G. Ledfelt, "A stable subcell model for arbitrarily oriented thin wires for the FDTD method," *International Journal of Numerical Modelling: Electronic Networks, Devices and Fields,* vol. 15, no. 5‐6, pp. 503-515, 2002.

[57] F. Edelvik, "A new technique for accurate and stable modeling of arbitrarily oriented thin wires in the FDTD method," *IEEE transactions on electromagnetic compatibility,* vol. 45, no. 2, pp. 416-423, 2003.

[58] C. Guiffaut and A. Reineix, "Cartesian shift thin wire formalism in the FDTD method with multiwire junctions," *IEEE Transactions on Antennas and Propagation,* vol. 58, no. 8, pp. 2658-2665, 2010.

[59] C. Guiffaut, N. Rouvrais, A. Reineix, and B. Pecqueux, "Insulated Oblique Thin Wire Formalism in the FDTD Method," *IEEE Transactions on Electromagnetic Compatibility,* 2017.

[60] L. Diaz, C. Miry, P. Baraton, C. Guiffaut, and A. Reineix, "Lightning transient voltages in cables of a large industrial site using a FDTD thin wire model," *Electric Power Systems Research,* 2016.

[61] R. Xiong, B. Chen, Y.-F. Mao, W. Deng, Q. Wu, and Y.-Y. Qiu, "FDTD modeling of the earthing conductor in the transient grounding resistance analysis," *IEEE Antennas and Wireless Propagation Letters,* vol. 11, pp. 957-960, 2012.

[62] R. Xiong, B. Chen, and D. Fang, "An algorithm for the FDTD modeling of flat electrodes in grounding systems," *IEEE Transactions on Antennas and Propagation,* vol. 62, no. 1, pp. 345-353, 2014.

[63] Du Y, Li B, Chen M. The Extended Thin-Wire Model of Lossy Round Wire Structures for FDTD Simulations[J]. IEEE Transactions on Power Delivery,

2017, 32(6): 2472-2480.

[64] A. Tatematsu, "A Technique for Representing Lossy Thin Wires and Coaxial Cables for FDTD-Based Surge Simulations," *IEEE Transactions on Electromagnetic Compatibility,* 2017.

[65] F. Costen, J.-P. Bérenger, and A. K. Brown, "Comparison of FDTD hard source with FDTD soft source and accuracy assessment in Debye media," *IEEE Transactions on Antennas and Propagation,* vol. 57, no. 7, pp. 2014-2022, 2009.

[66] R. L. Wagner and W. C. Chew, "An analysis of Liao's absorbing boundary condition," *Journal of electromagnetic waves and applications,* vol. 9, no. 7-8, pp. 993-1009, 1995.

[67] L. Zhang and T. Yu, "A Method of Improving the Stability of Liao's Higher-Order Absorbing Boundary Condition," *Progress In Electromagnetics Research M,* vol. 27, pp. 167-178, 2012.

[68] B. Yang, B.-H. Zhou, C. Gao, L.-H. Shi, B. Chen, and H.-L. Chen, "Using a two-step finite-difference time-domain method to analyze lightning-induced voltages on transmission lines," *IEEE Transactions on Electromagnetic Compatibility,* vol. 53, no. 1, pp. 256-260, 2011.

[69] B. Yang, B.-H. Zhou, B. Chen, J.-B. Wang, and X. Meng, "Numerical study of lightning-induced currents on buried cables and shield wire protection method," *IEEE Transactions on Electromagnetic Compatibility,* vol. 54, no. 2, pp. 323-331, 2012.

[70] Q. Zhang, X. Tang, W. Hou, and L. Zhang, "3-D FDTD simulation of the lightning-induced waves on overhead lines considering the vertically stratified ground," *IEEE Transactions on Electromagnetic Compatibility,* vol. 57, no. 5, pp. 1112-1122, 2015.

[71] H. Motoyama, Y. Kinoshita, K. Nonaka, and Y. Baba, "Experimental and analytical studies on lightning surge response of 500-kV transmission tower," *IEEE Transactions on Power Delivery,* vol. 24, no. 4, pp. 2232-2239, 2009.

[72] A. Tatematsu, K. Yamazaki, and H. Matsumoto, "Lightning surge analysis of a microwave relay station using the FDTD method," *IEEE Transactions on Electromagnetic Compatibility,* vol. 57, no. 6, pp. 1616-1626, 2015.

[73] K. Yamamoto, S. Yanagawa, and T. Ueda, "Verifications of transient grounding impedance measurements of a wind turbine generator system using the FDTD method," in *2011 International Symposium on Lightning Protection (XI SIPDA)*, 2011, pp. 255-260: IEEE.

[74] M. E. Rizk, F. Mahmood, M. Lehtonen, E. A. Badran, and M. H. Abdel-Rahman, "Investigation of lightning electromagnetic fields on underground cables in wind farms," *IEEE Transactions on Electromagnetic Compatibility,* vol. 58, no. 1, pp. 143-152, 2016.

[75] J. Chen, B. Zhou, F. Zhao, and S. Qiu, "Finite-difference time-domain analysis of the electromagnetic environment in a reinforced concrete structure when struck by lightning," *IEEE Transactions on Electromagnetic Compatibility,* vol. 52, no. 4, pp. 914-920, 2010.

[76] A. Tatematsu, F. Rachidi, and M. Rubinstein, "Analysis of electromagnetic fields inside a reinforced concrete building with layered reinforcing bar due to direct and indirect lightning strikes using the FDTD method," *IEEE Transactions on Electromagnetic Compatibility,* vol. 57, no. 3, pp. 405-417, 2015.

[77] T. H. Thang, Y. Baba, A. Piantini, and V. A. Rakov, "Lightning-induced voltages in the presence of nearby buildings: FDTD simulation versus small-scale experiment," *IEEE Transactions on Electromagnetic Compatibility,* vol. 57, no. 6, pp. 1601-1607, 2015.

[78] T. H. Thang, Y. Baba, V. A. Rakov, and A. Piantini, "FDTD computation of lightning-induced voltages on multiconductor lines with surge arresters and pole transformers," *IEEE Transactions on Electromagnetic Compatibility,* vol. 57, no. 3, pp. 442-447, 2015.

[79] A. Tatematsu and T. Ueda, "FDTD-based lightning surge simulation of an HV air-insulated substation with back-flashover phenomena," *IEEE Transactions*

on Electromagnetic Compatibility, vol. 58, no. 5, pp. 1549-1560, 2016.

[80] T. H. Thang *et al.*, "FDTD simulation of lightning surges on overhead wires in the presence of corona discharge," *IEEE Transactions on Electromagnetic Compatibility,* vol. 54, no. 6, pp. 1234-1243, 2012.

[81] T. H. Thang, Y. Baba, N. Nagaoka, A. Ametani, N. Itamoto, and V. A. Rakov, "FDTD simulations of corona effect on lightning-induced voltages," *IEEE Transactions on Electromagnetic Compatibility,* vol. 56, no. 1, pp. 168-176, 2014.

[82] G. Ala, P. Buccheri, P. Romano, and F. Viola, "Finite difference time domain simulation of earth electrodes soil ionisation under lightning surge condition," *IET Science, Measurement & Technology,* vol. 2, no. 3, pp. 134-145, 2008.

[83] C.-S. Yen, Z. Fazarinc, and R. L. Wheeler, "Time-domain skin-effect model for transient analysis of lossy transmission lines," *Proceedings of the IEEE,* vol. 70, no. 7, pp. 750-757, 1982.

[84] A. Ametani, N. Nagaoka, T. Noda, and T. Matsuura, "A simple and efficient method for including frequency-dependent effects in transmission line transient analysis," *International Journal of Electrical Power & Energy Systems,* vol. 19, no. 4, pp. 255-261, 1997.

[85] T.-C. Toh, *Electromagnetic Theory for Electromagnetic Compatibility Engineers*. CRC Press, 2013.

[86] L. Xu, Y. Du, and Q. Zhou, "The magnetic field and induced current arising from a cylindrical shell loop with an unbalanced current," *Electric Power Systems Research,* vol. 71, no. 1, pp. 21-26, 2004.

[87] S. A. Schelkunoff, "The electromagnetic theory of coaxial transmission lines and cylindrical shields," *Bell Labs Technical Journal,* vol. 13, no. 4, pp. 532-579, 1934.

[88] B. Gustavsen, "Improving the pole relocating properties of vector fitting," *IEEE Transactions on Power Delivery,* vol. 21, no. 3, pp. 1587-1592, 2006.

[89] B. Gustavsen, "Fast passivity enforcement for pole-residue models by

perturbation of residue matrix eigenvalues," *IEEE Transactions on Power Delivery,* vol. 23, no. 4, pp. 2278-2285, 2008.

[90] T. Noda, R. Yonezawa, S. Yokoyama, and Y. Takahashi, "Error in propagation velocity due to staircase approximation of an inclined thin wire in FDTD surge simulation," *IEEE Transactions on Power Delivery,* vol. 19, no. 4, pp. 1913-1918, 2004.

[91] B. Gustavsen and A. Semlyen, "Rational approximation of frequency domain responses by vector fitting," *IEEE Transactions on power delivery,* vol. 14, no. 3, pp. 1052-1061, 1999.

[92] W. J. J. Hwa, *Generalized moment methods in electromagnetics: formulation and computer solution of integral equations*. Wiley, 1991.

[93] N. Xia and Y. Du, "An efficient modeling method for 3-D magnetic plates in magnetic shielding," *IEEE transactions on electromagnetic compatibility,* vol. 56, no. 3, pp. 608-614, 2014.

[94] C. R. Paul, *Inductance: loop and partial*. John Wiley & Sons, 2011.

[95] R. Ammon, J. Anderson, G. Baker, P. Barker, and F. Muzi, "Guide for improving the lightning performance of electric power overhead distribution lines-IEEE Standard, New York," 1997.

[96] A. Tatematsu and T. Noda, "Three-dimensional FDTD calculation of lightning-induced voltages on a multiphase distribution line with the lightning arresters and an overhead shielding wire," *IEEE Transactions on Electromagnetic Compatibility,* vol. 56, no. 1, pp. 159-167, 2014.

[97] J. C. Hernandez, P. G. Vidal, and F. Jurado, "Lightning and surge protection in photovoltaic installations," *IEEE Transactions on power delivery,* vol. 23, no. 4, pp. 1961-1971, 2008.

[98] C. A. Charalambous, N. D. Kokkinos, and N. Christofides, "External lightning protection and grounding in large-scale photovoltaic applications," *IEEE transactions on electromagnetic compatibility,* vol. 56, no. 2, pp. 427-434, 2014.

[99] Y. Du and N. Xia, "Principles of power‐frequency magnetic shielding with finite‐width plates," *International transactions on electrical energy systems,* vol. 24, no. 8, pp. 1168-1184, 2014.

[100] C. F. Dalziel, "A Study of the Hazards of Impulse Currents [includes discussion]," *Transactions of the American Institute of Electrical Engineers. Part III: Power Apparatus and Systems,* vol. 72, no. 2, 1953.

[101] K. Bahra and P. Batty, "Earthing and bonding of electrified railways," 1998.